Technische Universität München

Fakultät für Physik

High-throughput Studies of Macromolecular Complexes using Flow Magnetic Tweezers

Rohit Agarwal

Vollständiger Abdruck der von der Fakultät für Physik der Technischen Universität München zur Erlangung des akademischen Grades eines Doktors der Naturwissenschaften genehmigten Dissertation.

Vorsitzender:	Prof. Dr. Martin Zacharias
Prüfer der Dissertation:	Prof. Dr. Karl Duderstadt
	Prof. Dr. Matthias Rief

Die Dissertation wurde am 09.06.2021 bei der Technischen Universität München eingereicht und durch die Fakultät für Physik am 28.09.2021 angenommen.

“Since the two chains in our model are intertwined, it is essential for them to untwist if they are to separate. As they make one complete turn around each other in 34 Å, there will be about 150 turns per million molecular weight, so that whatever the precise structure of the chromosome a considerable amount of uncoiling would be necessary. It is well known from microscopic observation that much coiling and uncoiling occurs during mitosis, and though this is on a much larger scale it probably reflects similar processes on a molecular level. Although it is difficult at the moment to see how these processes occur without everything getting tangled, we do not feel that this objection will be insuperable”

-Watson and Crick

1 Abstract

DNA replication in bacteria is an intricate process that requires coordination from numerous enzymes for its successful completion. Due to double-helical structure of the DNA, the replication fork faces a topological barrier in form of positive supercoils as it unwinds the parental strand to synthesize daughter strands. In bacterial cells, topoisomerase DNA gyrase accumulate in front of the fork to resolve these supercoils, while also maintaining a net negative superhelical density in the chromosome. Aside from relying on topoisomerases to resolve the topology, replisomes also have intrinsic mechanisms to counter the excess torsion ahead of the fork. One of these is the fork rotation where the supercoils can diffuse backwards to form precatenates which in turn are resolved by DNA topoisomerase IV. The exact mechanism of how DNA topology influences the replisome and vice versa, is difficult to decipher. Although structural, biochemical and single-molecule studies of the replisome and its components have yielded extensive information about the mechanisms involved, there were barely any studies to observe the dynamic interplay between DNA topology and a reconstituted replisome. In this thesis, an ultra-high throughput single-molecule force spectroscopy technique called Flow Magnetic Tweezers (FMT) is presented, which is an ideal platform to study topological rearrangements of DNA by multi-molecular complexes.

The application of forces and torques on single molecule level has transformed our understanding of the dynamic properties of biomolecules, but limited throughput of these techniques has hindered the characterization of rare events and intrinsic heterogeneity in a statistically robust manner. FMT provides a 100-fold improvement in throughput of force spectroscopy measurements with topological control. It does so by reconfiguring the experimental geometry of magnetic tweezers and observing tether length changes in lateral position and massive field of view. The forces were calculated by numerically solving equipartition theorem and worm-like chain model and independently validated using known force and topology dependent transitions of the DNA. Multiplexing capabilities of FMT were showcased by characterizing *E. coli* DNA gyrase and the effect of antibiotic ciprofloxacin on its dynamics. To rapidly quantify distinct classes of dynamic behaviors and rare events, a software platform with an automated feature classification pipeline called Molecule Archive Suite (MARS) was developed. Using MARS, broad quantifications of gyrase behaviors such as positive supercoil relaxation, negative supercoil introduction, unbraiding and very rare DNA breaks were detected.

Multiplexed FMT was easily adapted to characterize various eukaryotic topoisomerases and several DNA substrates were synthesized to study reconstituted bacterial replication on a topologically constrained substrate. Apart from being a method to observe enzyme dynamics, FMT can be used to study enzyme collisions or processes resulting in DNA double-strand breaks. It also shows promise as a drug screening platform. FMT can be implemented using low-cost components on standard microscopes and thus have potential applications in a broad range of fields.

2 Zusammenfassung

Die DNS-Replikation in Bakterien ist ein komplizierter Prozess, der die Koordination zahlreicher Enzyme für seinen erfolgreichen Abschluss erfordert. Aufgrund der doppelhelikalen Struktur der DNS steht die Replikationsgabel einer topologischen Barriere in Form von positiven Supercoils gegenüber. In Bakterienzellen reichern sich DNS-Gyrase vor der Gabel an, um diese Supercoils aufzulösen und gleichzeitig eine negative superhelikale Dichte im Chromosom aufrechtzuerhalten. Abgesehen davon, dass Replisomen sich auf Topoisomerasen verlassen, um die Topologie zu modulieren, haben die Komponenten des Replikationskomplexes auch intrinsische Mechanismen, um der übermäßigen Torsion vor der Gabel entgegenzuwirken. Einer davon ist die Gabelrotation, bei der die Supercoils nach hinten diffundieren können, um Präkatenate zu bilden, die wiederum von der DNS-Topoisomerase IV aufgelöst werden. Der genaue Mechanismus, wie die DNS-Topologie das Replisom beeinflusst und umgekehrt, ist schwer zu entschlüsseln. Obwohl strukturelle, biochemische und Einzelmolekül-Studien des Replisoms und seiner Komponenten umfangreiche Informationen über die beteiligten Mechanismen geliefert haben, gab es kaum Studien, die das dynamische Zusammenspiel zwischen DNS-Topologie und einem rekonstituierten Replisom beobachteten. In dieser Arbeit wird eine Ultrahochdurchsatz-Einzelmolekül-Kraftspektroskopie-Technik namens Flow Magnetic Tweezers (FMT) vorgestellt, die eine optimale Plattform zur Untersuchung topologischer Umlagerungen der DNS durch multimolekulare Komplexe darstellt.

Die Anwendung von Kräften und Drehmomenten auf Einzelmolekülebene hat unser Verständnis der dynamischen Eigenschaften von Biomolekülen verändert, aber der begrenzte Durchsatz dieser Techniken hat die Charakterisierung von seltenen Ereignissen und intrinsischer Heterogenität in einer statistisch robusten Weise behindert. FMT bietet eine 100-fache Verbesserung im Durchsatz von Kraftspektroskopiemessungen mit topologischer Kontrolle. Dies geschieht durch die Neuanordnung der experimentellen Geometrie der magnetischen Pinzette und die Beobachtung von Änderungen der Molekülausdehnung in der lateralen Position. Die Kräfte wurden durch numerische Lösung des Äquipartitionstheorems und des wurmartigen Kettenmodells berechnet und unabhängig mit bekannten kraft- und Topologie-abhängigen Übergängen der DNS validiert. Die Multiplexing-Fähigkeiten der FMT wurden durch die Charakterisierung der *E. coli* DNS-Gyrase und die Auswirkung des Antibiotikums Ciprofloxacin auf ihre Dynamik demonstriert. Um verschiedene Klassen von dynamischem Verhalten und seltenen Ereignissen schnell zu quantifizieren, wurde eine Softwareplattform mit einer automatischen Merkmalsklassifizierungspipeline namens Molecule Archive Suite (MARS) entwickelt. Mithilfe von MARS wurden breite Quantifizierungen von Gyrase-Verhaltensweisen wie positive Supercoil-Entspannung, negative Supercoil-Einführung, Dekatenierung und sehr seltene DNS-Doppelstrandbrüche erkannt.

Die Multiplex-FMT wurde leicht angepasst, um verschiedene eukaryotische Topoisomerasen zu charakterisieren, und es wurden verschiedene DNS-Substrate synthetisiert, um die rekonstituierte bakterielle Replikation auf einem topologisch eingeschränkten Substrat zu untersuchen. Abgesehen davon, dass die FMT eine Methode zur Beobachtung der Enzymdynamik ist, kann sie auch zur Untersuchung von Enzymkollisionen oder Prozessen, die zu DNS-Doppelstrangbrüchen führen, verwendet werden. Sie ist auch eine vielversprechende Plattform für das Screening von antibiotischen und krebshemmenden Medikamenten. FMT kann mit kostengünstigen Komponenten auf Standardmikroskopen implementiert werden und hat daher potenzielle Anwendungen in einem breiten Spektrum von Bereichen.

Table of Contents

1 ABSTRACT ... I

2 ZUSAMMENFASSUNG ... III

3 INTRODUCTION ... 1

3.1 DNA ... 2

3.1.1 DNA topology ... 3

3.1.2 DNA elasticity and stretching ... 4

3.2 TOPOLOGICAL STRESS DURING DNA REPLICATION ... 8

3.2.1 E. coli Replisome and Replication ... 10

3.2.2 E. coli DNA Gyrase ... 11

3.3 DYNAMICS OF MOLECULAR MOTORS ... 13

3.3.1 Optical tweezers ... 13

3.3.2 Magnetic Tweezers ... 21

3.3.3 DNA flow stretching ... 25

3.3.4 Hybrid methods ... 28

3.4 HIGH-THROUGHPUT METHODS ... 31

3.4.1 Highly parallel magnetic tweezers ... 31

3.4.2 Centrifuge force microscopy ... 33

3.4.3 Acoustic force spectroscopy ... 34

4 FLOW MAGNETIC TWEEZERS ... 37

4.1 CONSTRUCTION AND CALIBRATION OF FMT ... 39

4.2 MICROSPHERE TRACKING AND ANALYSIS SOFTWARE ... 43

4.3 SPATIAL RESOLUTION ... 44

4.4 FORCE DETERMINATION ... 45

5 INVESTIGATING DNA GYRASE DYNAMICS USING FMT ... 49

5.1 MASSIVE PARALLEL IMAGING OF TOPOLOGICAL TRANSFORMATIONS BY GYRASE ... 49

5.2 MOLECULE CLASSIFICATION ... 52

5.2.1 Feature classification using Molecule Archive Suite (Mars) ... 54

5.2.2 Gyrase behavior under different buffer conditions ... 55

5.3 GYRASE INHIBITION AND DNA BREAK FORMATION INDUCED BY CIPROFLOXACIN ... 56

5.3.1 Visualization of 100 million reaction cycles in parallel ... 59

6 CHARACTERIZING TYPE IIA TOPOISOMERASES ... 62

7 INVESTIGATING TOPOLOGICAL STRESS DURING REPLICATION 66

7.1 ALTERNATIVE DNA CONSTRUCTS 66

7.2 INITIATING REPLICATION ON THE ORIC SUBSTRATE 67

8 DISCUSSION 69

8.1 FMT IS AN ULTRA-HIGH THROUGHPUT SINGLE-MOLECULE TECHNIQUE 69

8.2 MULTIPLEXED STUDIES OF DIVERSE TOPOISOMERASES AND DRUG ACTION. 71

8.3 MECHANISM OF TOPOLOGICAL REARRANGEMENT BY *E. COLI* DNA REPLISOME 73

9 MATERIALS AND METHODS 76

9.1 EXPERIMENTAL SETUP 76

9.2 FLOW CELL SETUP 77

9.3 DNA AND BEAD PREPARATION 78

9.3.1 Handles with dUTPs containing Digoxigenin and Biotin moieties 79

9.4 DESIGNING THE ORIC PLASMID 82

9.5 DATA AVAILABILITY 84

9.6 CODE AVAILABILITY 84

10 APPENDIX I: SCHEMATICS OF FLOW MAGNETIC TWEEZERS 85

10.1 DRIFT STABILIZATION 86

10.2 FLOW CELL HOLDER 87

10.3 STAGES 88

10.4 MAGNETIC TWEEZERS 89

10.5 COMPONENTS, VENDORS AND COSTS 90

11 APPENDIX II: SETTING UP A FMT EXPERIMENT AND MOLECULE CHARACTERIZATION 92

11.1 PREPARING THE FLOWCELL FOR AN EXPERIMENT 92

11.2 ASSEMBLING DNA-BEAD TETHERS 92

11.3 CHARACTERIZATION STEPS AND ENZYMATIC EXPERIMENT 93

12 APPENDIX III: DETERMINING PIXEL DIMENSIONS 95

13 APPENDIX IV: FLOW PROFILE IN THE FLOW CELL 96

14 APPENDIX V: SUPPLEMENTARY MOVIES 98

15 ABBREVIATIONS 99

16 ACKNOWLEDGEMENTS 101

17 REFERENCES 103

3 Introduction

In biology, cells are considered to be the basic unit of all known life-forms on the planet. A hallmark of life is the compartmentalization of biomolecules in these membrane-bound cells. These biomolecules in the form of enzymes serve as work-horses for the cell, while ATP provides the energy currency, and DNA present as an elegant coding mechanism to ultimately build the proteins. As efficient and dynamic as the cellular environment is, the constituent processes are exceedingly complex. Owing to the sheer number of molecules in a cell, ensemble averaging techniques represent a physiologically relevant mean average behavior of certain enzyme populations. These however fail to take into account the molecular heterogeneity among these molecules. Intrinsic to their biological and physiological function, molecular machines usually exhibit multiple conformations while the cellular environment facilitates a fundamental instability enabling the molecules to alternate between these different states. Bulk ensemble averaging cannot be used to probe multiple states in a heterogeneous system whereas single-molecule measurements enable studies of these subpopulations. Single-molecule studies come into play when considering that the actual amount and stoichiometry of molecules involved in specific biological processes are generally lower as compared to the diverse population of total molecules in a cell.

Single-molecule, biophysical studies are technically challenging as they are conducted in a regime governed by stochastic thermal fluctuations with energies on the order of several k_BT (k_B is Boltzmann's constant and T is temperature in Kelvin), forces at piconewton (pN) scale and lengths of molecules in nanometers (nm), which is two orders of magnitude smaller than the wavelength of visible light. These further compounds the problem of acquiring data with enough spatial and temporal precision. Hence the requirement is to obtain discernible data where signal is negligible and the setting is noisy, leading to inherently lower yield in throughput. In recent years, many technical advances have enabled researchers to multiplex these measurements leading to higher throughput techniques. Some of these techniques will be discussed here including the novel method Flow Magnetic Tweezers (FMT).

3.1 DNA

Deoxyribonucleic Acid (DNA) is the primary genetic molecule carrying information that enables a cell to develop, function and proliferate. It is comprised of two complementary polynucleotide chains running anti-parallel to each other and encodes information using four bases: Adenine (A), Thymine (T), Cytosine (C) and Guanine (G) where T is complementary to A and C to G[1]. A nucleotide is the fundamental building block of DNA and consists of a phosphate linked to a sugar called 2'-deoxyribose forming a sugar-phosphate backbone to which the bases are attached. Nucleotides are linked to each other through the 3'-hydroxyl of one nucleotide and 5'-hydroxyl of the other nucleotide through a phosphodiester linkage which imparts an inherent polarity to the DNA chain (Figure 3-1). These bases interact with their partners through hydrogen bonding and form a DNA ladder where hydrophobicity of the bases stacks them inwards and the sugar-phosphate backbone outwards. This structure exists as a double-helix with multiple possible conformations (such as B-DNA, A-DNA and Z-DNA), but the most common is B-form, which is a right-handed helical structure with 1 turn spanning 34 Å containing ~10.5 basepairs (bps) and a polymer chain ~2 nm wide[1].

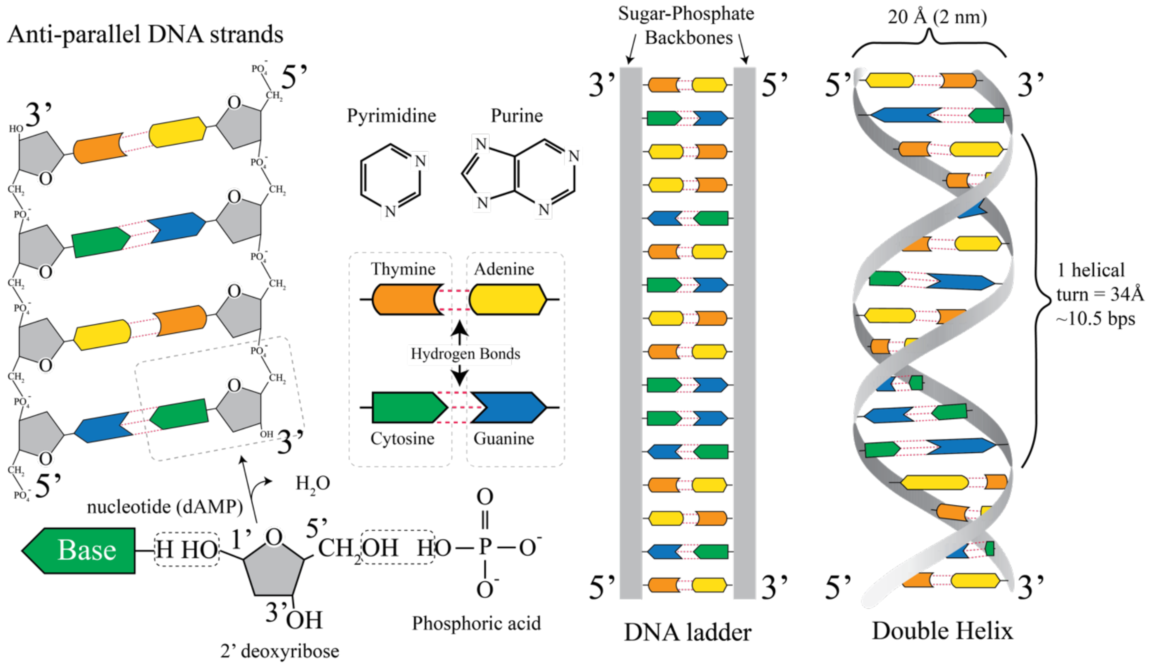

Figure 3-1 Helical structure of DNA. A nucleotide forms by a dehydration reaction and consists of a deoxyribose sugar and phosphate connected to a base. The nucleotides form a polynucleotide polymer through phosphodiester linkages of the sugar-phosphate backbone. This imparts directionality to the DNA conventionally written from the 5' to the 3' direction. These anti-parallel and complementary strands form

a DNA-ladder which twists into a double-helix ~2 nm wide and with a helical pitch of 34 Å (~10.5 bps) (adapted from Molecular Biology of the Gene[1]).

3.1.1 DNA topology

This helical-form although elegant, is still to be untwisted to be separated. As quoted by Watson and Crick in their seminal study of DNA structure: "Although it is difficult at the moment to see how these processes (mitosis) occur without everything getting tangled, we do not feel this objection will be insuperable."[2]. Therefore, DNA topology influences DNA structure and its biochemical interactions. Various processes like DNA replication, transcription or DNA repair can alter the topology of the genome and introduce complications like knotting and catenation. A simple example to study topology can be a covalently closed, circular DNA (cccDNA: like plasmids) whose results can be generalized to linear DNA subjected to topological constraints[1].

The intertwining of the complementary strands is described by the linking number (Lk). An integer, Lk is the sum of geometric components called twist (Tw) and writhe (Wr). Tw is the number of times one strand wraps around the other strand. For relaxed DNA, Lk is similar to Tw. Lk_0 notates Lk of a relaxed DNA and can be altered by cutting and rejoining a strand of DNA. ΔLk is the difference between Lk_0 and Lk. The helix can be overwound or underwound which results in a +ΔLk or a -ΔLk. In Figure 3-2, a relaxed cccDNA is underwound by ΔLk = -4. A Wr of -4 results in a right-handed helical buckling of the cccDNA into loop-like structures called plectonemic supercoils. If the Lk is conserved following introduction of -Wr, it can interchange with Tw as $\mathbf{Lk = Tw + Wr}$. A ΔLk of -4 can be accommodated by formation of 4 plectonemic supercoils (Wr = -4), a denaturation of 4 helical turns (Tw = n – 4, where n is Lk_0) or a mix of both[3]. Topological deviation from the relaxed state can be reported by using superhelical density (σ). Sigma is independent of DNA length and given by: $\boldsymbol{\sigma = \Delta Lk / Lk_0}$.

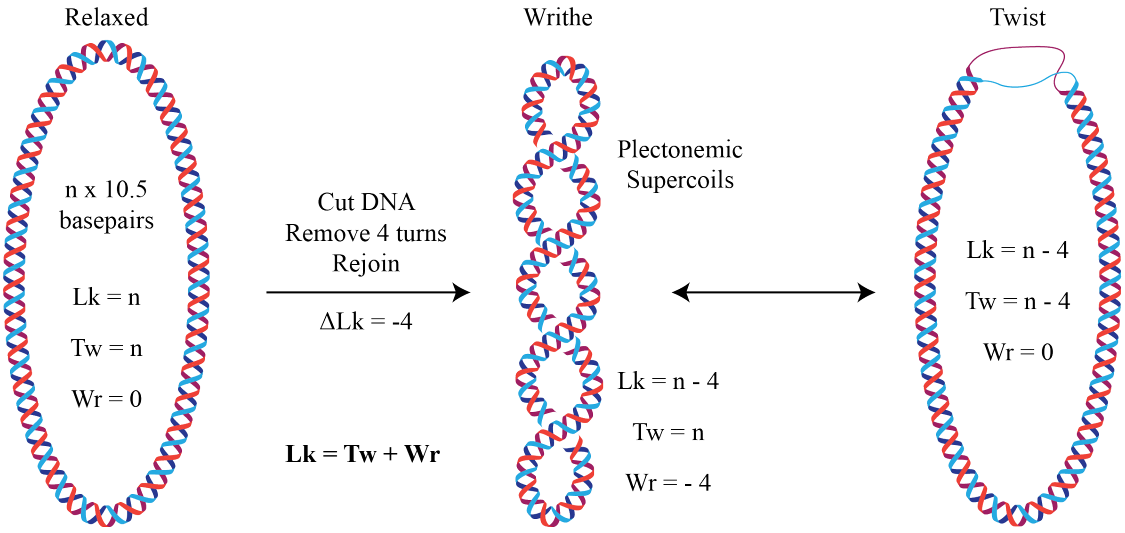

Figure 3-2 Topological state of cccDNA. A relaxed DNA has $Lk_0 = n$. Upon underwinding ($\Delta Lk = -4$), the strain from the supercoiled state can be taken by formation of plectonemic supercoils ($Wr = -4$) or by local disruption of base pairings ($Tw = n - 4$). Adapted from Koster *et al.*[3] and Molecular Biology of the Gene[1].

3.1.2 DNA elasticity and stretching

Force-extension behavior of DNA is largely defined by its polymeric properties. The freely-jointed chain (FJC) model was first proposed by Werner Kuhn where he approximated conformations of polymers in solution by viewing the chain as rigid segments connected by flexible links[4]. The parameter b called Kuhn length (Figure 3-3 A) serves as an operational measure of polymer rigidity as stiffer polymers remain straight over longer distances and vice-versa. Number of segments N here could be obtained simply by dividing the length of the chain L by Kuhn length b: $\mathbf{N = L/b}$. Long polymers display random coil conformations with constituent segments displaying stochastic movement akin to processes such as diffusion or random walks. Thus, the coil fluctuates on the scale of N where average size of this coil scales with square root of polymer length. $\mathbf{\langle R^2 \rangle = Lb}$.

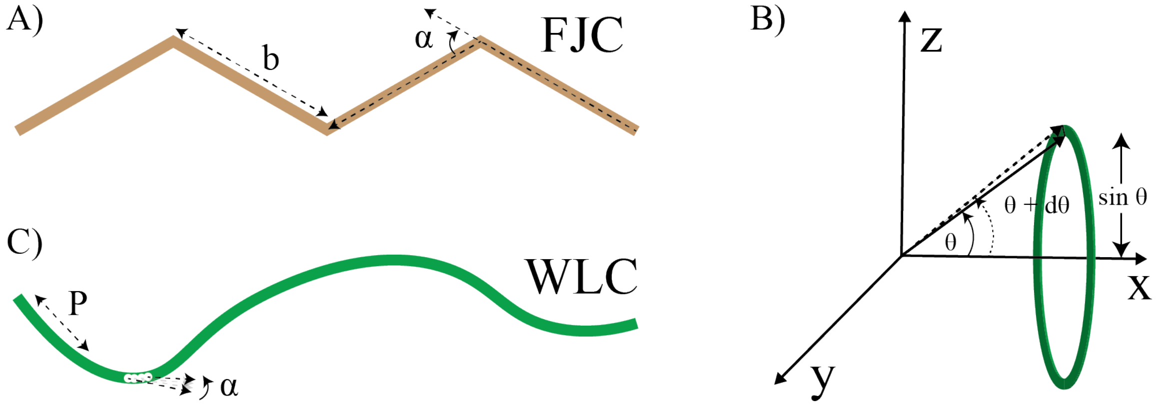

Figure 3-3 Polymer models of DNA. A) FJC model assumes polymers as an array of rigid segments of Kuhn length b with angle α to the adjacent segment. The orientation of these segments is uncorrelated. B) Statistical weight of various conformations of a rigid segment in uniform force field. The segment changes conformation within the confines of the sector between angles θ and θ + dθ and is proportional to the area of this sector on a unit sphere. Radius of this sector is sinθ and area is 2πsinθdθ. C) WLC model assumes a constant time-averaged curvature of the chain. The average angle α of tangents of adjacent monomers is a measure of this curvature and rigidity of the chain. The Persistence length P quantifies the bending stiffness of the polymer. (adapted from Sarkar et al.[5])

DNA being a fairly rigid polymer, conforms well to this model with b ≈ 300 bp. Application of force distorts the isotropic orientation of the Kuhn segments and result in a restoring entropic elastic force that resist stretching. In a constant force field, the segments follow Boltzmann distribution:

$$W(\theta) = e^{\frac{-\Delta G}{k_B T}} = 2\pi \, sin\theta \; e^{\frac{F \, bcos\theta}{k_B T}} \tag{3.1}$$

ΔG: Free energy of the segment

θ: Angle between segment and force vector

$F * b.cos\theta$: Energy of the segment in the field with $b.cos\theta$ being projection of segment on force

$2.sin\theta$: statistical weight of conformation for the given angle θ.

Average projection of the segments onto the force field L_x is given by:

$$L_x = \frac{\int_0^{\pi} b.cos\theta \, . \, W(\theta)\, d\theta}{\int_0^{\pi} W(\theta)\, d\theta} = b.\mathcal{L}\left(\frac{Fb}{k_BT}\right) \tag{3.2}$$

Since arrays of these segments are under constant force field, the relative extension is $x = L_x/L$.

$$x = \mathcal{L}\left(\frac{Fb}{k_BT}\right) = \coth\left(\frac{Fb}{k_BT}\right) - \frac{k_BT}{Fb} \tag{3.3}$$

Relative extension of all polymers is dependent on force and rigidity where a more flexible chain requires higher force to achieve similar extension as a rigid polymer[5]. As DNA is a soft spring, miniscule forces lead to longer extensions initially. For $Fb << k_BT$, the behavior is analogous to Hooke's law which describes an ideal spring as $\mathbf{x = Fb/3k_BT}$. As Langevin function $\mathcal{L}$ can be approximated by ideal spring behavior for larger extensions ($Fb \approx k_BT$), this model poorly describes DNA elasticity at high extensions[6]. As local polymer curvature on scales shorter than b is not taken into account, the shape of shorter as well as highly extended chains is significantly distorted[7].

A finer description of such conformations can be approximated using a worm-like chain (WLC) model as it accounts for the local curvature by taking into account relative bending of adjacent monomers by an average angle $\alpha = <\alpha^2>^{1/2}$, which remains the same throughout the chain as expected from the constant energy associated with each degree of freedom (Figure 3-3 C). Thus, correlation between a vector that is tangent to the polymer at initial position (u_1), and tangent vector n monomers away at distance l (u_n), decays exponentially with increasing separation between the monomers.

$$< u_1 . u_n > = e^{-\frac{l}{P}} \tag{3.4}$$

$$P = \frac{2l_0}{< \alpha^2 >} \tag{3.5}$$

l: distance between monomers along the chain

l_0: distance between adjacent monomers

P: Persistence length

End-to-end distance R can be calculated as:

$$< R^2 > = 2P[L - P\left(1 - e^{-\frac{L}{P}}\right)] \tag{3.6}$$

For long polymers, $<R^2> = 2PL$, which results in same statistics as FJC model with b = 2P.

Persistence length acts as the primary parameter that defines extension of polymers by applied forces with a value ~45 nm at physiological monovalent salt concentrations (~150 mM)[8]. The WLC equation can only be solved numerically and force-extension data is usually fit to the following equation[7]:

$$F = \frac{k_B T}{P}\left[\frac{1}{4}\left(1 - \frac{x}{L}\right)^{-2} - \frac{1}{4} + \frac{x}{L}\right] \tag{3.7}$$

3.2 Topological Stress during DNA replication

The majority of bacterial species contain a single circular chromosome, 2-8 Megabasepairs (Mbp) in size which replicates bidirectionally from a unique origin (*oriC*). Linear length of this DNA strand is upwards of 1 mm while it is packed in a space less than 1 µm in diameter, i.e. >1000-fold compaction to fit inside an organism. As DNA needs to be accessible at all times to the organism, it has to be condensed in an orderly and hierarchical fashion in the cell[9]. The principal mechanism of DNA compaction in bacteria is through negative supercoiling of the chromosome. When the double-helix is underwound, it forms plectonemic loops which help condense the chromosome. This global negative superhelical density is essential for numerous cellular processes such as numerous processes including transcription, replication, repair and recombination[10]. To avoid undesirable relaxation due to DNA damage, a chromosome is organized into topologically insulated domains[11]. Replication of this chromosome is an intricate interplay of multiple enzymes and enzyme-complexes, some of which are shown in Figure 3-4.

Negative supercoiling lowers the free energy necessary for denaturation of DNA and apart from chromosome compaction, also plays a role in decatenation. The replication system of *Escherichia coli* (*E. coli*) is discussed here where the enzyme complex replicates ~600 bps/s *in vivo*[12]. Although the bulk of the *E. coli* chromosome is (-) supercoiled, the parental strand around the fork is (+) supercoiled due to constant unwinding by the replisome and this excessive (+) supercoil accumulation can inhibit fork-progression in absence of fork-rotation. Rotation of the fork on the other hand leads to the formation of precatenates between nascent-daughter chromosomes which must be unlinked prior to chromosome segregation. Topoisomerases are a class of highly conserved and essential enzymes that actively regulate the topological state of the genome. DNA Gyrase and topoisomerase (topo) IV are type 2 topoisomerases present in *E. coli* that play an important part in modulating topology and catenation of the double helix of the parental duplex as well as the two separate daughter strands post-replication. Gyrase has the unique ability to introduce (-) supercoils in (+) supercoiled or relaxed DNA while topo IV is primarily a decatenase[11], thus gyrase acts ahead of the fork and topo IV removes precatenates behind[10] (Figure 3-4 A).

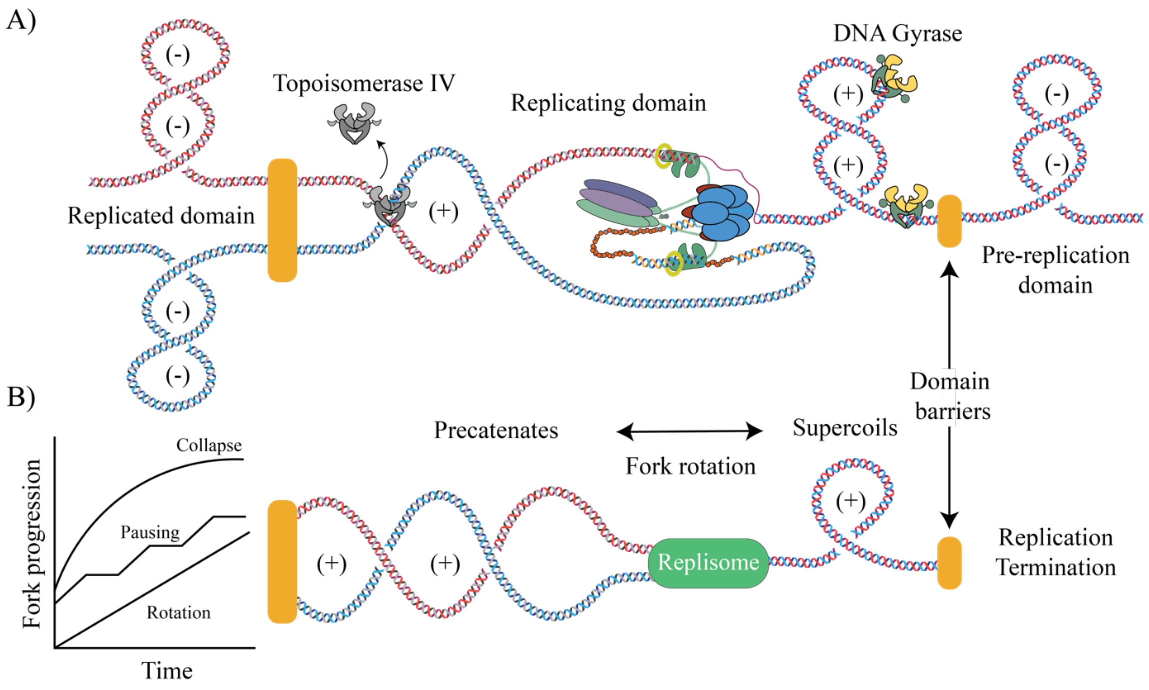

Figure 3-4 Model for topology of a replicating chromosome. A) The enzyme Gyrase keeps the native E.coli chromosome (-) supercoiled (Pre-replication domain). The bulk of the chromosome is protected from hazards of DNA damage as it is divided into topological domain barriers. Replication creates (+) ΔLk in the replicating domain which causes (+) coiling ahead of the fork and (+) precatenates behind it. Thus, gyrase helps replication by removing the (+) supercoils in front of the fork and topo IV by removing precatenates behind the fork. The replicated domains segregate eventually making two separate daughter chromosomes. B) Towards replication termination, the available parental strand gets (+) supercoiled and active topoisomerases are titrated away due to daughter chromosomes. This can result in several topology-based fates for an active fork. i) The fork can rotate so the (+) superhelical stress can diffuse through the replisome and form precatenates. ii) The fork can pause and decouple leading- and lagging- strand to release the stress as it progresses. iii) Accumulation of (+) superhelical stress can result in fork collapse which can be detrimental to an organism. (adapted from Postow *et al.*[11])

As the replication fork nears replication termination, the unreplicated strand becomes shorter while the replicated strands titrate away the pool of active topoisomerases (Figure 3-4 B). This topological problem with a lack of topoisomerases can be resolved by continuous fork rotation where (+) superhelical stress in front of the fork can diffuse to create interwinding precatenates behind. Alternatively, the fork can occasionally pause to decouple leading- and lagging- strand polymerases to release the excess torsional strain as suggested by Kurth *et al.*[13]. Finally, in case of a constrained DNA substrate and absence of dissipation of torsional strain, the fork will collapse leading to a failure in replication which is catastrophic for an organism.

3.2.1 *E. coli* Replisome and Replication

Bacterial DNA replication is divided into three stages: initiation, elongation and termination. *E. coli* replication, which has long been a model system to study bacterial DNA replication, is discussed here.

The *E. coli* chromosome is 4.6 Mb in size and replication initiates at a locus called *OriC* which is a 250-bp long. The initiator protein DnaA facilitates DNA melting and bubble formation for subsequent helicase-loading. Two DnaB helicase hexamers are loaded onto each of the separated single-stranded DNAs (ssDNA) in the initiation bubble with the help of DnaC (helicase loader). Interaction of DnaG primase with the N-terminal collar of DnaB stimulates DnaC disassociation forming two replication forks[14].

The primase produces a leading-strand RNA primer for DNA elongation and repeatedly primes the Okazaki-fragments (OF) synthesis on the lagging-strand. These RNA primers are replaced by DNA through gap-filling and nick translation by DNA polymerase (pol) I, while the nicks are sealed by DNA ligase. Major replication polymerase here is DNA pol III which consists of the $\alpha\varepsilon\theta$ polymerase core and the β_2 sliding clamp. In the core, α is the polymerase subunit, ε is the 3'-5' proofreading exonuclease and θ is a small subunit that stabilizes ε. The γ- clamp loader loads β_2 clamp onto the primed terminus. The clamp increases processivity of Pol III (>150 kb) and synthesis speed of circa 1000 bp/s. Single strand-binding (SSB) proteins stabilize ssDNA on the lagging strand [14].

Replication terminates at 23-bp termination (*Ter*) sites using protein Tus by forming a polar Tus-*Ter* lock complex which has permissive and non-permissive face for the replisome to either pass or be blocked. This ensures proper fork convergence and chromosome segregation. Topo 2 ultimately decatenates the linked circular DNA duplexes. The following schematic shows some constituent proteins of the E. coli replisome with coupled leading- and lagging-strand synthesis[14].

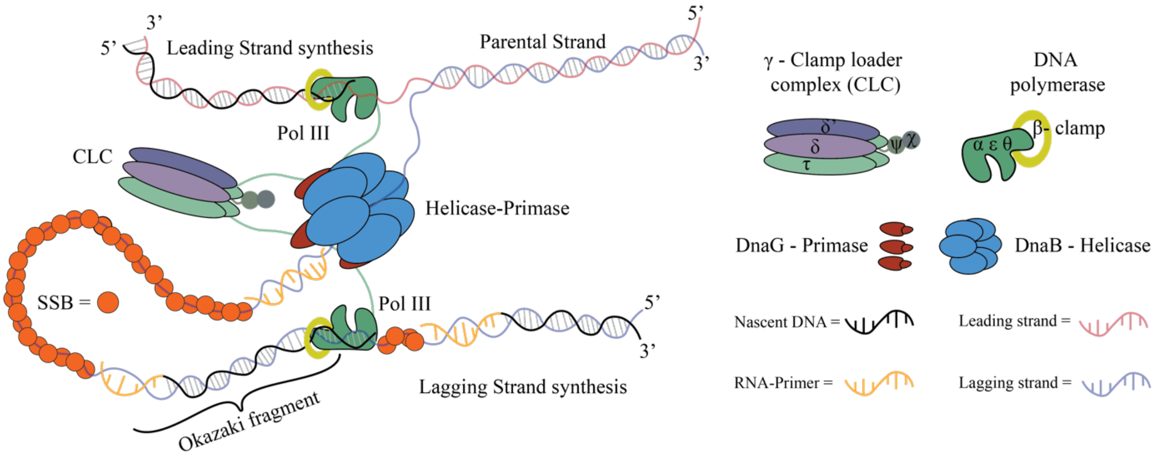

Figure 3-5 Schematic of the *E. coli* replisome. Parental strand is separated by DnaB helicase and primed by DnaG primase where leading-strand (red) has continuous synthesis by Pol III connected to DnaB via τ subunit of the clamp loader complex. Multiple priming events are required on the lagging-strand (blue) to prime the Okazaki fragments. Meanwhile, the ssDNA on the lagging strand is bound by single strand binding proteins. Daughter strands show semiconservative replication as the final leading- and lagging-strands constitute one parental strand each. (adapted from Xu *et al.*[14])

3.2.2 *E. coli* DNA Gyrase

Topoisomerases solve complex topological problems using the elegant chemistry of transesterification reactions. A transient break is created where active site tyrosine forms a covalent adduct with the backbone phosphate by acting as a nucleophile to initiate the first transesterification[15,16]. The break is resealed by reversing the first reaction and regenerating free tyrosine. They are divided into type I and type II where the former carries out strand passage through a single strand break and the latter mediates strand transport thorough a double-strand DNA gate and changes the Lk by 1 and 2 respectively[15].

E. coli DNA gyrase is a tetramer made of two GyrB and two GyrA subunits. It is a type IIA topoisomerase that catalyzes the passage of duplex DNA through another by binding and opening a DNA gate in a duplex region termed the G segment. A second stretch of duplex called the T segment is then captured, followed by binding of two ATP molecules in the ATPase domain of the GyrB subunits. The first ATP consumption promotes passage of the T segment through the DNA gate. Subsequently, the cleaved G segment is resealed and ΔLk = -2 with hydrolysis and release of second ATP resetting the enzyme[15]. Gyrase uses energy from ATP hydrolysis to continue this cycle to further negatively supercoil DNA and maintain a -σ in the chromosome in *E. coli*.

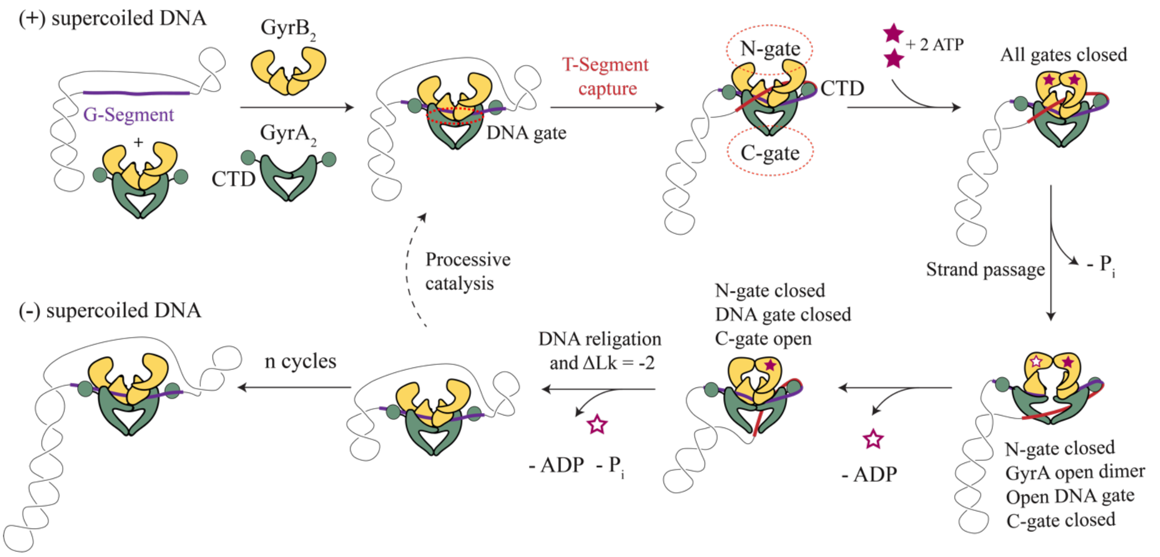

Figure 3-6 Mechanism of supercoiling of DNA by gyrase. Gyrase binds to the G-segment at the interface of GyrA and GyrB subunits in the region of the DNA gate. The DNA wraps around the C-terminal domains (CTD) of GyrA which is essential for introducing (-) supercoils into DNA. The CTD guides the T-segment to enter the space between the N-gate of the two GyrB subunits. Binding of the 2 ATP molecules to GyrB subunits causes the N-gate to close, thus trapping the T-segment inside the GyrB subunits. The gate opens as the active site tyrosines in the GyrA subunits cleave the G-segment and form covalent protein/DNA intermediate. The T-segment passes through the open DNA gate and one ATP is hydrolyzed in this step leaving one ATP and one ADP bound the GyrBs. After strand-passage, the DNA gate closes and ADP detaches from the complex opening C-gate which releases the trapped T-segment. Ultimately, the second ATP is hydrolyzed, closing the C-gate and opening the N-gate thus readying the enzyme for subsequent cycles. Gyrase has the unique to relax (+) supercoiled DNA and also introduce (-) supercoiled DNA using the same cyclic process as shown. One cycle changes the Lk by -2. (Adapted from Soczek *et al.*[17])

Although change of topology by gyrase requires a double-strand break, the cleaved gate must be resealed to avoid severe DNA lesions eventually leading to cell death. Quinolone antimicrobials are widely used drugs and only known agents that directly inhibit bacterial DNA replication. They target both Gyrase and topo IV by blocking the strand-passage catalysis thus generating double-strand breaks in DNA. Quinolones bind reversibly to the complex of gyrase with DNA near the active site tyrosine and block the resealing of the DNA double-strand break by stabilizing the gyrase-DNA complex which also serves as a barrier to the movement of the DNA replication fork and can be converted into a permanent double-strand break. This triggers bacterial SOS DNA repair response with incomplete repair generating quinolone bactericidal activity[18].

3.3 Dynamics of molecular motors

Molecular motors transform the chemical energy derived from hydrolysis of molecules like ATP/ GTP or a proton gradient to drive physical work inside cells. Some examples are cytoskeletal motors such as Kinesins (intracellular cargo transport) and Myosins (muscle movement), rotary motors like F_OF_1-ATP synthase (ATP synthesis) and bacterial flagellum (bacterial motility) or nucleic acid motors like DNA polymerase (synthesizing complementary DNA strand), SMC proteins (chromosome condensation) and Topoisomerases (DNA topology modulation). The conformational changes of these proteins range in steps of a few nanometer with forces of several piconewtons. Although structural interrogation of these motors can be carried out using electron microscopy (EM)[19], nuclear magnetic resonance (NMR)[20] or X-ray crystallography[21], the dynamics can be studied using force-spectroscopy methods.

3.3.1 Optical tweezers

Optical trapping of particles using laser radiation pressure is a pioneering technique introduced by Arthur Ashkin in 1970[22] and further modified to assert a net optical force on dielectric particle of higher refractive index than the surrounding medium towards the intensity maximum of a focused laser[23]. The basic principle of this method is shown in Figure 3-7. This diffraction limited spot is created by a high numerical aperture (NA) objective focusing the laser beam and trapping dielectric particles such as beads with a three-dimensional restoring force towards the focus. The position of a bead is measured via an interference pattern of either the trapping light or a separate tracking laser following re-collimation by the condenser lens. The interference pattern on the back focal plane of the condenser goes through an imaging lens (omitted in the figure) onto a quadrant photo diode (QPD). A QPD is characterized by its high responsivity and temporal resolution (>10kHz) as compared to cameras which have lower frame rates[24]. Any shifts in the interference patterns due to displacement of the bead are registered as electrical signals. The forces acting on the bead here are called the gradient force and the scattering force. Induced dipoles in the bead interact with the steep gradient near the focus and force the bead along the gradient. The scattering forces occur in the direction of the laser, shifting the bead slightly past the focus of the beam. In order to get a stable trap, the gradient forces must overcome the scattering forces hence making a high NA objective necessary. For smaller displacements around 150 nm, this trap can be modelled as a Hookean spring where force $F = -\alpha x$ (α is the spring constant and x is the displacement)[24]. The stiffness of the trap depends on the steepness of the optical gradient, laser power and polarizability of the substance.

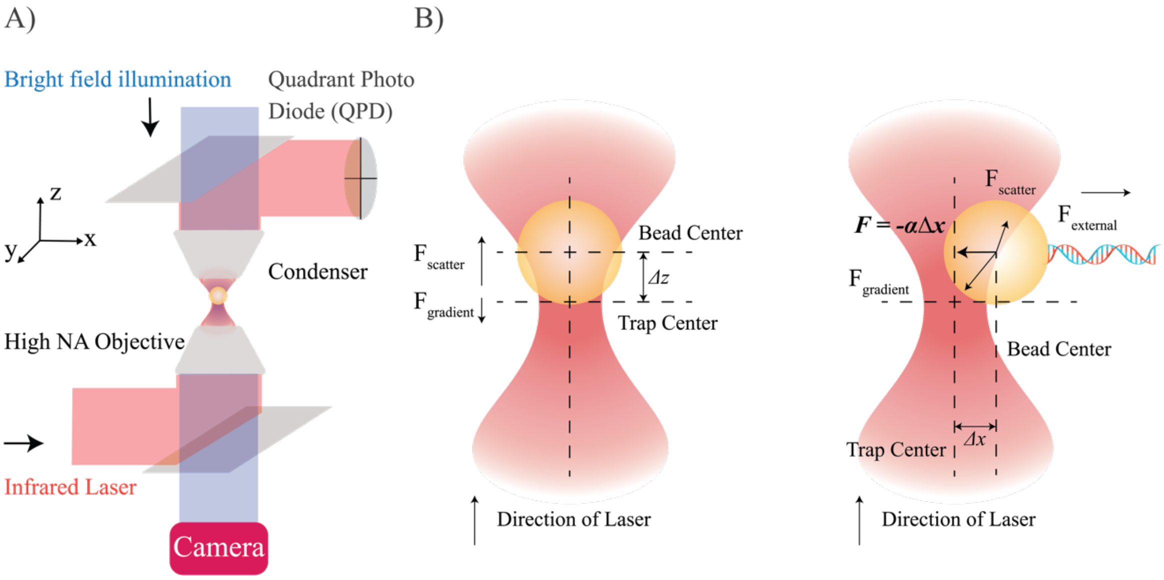

Figure 3-7. Setup and principle of Optical Tweezers. A) Basic components of optical tweezers setup consist of a laser beam which traps a dielectric particle towards its intensity maximum. This is achieved through a high NA Objective where a collimated beam is focused to a diffraction limited spot before being re-collimated by a condenser lens. The interference pattern of the exit beam is imaged by a Quadrant Photo Diode (QPD) and the voltage read-out can be converted to displacement readings. B) The scattering force $F_{scatter}$ acts in the direction of the laser while the gradient force $F_{gradient}$ operates towards trap center where the field gradient is the highest, hence a stable position at displacement Δz from the trap center. Lateral displacement Δx of the bead due to external force $F_{external}$ is opposed by the scatter and gradient forces leading to a net Hookean restoring force $F = -\alpha x$ where α is the trap stiffness or the spring constant. (adapted from Miller *et al.*[25])

Historically, the setup was used to study the then-newly discovered force-generating protein, Kinesin[26]. Block *et al.* used the trap to facilitate positioning the kinesin-coated beads onto the microtubule as compared to freely diffusing protein (Figure 3-8 A); significantly improving the yield of the of the bead assay, particularly at low protein concentration[27]. They found a kinesin molecule to be processive for 1.4 μm. Higher concentration of protein led to a more processive movement of several microns. A subsequent tweaking with differential interference contrast optics and QPDs from Svoboda *et al.* led to the instrument having higher spatio-temporal sensitivity with which they were able to resolve the 8 nm step of the kinesin motor[28]. The study indicated a linear decrease in velocity with increasing force and the machines being able to oppose forces up to 5 pN.

Geometries of the optical traps were further modified to study protein-nucleic acid complexes[29]. Stretching of nucleosomal arrays where a DNA is tethered to the slide surface and an optically trapped bead revealed a reversible and multistage release of DNA (Figure 3-8 B). A release of ≈76 bp of DNA from nucleosome was observed at low and incrementing forces; but higher forces lead to an abrupt release of ≈80 bp of DNA. To further modify trap geometry, a second trap can be added to the setup, decoupling the sample from any attachment to a chamber hence reducing the associated drift and noise. A dual-trap such as this is suspended in solution and can be moved in the sample chamber freely; enabling features such as instantaneous buffer exchange in a multichannel laminar flow cell by moving the trapped beads and sample between different lanes. Such setup was used to observe ångström-level resolution and base-pair stepping by RNA-polymerase (Figure 3-8 C)[30].

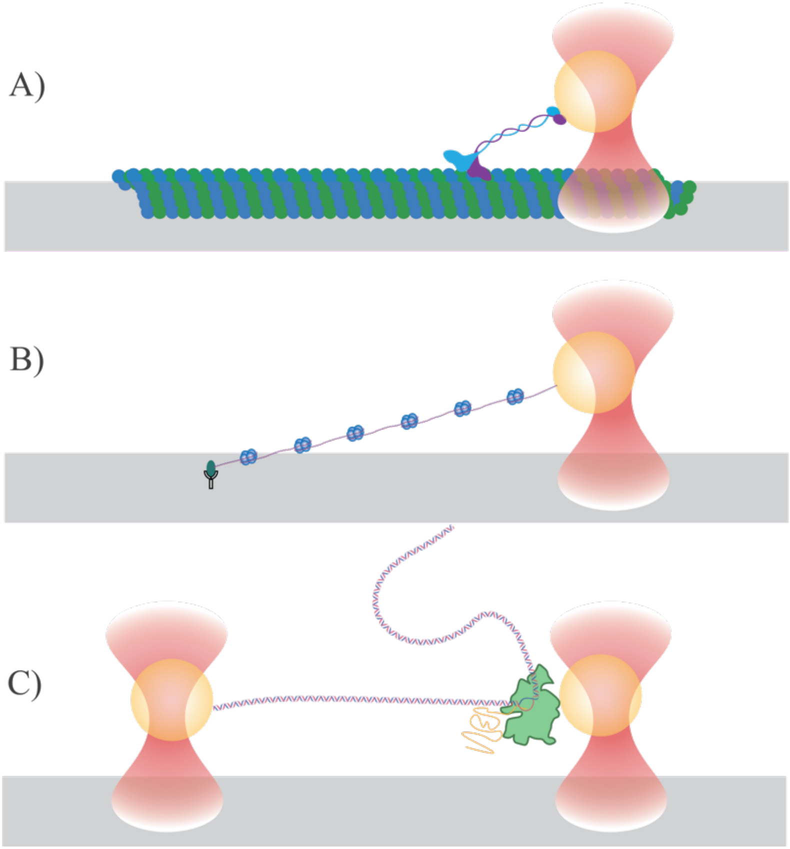

Figure 3-8 Optical Tweezers assays. A) Recognition of step-size and force for single kinesin molecules translocating on a microtubule. Force is acted upon a single trapped bead by a kinesin which could oppose forces up to 5 pN and translocated in 8 nm steps.(adapted from Block *et al.*[27]) B) Alternate single trap geometry of DNA tethered to slide surface and trapped bead. Such setup was used to investigate the dynamic structure of single nucleosomes in an array where disassociation dynamics of DNA from a nucleosome array was investigated. (adapter from Brower-Toland et al.[29]) C) Addition of a second trap to the setup enabled the investigators to observed base-pair stepping by RNA polymerase where discrete steps by RNAP indicate an addition of single base pair per nucleotide to the nascent RNA chain. (adapter from Abbondanzieri et al.[30])

3.3.1.1 Resolution and calibration

The output responsivity (R: voltage per unit displacement) of the QPD is an arbitrarily scaled voltage which must be calibrated. This can be done using piezo drives of the sample stage to scan the position of a stuck particles in the vicinity of the trap center. The QPD output is measure at each known displacement of the particle; thus, mapping the response and translating the voltage read-out into displacement.

Thermal fluctuations in solution results in collisions where solvent molecules continually perturb the location of a trapped particle. Analysis of the thermal motion over trapped particle allows the stiffness to be measured using several methods, two of which namely equipartition theorem and power spectral density (PSD) are discussed here. The equipartition theorem can be used to equate the average potential energy of a trapped particle in each direction with average thermal energy of solvent molecules.

Equipartition theorem: energy of a particle in each degree of freedom is:

$$E = \frac{1}{2} k_B T \tag{3.8}$$

Hooke's law: energy in a spring:

$$E = \frac{1}{2} \alpha < x^2 > \tag{3.9}$$

Which gives trap stiffness α:

$$\alpha = \frac{k_B T}{< x^2 >} \tag{3.10}$$

k_B :	Boltzmann's constant
T :	Temperature
$< x^2 >$:	Variance determine experimentally using R.

The spatial resolution δx is dependent on thermal noise and the corresponding force resolution δF is given as follows[24]:

$$\delta x = \sqrt{\frac{k_B T}{\alpha}} \; and \; \delta F = \sqrt{\alpha k_B T} \tag{3.11}$$

As the power spectrum of the particle displacement fits a Lorentzian, noises beside Brownian noise can be filtered using following relation[24]:

$$S(f) = \frac{k_B T}{\pi^2 \beta (f^2 + f_0^2)} \tag{3.12}$$

where $S(f)$ is power per unit frequency (displacement^{2}Hz^{-1}), $\beta = 6\pi\eta r$ is the drag coefficient and $f_0 = \alpha/2\pi\beta$ is the roll-off frequency.

η : viscosity of the solvent (8.9 x 10^{-4} Pa.s for water)
r : Radius of the particle

Example power spectra are shown in Figure 3-9. The values used are for a 1 μm particle attached to a spring and undergoing Brownian motion with a roll-off frequency (f_0) of 2 kHz (in red). The amplitude of the displacement spectrum decreases at higher frequencies and the two parameters, a roll-off frequency f_0 and a low-frequency intercept P_0 can be determined. Blue and green plots show the power spectra for the same particle at half the drag coefficient (β) and double the stiffness (α) respectively. Both these changes increase the f_0 while decreasing P_0. Area under the curve ($< x^2 >$) and by association, the position noise is reduced by increasing the stiffness. Noise is equivalent for red and blue curve as reduction in P_0 is compensated by an extended f_0. An additional factor; cut-off frequency Δf (100 Hz) can be used to approximate the effect of filtering the position signal where Δf << f_0. By limiting the bandwidth (Δf) as shown in the grey region, a reduction in noise for reduced β and increased α can be seen. The spatial (δx) and corresponding force (δF) resolution is approximated by following relations[24]:

$$\delta x = \sqrt{\frac{4\beta k_B T \Delta f}{\alpha^2}} \; and \; \delta F = \sqrt{4\beta k_B T \Delta f} \tag{3.13}$$

To improve spatial resolution: 1) stiffness (α) can be increased, 2) bandwidth (Δf) can be decreased, 3) drag (β) can be decreased by reducing the size of the probe or viscosity of the medium. Improvement in force resolution is directly proportional to the reduction of drag and bandwidth. However, temporal resolution is inversely proportional to bandwidth (in case of filtering) or roll-off frequency of the Lorentzian (no filtering). Time resolution can be improved by increasing stiffness and reducing hydrodynamic drag on the probe. To maximize all three position, force and time resolution, drag should be minimized. Both calibration techniques discussed here rely on measuring noise accurately and errors are introduced if the position signal is poorly filtered or the technique lacks sufficient bandwidth[24,31].

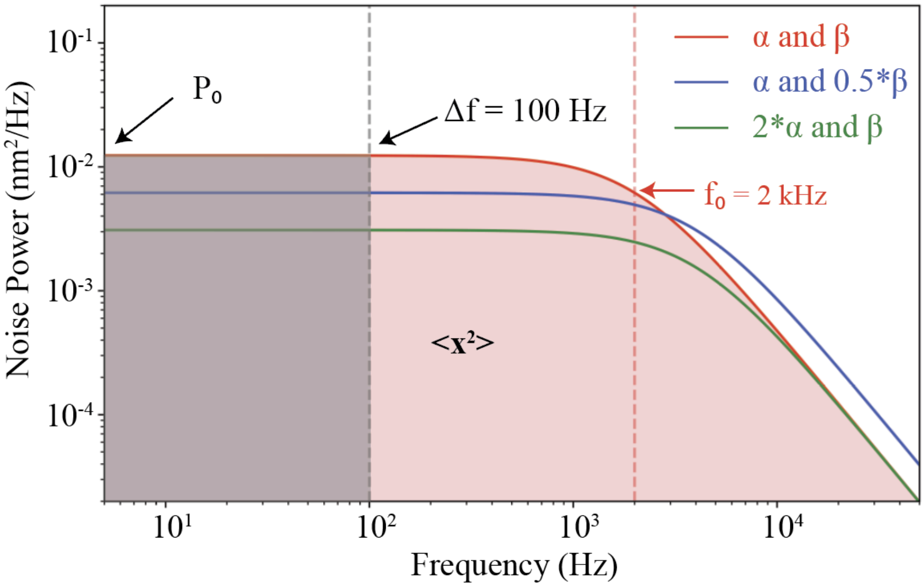

Figure 3-9 Power spectrum for a 1 μm probe and a roll-off frequency of 2 kHz (red). Changing parameters such as stiffness (α) and drag coefficient (β) lead to change in low-frequency amplitude (P_0), the roll-off frequency (f_0) and the area under the curve ($< x^2 >$). For the same particle, if β is halved (blue) or α is doubled (green), an increase in f_0 and a decrease in P_0 can be seen. $< x^2 >$ is reduced only when α is doubled, it remains similar for the blue and red curves as the decrease in P_0 is compensated by an increase in f_0. Denoising can be achieved by setting a cut-off frequency (Δf) as shown here where the bandwidth is limited to 100 Hz. Grey shaded area shows a reduction in position noise for both blue and green plots. (adapted from Neuman and Nagy[24])

The power spectrum of thermal excitation is constant over the frequency range of interest. However, response of stiffness (α) and viscous damping (βv where v is particle velocity) taken together is a function of frequency.

$$P_x = \frac{P_0 f_0^2}{f^2 + f_0^2} \tag{3.14}$$

Area under the curve (Parseval's theorem) for the power spectrum plot gives the variance $<x^2>$.

$$\int_0^\infty \frac{P_0 f_0^2}{f^2 + f_0^2} = < x^2 > = \frac{\pi}{2} P_0 f_0 \tag{3.15}$$

The QPD output (V: voltage) is related to the variance by calibration factor R.

$$< x^2 > = \frac{1}{R^2} < V^2 > \tag{3.16}$$

Shown in Equation (3.11):

$$\frac{\pi}{2}\frac{P_{0,V}}{R^2} f_0 = \frac{k_B T}{\alpha} \tag{3.17}$$

Solving for R:

$$R = \sqrt{\frac{\pi^2 \beta f_0^2 P_0}{k_B T}} \tag{3.18}$$

Stiffness $\alpha = 2\pi\beta f_0$ is calculated by transforming a time series of position samples into a power spectral density.

Optical Tweezers (OT) offer a force range from 1nN down to 0.1 pN. The lower limit is imposed by the necessity for a stable trap and a sufficiently high trap stiffness. Torque can also be applied to the cylinders using a variety of methods, such as polarization of the trapping laser or formation of a helical waveform[32,33]. This however, further complicates an already complex setup where similar control can easily be achieved using magnetic tweezers.

3.3.2 Magnetic Tweezers

Following innovations in OT and use of magnetic beads to measure the elasticity of DNA molecules[6], magnetic tweezers (MT) were invented in 1996 by Strick, Bensimon and Croquette[34]. It is constituted by a DNA molecule multiply-tethered to the extremes of a glass slide and a paramagnetic bead (Figure 3-10). This bead can be manipulated using the gradient of magnetic field and offers a homogeneous force field. Proximity of the magnets to the bead increases the force on the biomolecule $\vec{F} = \frac{1}{2}\vec{\nabla}(\vec{\mu}.\vec{B})$ and rotation of the magnetic field gradient causes rotation which can be used to manipulate the topology of the molecule among other processes. The microspheres comprise of Fe_2O_3 particles embedded in a polystyrene sphere. These nanoparticles have separate magnetic domains which are randomly oriented and have no net magnetization unless upon acted by an externally applied field $\vec{B}$. With increasing field gradient, the magnetization aligns with the field resulting in net magnetization of the microsphere. Theoretically, this effect reaches saturation when all the domains perfectly align with external field. Practically however, due to anisotropy in the magnetization of the bead, a minor component of the magnetic moment μ_0 is not aligned with $\vec{B}$ thus generating torque τ in the bead $\vec{\tau} = \vec{\mu}_0.\vec{B}$.

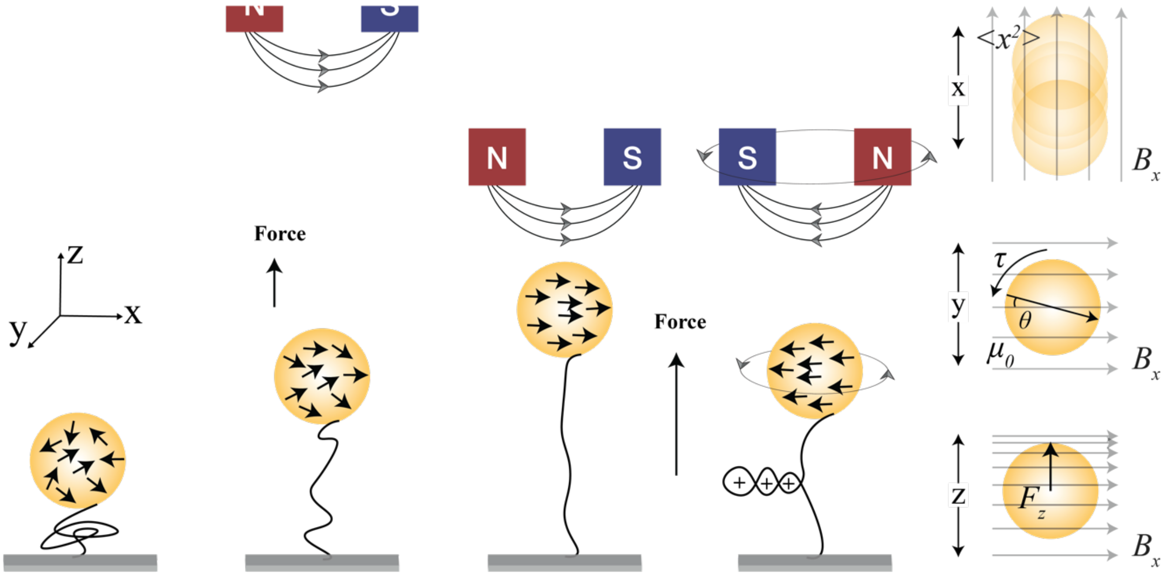

Figure 3-10 Principle of Magnetic Tweezers. A paramagentic bead is tethered to the surface and proximity of the magnetic field gradient determines applied force on the DNA as the bead is attracted towards the

region of highest magnetic flux density as shown in z-axis point of view (POV). In absence of an external magnetic field, magnetic domains are randomly arranged. As the field gradient increases, the domains align themselves with the field and the bead gains a net magnetisation until they reach a saturation magnetisation. A slight misalignment in a magnetisation of the magnetic bead from the background B_x field gives rise to torque as shown in the y-axis POV. The x-axis POV displays the transient excursions of the bead which are used to calculate the variance and resulting force on the molecule.

A typical MT setup consists of an inverted microscope and monochromatic illumination which are used to track diffraction pattern of the beads using video microscopy to determine bead position along x, y and z axes (Figure 3-11 A). Conventional MTs employ permanent cubic magnets to produce a horizontal magnetic field where preferred magnetization axis of the bead aligns tightly with the field; locking its rotational motion. This enables users to precisely control the twist applied to the nucleic acids as the rotational angle of the bead barely deviates from its equilibrium position. Cylindrical magnets on the other hand apply a vertical magnetic field along the tether axis leaving the bead rotation unconstrained while still retaining force application on the bead. One such setup is the freely orbiting MT (FOMT) where the bead fluctuations in the XY plane trace out a doughnut shape with only the nucleic acid tether constraining the bead rotation (Figure 3-11 B) as compared to conventional MT where the XY movement of the bead is strongly confined. FOMT allows measurement of equilibrium fluctuations and change in twist of tethered molecules by monitoring XY fluctuation pattern and changing the information to radial and angular coordinates[35]. This act as a way to measure said twist without bias on the molecule from a constrained bead. A slight modification in the magnet geometry can be made by attaching side magnets to the FOMT geometry which create horizontal magnetic fields (Figure 3-11 C). This kind of geometry gives rise to weak angular traps that enable torque measurements and hence called Magnetic Torque Tweezers (MTT)[36]. The horizontal component weakly constrains the bead rotation which traces arc-shaped patterns in the XY-plane. Following torque application on the nucleic acid, a restoring torque is applied by the molecule shifting the equilibrium angular position by angle $\Delta\theta$ which can be detected due to lower stiffness of the torsional trap. A change from cartesian coordinates to polar coordinates of these readings yield a direct measurement of torque on the molecule.

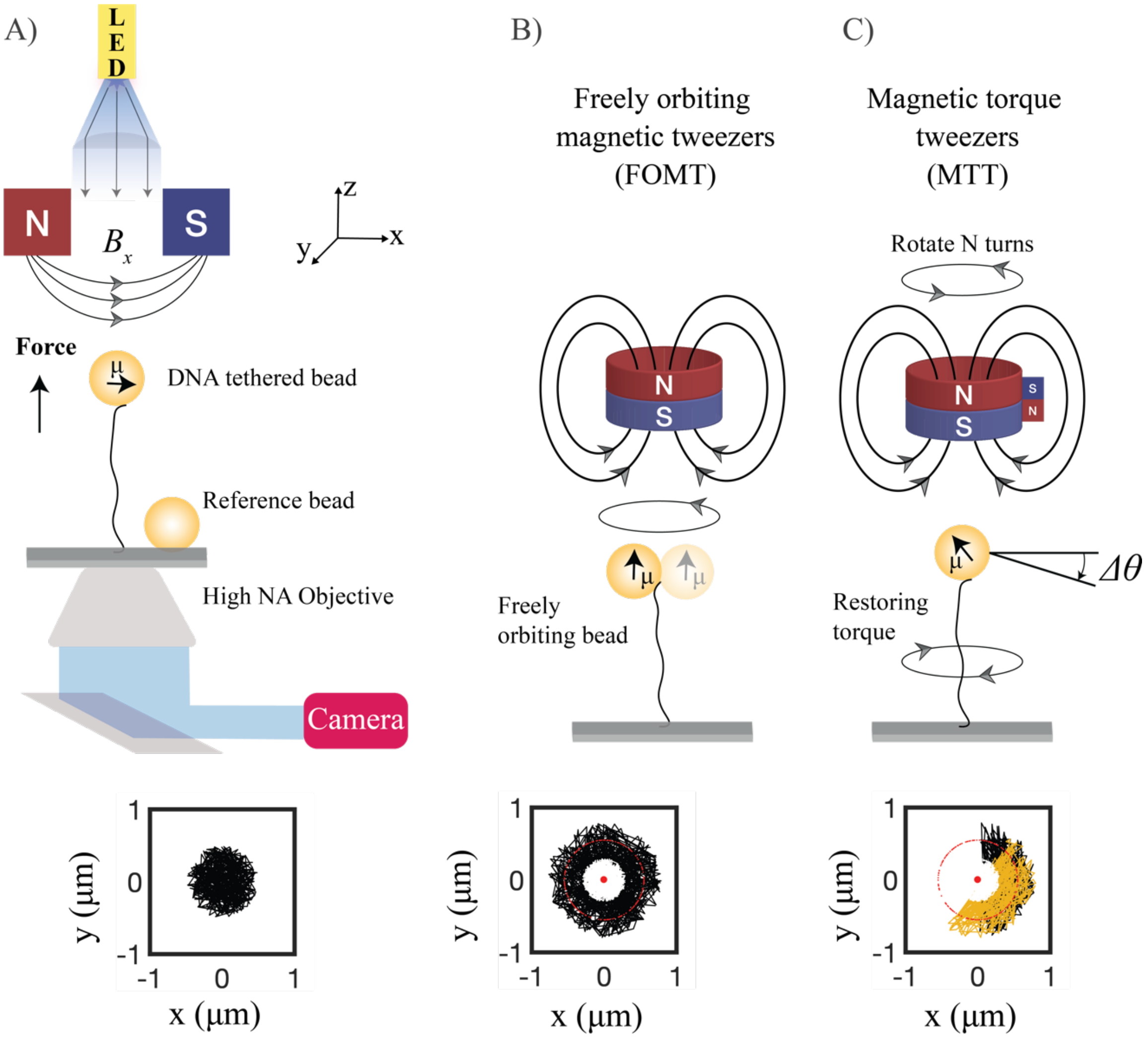

Figure 3-11 Setup of Magnetic Tweezers and different magnet geometries. A) A typical inverted microscopy setup for MT with reference bead attached to the surface for drift correction. Conventional magnet geometry consists of antiparallel magnets that create a horizontal magnetic field pulling the bead in direction of the field gradient and also constraining rotation of the bead as seen from bead-fluctuations in XY-Plane. B) Cylindrical magnets in FOMT create a vertical field allowing for free rotation of the bead where it traces a circular annulus in the XY-plane from which the rotation angle can be elucidated. C) Addition of a side magnetic in MTT imparts a weak horizontal magnetic field thus traces an arc in the XY-plane. Shift in position of the arc enables torque measurements on the molecule. (adapted from Strick et al.[34] , Lipfert et al.[35,36] and Kriegel et al.[37])

MT is thus a versatile and straightforward technique with a potential for high throughput owing to a homogeneous magnetic field over a larger area as discuss in later chapter about high-throughput methods. The force ranges from as low as a Brownian force (femtonewton range) to about 100 pN. Easy application of external torque is a strength of this method as compared to other force spectroscopy techniques. With addition of geometries such as FOMT and MTT to the magnets, twists and torques on the tethered molecules could be directly measured. One major drawback of MT as compared to OT is its bandwidth and sensitivity due to its video-based detection of displacement of the bead. Nonetheless, the method has made technological and theoretical leaps in the two decades since it was discovered and proves to be an integral part of force spectroscopy toolbox.

3.3.2.1 Force calibration and corrections

In most setups, as the chamber is mounter atop an inverted microscope and tethered bead is pulled vertically upwards, changes in tether extension is observed through well-defined concentric rings formed by out-of-focus beads as compared to a fiducial marker. Analysis of these rings point towards a change in tether extension.

In general, the basics of force-extension relation remain similar across platforms and the calibrations and methods applied in OT (discussed in Resolution and calibration section) apply to MT as well. These derivations are discussed in significant details elsewhere[38,39]. Here, the OT calibrations are complemented a bit with further corrections.

Due to Brownian motion, the tethered bead in a magnetic field is forced out of its equilibrium position and restored again due to restoring force by the nucleic acid. Average potential energy E_p in direction of the magnetic field (here x) is given by:

$$E_p = \frac{1}{2} \cdot \frac{F}{l} \langle \delta x^2 \rangle \quad where \quad \frac{F}{l} = \alpha \tag{3.19}$$

α is the effective trap stiffness and $\langle \delta x^2 \rangle$ the variance of bead excursions as shown in equations (3.8) - (3.10).

As shown in equation (3.10), force is given by:

$$F = \frac{k_B T\, l}{\langle \delta x^2 \rangle} \tag{3.20}$$

For forces > ~1pN, the measurement of variance in real space shows a systematic error which can be resolved by a more accurate determination of variance in Fourier space by integrating the power spectrum of the bead motion (see Resolution and calibration).

$$\langle \delta x^2 \rangle = \frac{1}{2\pi} \int P(\omega) d\omega \tag{3.21}$$

There is however another obstacle while observing microsphere displacement as position determination is susceptible to deleterious effects of long camera integration time, low frame-rate and interlacing. This motion blurring leads to averaging of instantaneous positions x_m sampled by the bead instead of actual position x and overestimation of forces.

$$var(x_m) = var(x)\left(\frac{2}{\gamma} - \frac{2}{\gamma^2}(1 - e^{-\gamma})\right) \tag{3.22}$$

$\gamma = W\alpha/\beta$ is the dimensionless exposure time which equals the product of integration time of the camera W and inverse of the trap relaxation time which consists of the quantities α = trap stiffness and β= drag coefficient.

3.3.3 DNA flow stretching

The concept of immobilizing DNA molecules on a surface and exerting force on the other end was taken further by van Oijen *et al.* in 2003 where a laminar flow of aqueous buffer was used to transfer momentum from fluid to an attached bead[40]. DNA is tethered to the surface of a flow chamber and to a polystyrene bead whose viscous drag exerts force on the molecules. The drag force F_{drag} is determined by the width and height of the flow chamber as well the fluid velocity (Figure 3-12 A). Combining flow-stretching with low-magnification wide-field optical microscopy substantially improves data-throughput and statistics by observing multiple DNA molecules at once. The force due to stokes drag on the sphere can be calculated using $F_{drag} = 6\pi\eta r v$. Where η is the fluid viscosity, r is the bead radius and v is the fluid velocity (Figure 3-12 B).

Additionally, elastic properties of DNA were exploited and were integral during initial enzymatic experiments with flow-stretching. Force-extension behavior of single-stranded DNA (ssDNA) and double-stranded DNA (dsDNA) (Figure 3-12 C) vary due to differences in their fundamental structure which can be parametrized by bending persistence length P. Shorter P means lesser energy is required to bend a polymer. With P at around 50 nm for dsDNA[7] and 0.8-3 nm for ssDNA[41] with strong dependence on the ionic content of the buffers. Polymers with a shorter P tend to adapt a compact coiled structure where end-to-end distance is much shorter than its contour length. This property stems from entropic elasticity of polymers as compact molecules can sample more potential configurations and this number decreases as the molecule is stretched. While stretching ssDNA, thermal fluctuations prevent the polymer from being extended more than dsDNA which in turn leads to a difference in forces needed to de-compact DNA (Figure 3-12 D).

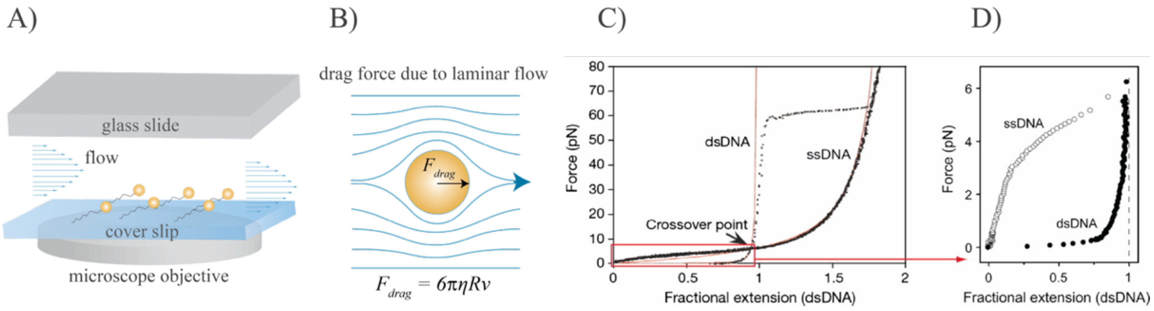

Figure 3-12 Setup and principle of DNA flow stretching. A) Multiple DNA molecules are tethered to the slide surface and polystyrene beads (adapted from van Oijen *et al.*[40]). B) Under influence of laminar flow, the DNA stretches as drag is applied to the bead. C) Force-extension data from ssDNA and dsDNA (taken from van Oijen[42]). A crossover point marks the forces above which ssDNA extends more than dsDNA. Also shown here in red is the worm-like chain fit of dsDNA extension at incrementing forces (adapted from Wuite *et al.*[43]). D) At lower forces below the crossover point, ssDNA is shorter than dsDNA. This fact can be exploited the study enzymes that catalyze conversion between duplex and single stranded and hence lead to length changed in DNA (adapted from Lee *et al.*[44]).

Enzymatic conversion between dsDNA and ssDNA at a constant force can be calculated as the total length of a molecule contains both dsDNA and ssDNA and can be describe as a linear sum of the both forms combined: $L_{total}(F) = N_{ds}I_{ds}(F) + N_{ss}I_{ss}(F)$ where $L_{total}(F)$ is the total extension at force F, N is the number of nucleotides in dsDNA/ ssDNA, and I is the length of a single nucleotide for dsDNA/ ssDNA. As the total number of nucleotides for a molecule remain constant, the measured length change $\Delta L(F) = \Delta N\ (I_{ss}(F) - I_{ds}(F))$ gives double-stranded basepairs converted to single-stranded basepairs (or $\Delta N\ \left(I_{ds}(F) - I_{ss}(F)\right)$ for conversion of ssDNA to dsDNA).

This property of change in DNA length was used to study DNA digestion by λ exonuclease while flow stretching a tethered molecule (Figure 3-13 A)[40]. As the dsDNA was digested, resulting ssDNA compaction led to a change in the tethered bead's relative position. This can be translated to calculate basepairs digested and study dynamics of the enzyme. The high throughput capability of this setup was used to study multi-protein processes such as DNA replication[44-46]. An example assay shows modified DNA construct with a primed strand and a partial replisome synthesizing leading strand while the non-replicated lagging strand compacts analogous to the exonuclease experiment (Figure 3-13 B). This gives a readout of the rate at which DNA polymerase incorporates nucleotides which replicating DNA. This assay while used for numerous further studies of replication, can be modified further by an additional bead attached to the leading strand[47]. This enables users to simultaneously monitor leading and lagging strand synthesis as dynamics at replication fork is complex and has to be coordinated (Figure 3-13 C). Synthesis can be monitored by observing the motion of bead B tethered to the leading strand. Synthesis of lagging and completion of okazaki fragments on the other hand leads to looping motion of both bead A and B in direction opposite to that of leading strand synthesis.

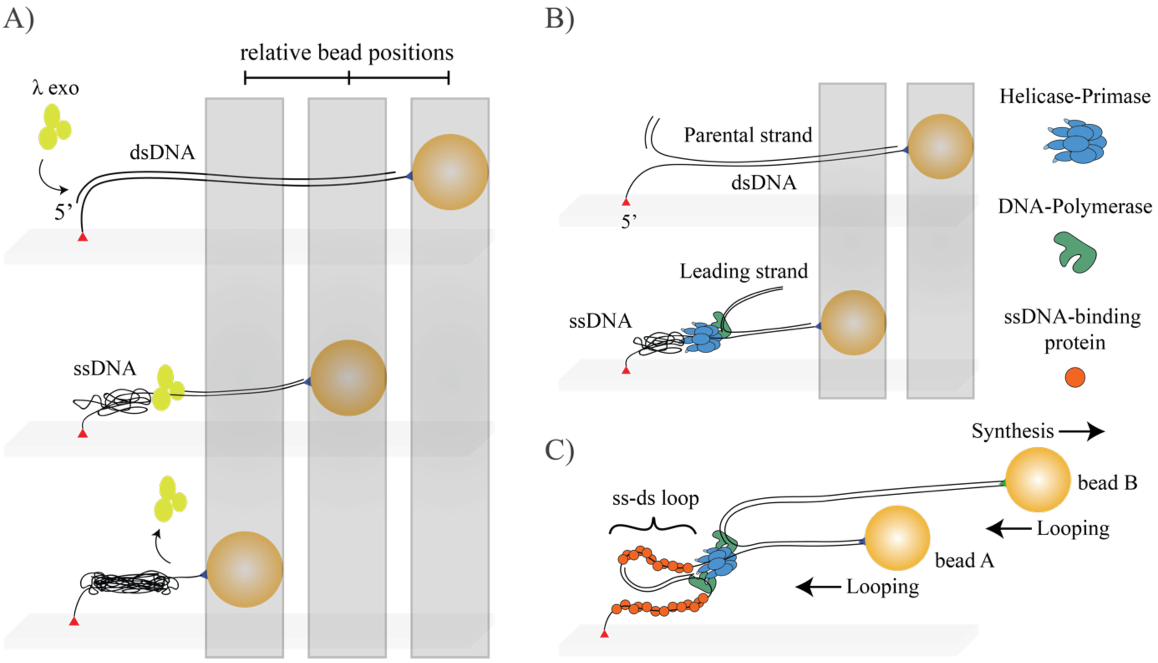

Figure 3-13 DNA flow stretching to study enzyme dynamics. A) A λ exonuclease digesting dsDNA and converting it to ssDNA. ssDNA compacts more than dsDNA at forces lower than ~6pN through entropic forces. This compaction can be detected as relative change in bead's position (adapted from van Oijen *et al.*[40]). B) Modifications can be made to the DNA substrate to make a primed fork for a partial replisome to synthesize leading strand while translocating along the parental strand (adapted from Lee *et al.*[44]) As the lagging strand is not synthesized, ssDNA compacts here analogous to the exonuclease assay. C) Two-bead assembly can be used to study dynamics of a full replisome and coordination of leading and lagging strand synthesis. DNA replication leads to an extension of the leading strand and corresponding movement of bead B during synthesis. Lagging strand synthesis on the other hand leads to a loop formation during completion of okazaki fragments. This results in compaction of both bead A and B before the loop is release again (adapted from Duderstadt *et al.*[47]).

3.3.4 Hybrid methods

The single-molecule techniques stated have unique merits and these can be used in concert to overcome their limitations. As any method facilitates how one approaches studying a biological question; following are some examples of studies where instruments were combined to exploit the potential of existing methods in the field.

DNA supercoiling dynamics play an important part in various cellular processes and these were studied by Crut *et al.* by combining MT with OT[48]. Here, the ability to twist DNA and retaining the ΔLk is provided by MT whereas OT acts as a near-instantaneous force switch that operates on millisecond time range (Figure 3-14 A). Force on the DNA initially imposed by MT is reduced by optically trapping the bead and moving it towards the surface. As the magnets are held fixed after initial application of supercoils, the dynamics between Tw and Wr depends on the tension along the DNA. Hence, this study investigated fast structural transitions of single DNA molecules and determined that plectoneme removal does not influence elongation kinetics of DNA[48].

Fluorescence microscopy can be used to study single molecules by tagging them with a fluorophore. Once this fluorophore is excited with light of a specific wavelength, it emits light of a longer wavelength which can be detected by the camera. Combining this technique with force spectroscopy not only enables the user to study local structural information of biomolecules but also gives access to global mechanical information. One such setup was used to study force-induced strand separation of dye-labeled dsDNA[49]. Confocal fluorescence microscopy however, suffer from resolution constraints imposed by the diffraction limit of the light. This hinders resolution of a multitude of biological structures, the majority of whom have size scales much smaller than the wavelength of light used. Super-resolution techniques such as Stimulated emission depletion (STED) microscopy overcome this barrier by selectively deactivating fluorophores using a depletion beam, minimizing the area of illumination at the focal point (Figure 3-14 B). STED was combined with a dual-trap OT setup to visualize DNA-binding proteins on a densely coated DNA[50]. This study achieved a sixfold resolution improvement over that of confocal microscopy as well as high temporal resolution ensured by fast one-dimensional beam scanning.

Single-molecule Förster resonance energy transfer (smFRET) is a technical equivalent of an Ångström scale ruler. This fluorescent method relies on distance dependent nonradiative energy transfer from a donor fluorophore to an acceptor fluorophore (Cy3-Cy5 pair in Figure 3-14 C). The efficiency of this transfer is inversely proportional to the sixth power of the distance between donor and acceptor making FRET extremely sensitive to small changes in distances. The sample is placed in a total internal reflection fluorescence (TIRF) setup, where incident light induces an evanescent wavefront illuminating a thin volume (~100 nm) above the slide surface. B-Z DNA transitions in short guanine/cytosine (GC) repeat region were studied by Lee *et al.* by combining smFRET with MT where this transition occurred at low negative superhelicity and low tension[51]. The GC-core in the DNA is flanked by donor and acceptor dye which can be used to monitor its conversion from B- to Z-DNA and vice-versa. DNA when in B-conformation has a high FRET efficiency. Once this strand is underwound, at a predetermined tension, the GC-core inverts its helical sense and expands; thus, lowering the FRET efficiency. This inversion also absorbs negative linking difference and reduces the effective ΔLk of the molecule leading to its extension. This hybrid single-molecule approach thus shed light on the transition mechanism.

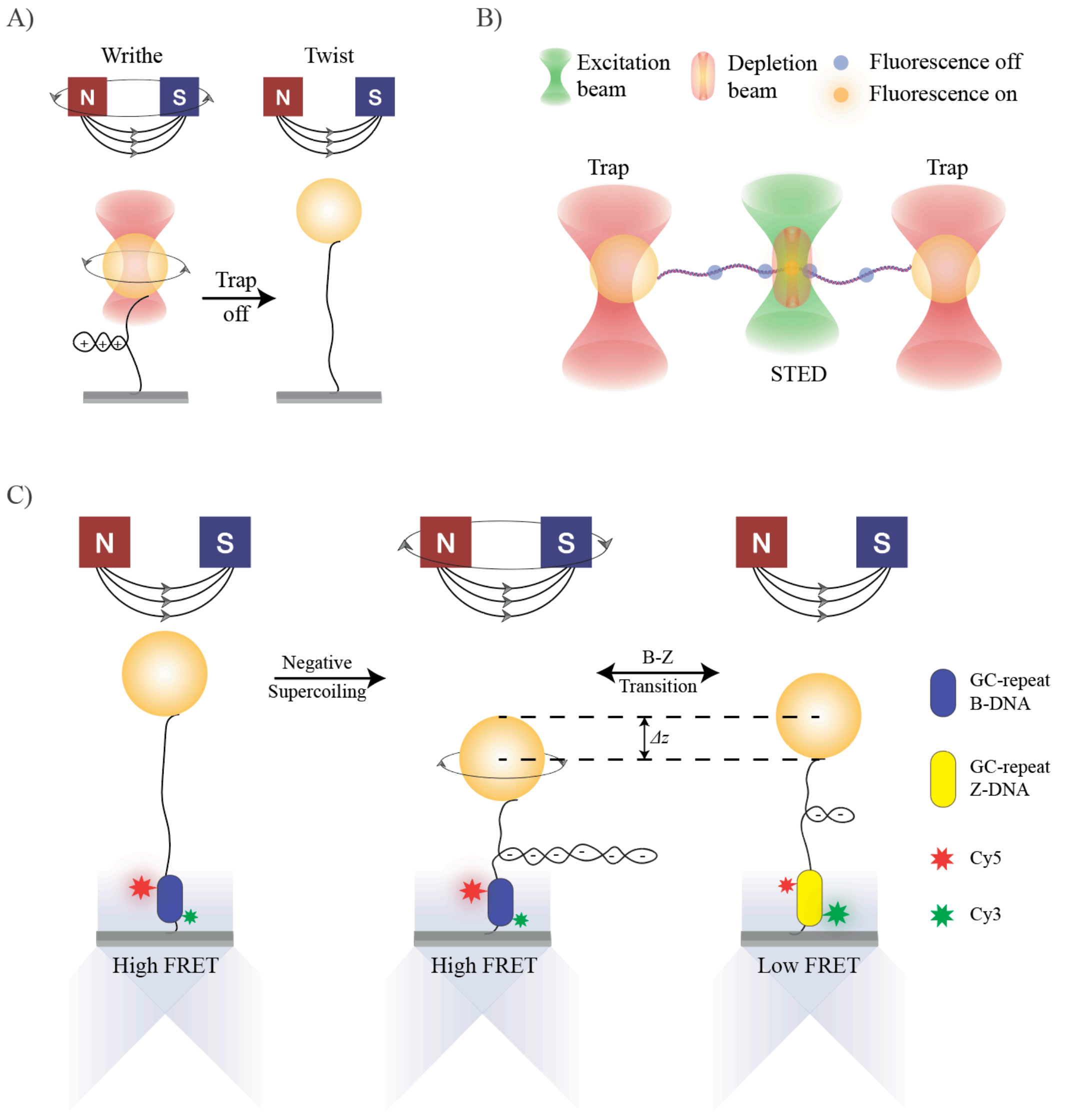

Figure 3-14 Different hybrid methods to study biological problems. A) Stretching experiment with supercoiled DNA molecules using hybrid MT-OT. DNA is twisted and the bead is trapped to lower the end-to-end distance. This lowered tension results in formation of plectonemes. Force can be turned off instantaneously by turning off the trap. Dynamics of writhe conversion to twist at higher tension can then be studied (adapted from Crut *et al.*[48]). B) Protein visualization on a dual-trap OT using STED. A DNA

molecule is stretched using two trapped beads where labeled DNA-binding proteins accumulate on the strand. The excitation beam along with the depletion beam can then be scanned on the strand and single-proteins resolved (adapted from Heller *et al.*[50]). C) Studying B-Z DNA transition using smFRET combined with MT to regulate tension and torsion on the molecule. The GC-core in the DNA strand is flanked by a donor (Cy3-green) and acceptor (Cy5-red) dye and underwound using MT. The change of FRET efficiency from high to low indicates conversion of B-form to Z-form DNA. This transition also removes plectonemes, increasing the extension by Δz (adapted from Lee *et al.*[51]).

3.4 High-throughput methods

Single-molecule methods developed in the past decades and discussed in the previous section have revolutionized the way biomolecular studies are conducted. These however were performed on instruments where mostly one molecule could be studied at a time, impeding the rapid collection of statistically significant datasets. The trend in past decade shifted towards higher-throughput methods as heterogeneity in molecular behavior and probabilistic nature of enzymes called for robust data acquisition and interpretation strategies.

3.4.1 Highly parallel magnetic tweezers

Magnetic Tweezers as a method are intrinsically high-throughput as the B field is relatively uniform over large areas spanning several mm. Potential bottle-neck here is set by the camera detector's field-of-view (FOV) as high-NA objectives lenses are required for high-axial resolution to observe length changes. As FOV is limited, an alternative to increase data acquisition could be to densely pack the molecules of interest in a given FOV. In standard MT approach, surface is coated with DNA-end-binding labels that are randomly distributed and maximum achievable number of useful tethers can be calculated from probability density of finding nearest neighbor at a distance that is far-enough to avoid crosstalk in position tracking as well as irreversible pull-in of DNA-tethered beads due to magnetic dipole-dipole coupling. The number of productive tethers can be calculated using following equation[52]:

$$N_{bead} = A_{FOV}\,\rho \int_{d_0}^{\infty} \omega(r)dr = A_{FOV}\,\rho\, e^{-\rho\pi d_0^2} \tag{3.23}$$

Where A_{FOV} is the area of field-of-view, ρ is the surface density of tethered beads and $\omega(r)$ denoted the probability density with $\omega(r) = 2\rho\pi r\, e^{-\rho\pi r^2}$ (productive tethers defined as r > d_0).

A regular distribution of beads on the other hand results in a much higher stacking density as displayed in Table 3-1.

Table 3-1: Comparison is different distributions and maximum bead numbers.

	Random	Square	Hexagonal
Maximum number of beads for a given field	$\frac{A_{FOV}}{d_0^2}\frac{1}{\pi e}$	$\frac{A_{FOV}}{d_0^2}$	$\frac{A_{FOV}}{d_0^2}\frac{2}{\sqrt{3}}$
Relative improvement	1	$\pi e \approx 8.5$	$(2/\sqrt{3})\pi e \approx 10$

Under random distribution, DNA-tethered beads diffuse and tether to the surface at arbitrary points. In comparison, a periodic placement of beads in square or hexagonal pattern leads to an improved density of surface tethered by a factor of 8.5 and 10 respectively. This is an order of magnitude improvement over randomly distributed tethers (Figure 3-15 A).

Regular arrays of DNA-tethered magnetic beads via surface patterning were employed by De Vlaminck *et al.* in their 2011 study[52]. The protocol as described in Figure 3-15 B) involves etching a negative pattern on a silicon surface using electron beam lithography. An elastomer such as polydimethylsiloxane (PDMS) is coated with required protein and pressed against the silicon template leaving the desired protein pattern on the PDMS stamp which in turn is pressed onto a glass slide. The surface is then passivated to avoid undesired DNA sticking and ultimately arrays or tethered beads are created on the pattern. The authors could perform measurements of mechanical parameters of up to 357 dsDNA molecules in a single experimental run using this technique for an imaging system with 25x optical magnification and a 1.4-megapixel camera resulting in a 300 μm x 400 μm FOV.

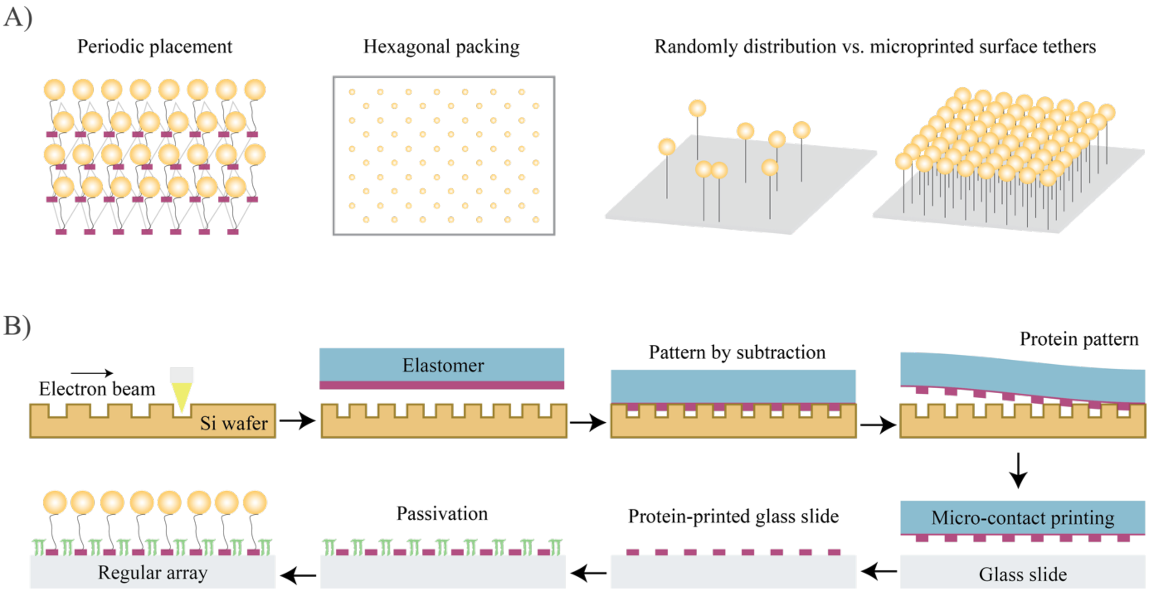

Figure 3-15 Principal and methodology to achieve high surface coverage via micro-contact printing. A) Regular arrays of DNA-tethered beads greatly increase the achievable data-throughput. The 2D view shows hexagonal packing of beads as observed using video microscopy. Random diffusion and tethering of beads have lower yields of tethers as compared to periodic placement where the yield of usable tethers is an order of magnitude higher. B) A negative pattern is etched onto a silicon wafer using electron beam lithography. A PDMS surface is coated with desired protein and the pattern is transferred by pressing the PDMS against the Si-wafer. This pattern is then stamped onto a glass slide and passivated for final patterned array of tethers. Figure adapted from De Vlaminck *et al.*[52]

3.4.2 Centrifuge force microscopy

In a miniature centrifuge force microscope (CFM)[53], a benchtop centrifuge (Figure 3-16 A) is repurposed by integrating a camera, objective, battery, LED and the sample in a centrifuge bucket (Figure 3-16 B) and rotated to apply force on the sample. To authenticate the single-molecule data obtained, DNA nanoswitches are used. Temperature-dependent unzipping experiments are performed using these constructs where the molecule switches between a looped and unlooped state as a signifier of a rupture and re-ligation events (Figure 3-16 C). The change in tether length were projected onto the xy-plane of the coverslip (ΔL_{obs}). As the direction of force application could be controlled by mechanically constraining the angle of the bucket, the actual length changed (ΔL) could be calculated by dividing ΔL_{obs} by cosine of the bucket angle (Figure 3-16 D).

CFM proves as a cost-effective and easily-implementable multiplex method to characterize nucleic acids with single molecule precision. It has a force range (~0.1 to 100 pN) and spatial resolution (~2 nm) comparable to that of other modern single-molecule methods[53]. However, studies of enzymatic reactions using CFM are yet to be performed. Limitations of this method include small FOV (200 µm x 180 µm), sealing of the sample chamber restricting buffer exchange and lack of topological control over the molecules.

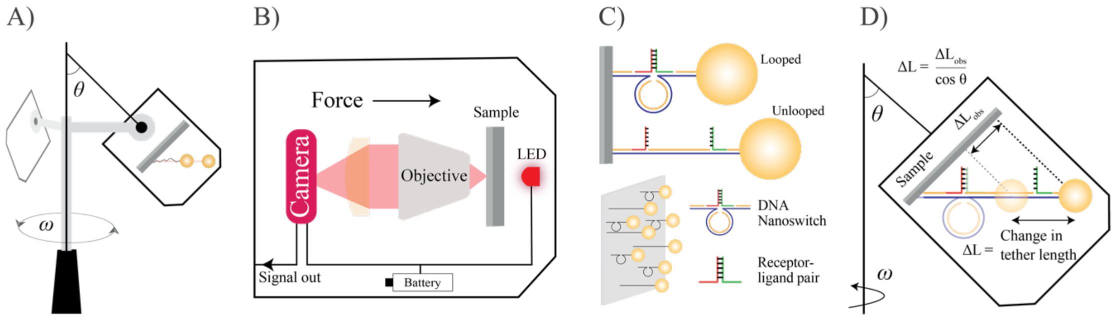

Figure 3-16 Setup of a benchtop CFM and rupture experiment using DNA nanoswitch. A) Rotation of the bucket induces forces on molecules tethered between coverslip and attached bead. B) Schematic of a CFM shows integrated camera, objective, sample chamber, LED and battery. C) Schematic of the nanoswitch shows the unzipping construct where complementary oligos shows here in red and green hybridize to form a loped switch. Application of force can unzip this construct resulting in a measurable increase in tether length. D) Tether extension measurements using projection in xy-plane. Change in tether length (ΔL) can be calculated using observed lateral shift in bead position (ΔL_{obs}) and bucket angle (θ). All figures adapted from Yang *et al.*[53]

3.4.3 Acoustic force spectroscopy

Acoustic force spectroscopy (AFS) displayed a novel method to stretch molecules tethered between surface and a bead[54]. An inverted setup with objective, camera and LED were used to image the microspheres (Figure 3-17 A). The flow cell consists of a piezo element driven by an oscillating voltage that excites a standing planar acoustic wave over a flow cell. The bead under the influence of this wave experiences force along the vertical axis (z-direction). A thin aluminum layer serves as a mirror and allows bright-field microscopy in epiconfiguration. The flow chamber is sandwiched between a top and a bottom glass layer. Different layers such as the piezo, glass and fluid here serve as transmitters of the acoustic pressure. The impedance of each of these layers is determined by their density and speed of sound in the medium. The quality factor accounted for dampening and other losses throughout the acoustic device. As the standing wave transmit unidirectionally, a 1-D acoustic model was employed here to calculate quantities such as resonance frequencies, acoustic pressures and velocities along different layers this determining the final values at the plane of interest in the flow chamber. Theoretical predictions of acoustic energy (Figure 3-17 B) and acoustic forces (Figure 3-17 C) yielded frequencies to apply tension to biomolecules either away (6.8 MHz) or towards (9.2 MHz) the tether plane. When no acoustic force is applied, the bead observes tethered particle motion profile. Driving piezo at 9.0 MHz drives the bead toward the tether plane and at frequency 6.7 MHz; away from the plane and hence increases tension on the DNA tether as seen from the x, y and z traces of the bead (Figure 3-17 D)

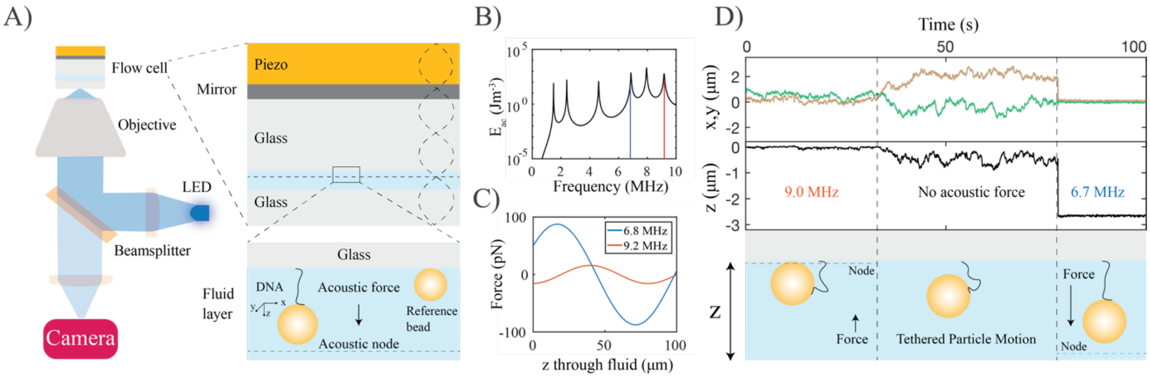

Figure 3-17 Setup and principal of AFS. A) An inverted microscope with objective, LED and beamsplitter is used to image beads in the FOV. The acoustic force device is integrated in the flow cell and the flow chamber lies between two glass layers with a sputtered layer of aluminum illuminating the bright field (adapted from Sitters *et al.*[54]). B, C) Theorical prediction of relevant frequencies from acoustic energy and force respectively (plotted from source data[54]). D) Trace of bead movement in x, y and z. At 9.0 MHz, the bead is pushed towards the surface. When no force is applied, the bead displays tethered particle motion. At 6.7 MHZ, the bead is pushed away from the surface (plotted from source data[54]).

In the tradition of force spectroscopy experiments, force-extension behavior of DNA was investigated in this study. The experimental curves were well described by the extensible WLC model. To test for the effects of protein binding on mechanical properties of DNA, RecA protein was tested as this filamentous protein increases the contour length of DNA by 1.5-fold. Ultimately, to demonstrate multiplexing capability of AFS, rupture experiments were performed on a 1.1 mm x 0.8 mm field with over 2,000 tracked beads and 145 usable tethers[54].

Similar to highly parallel MT and CFS, AFS provides a force application method suitable for homogeneous force administration over large fields. This study used a 40x objective to calibrate forces and to track beads in all 3 dimensions. For bigger fields of view however, authors switched to a 10x objective, which hinders the measurement of length changes along the z-axis. This limits further applications due to limited FOV as tracking xy-plane here only applies to nucleic acid studies akin to rupture experiments.

4 Flow Magnetic Tweezers

The contents of this chapter (Flow Magnetic Tweezers) and the following chapter (Investigating DNA gyrase dynamics using FMT) have been published in the article "Multiplex flow magnetic tweezers reveal rare enzymatic events with single molecule precision." by Rohit Agarwal and Karl E. Duderstadt in *Nature Communications* **11**, 4714 (2020).

Force spectroscopy techniques have revolutionized functional studies of biomolecules, revealing key intermediates during protein folding[55], the mechanochemical cycles of polymerases and translocases[56,57], and the topological transformations catalyzed by DNA topoisomerases[58,59]. Most of these observations have been performed on instruments in which only one molecule can be studied at a time (i.e. Optical tweezers), impeding the rapid collection of statistically significant datasets. Several approaches have been developed that provide greater multiplexing[53,54,60,61] including Magnetic Tweezers (MT)[58,59,62], Acoustic force spectroscopy[54] (AFS), and Centrifuge force microscopy[53] (CFM). However, all of these methods depend on high axial resolution to observe length changes. This imposes a fundamental limitation in throughput, requiring optics with a high Numerical Aperture (NA), which is only realized for small fields of view at high magnification. Novel approaches that overcome this throughput barrier are needed so that rare events and unexpected behaviors can be distinguished from intrinsic heterogeneity in a statistically robust manner.

Here, a single-molecule DNA topology manipulation platform, flow magnetic tweezers (FMT) is presented, in which the experimental geometry used for magnetic tweezing is reconfigured by a lateral flow force. This transformation removes the high-NA limitation imposed by current force spectroscopy techniques allowing tether length changes to be observed as changes in lateral position in massive fields of view. To calibrate force solely based on lateral position measurements that report on changes in the projected length of individual DNA molecules, a system of equations, involving the equipartition theorem and WLC model, was solved. This approach was independently validated using the known force and topology dependent transitions of DNA.

Table 4-1 throughput of Force spectroscopy techniques

Method	FOV	Topological control	Resolution	Relative FOV	Tracked beads	Final
Flow Magnetic Tweezers (FMT)	15 mm^2 (5.2mm x 3mm)	Yes	21 nm	3000x	50,000	10,000
Acoustic Force Spectroscopy (AFS)[54]	0.89 mm^2 (1.1 mm x 0.8 mm)	No	3 nm	179x	2,000	150
High-throughput Magnetic Tweezers (MT)[60]	0.12 mm^2 (0.3 mm x 0.4 mm)	Yes	3 nm	24x	~800	hundreds
Centrifuge Force Microscopy (CFM)[53]	0.03 mm^2 (0.2 mm x 0.18 mm)	No	2 nm	7x	~1000	-
Magnetic Tweezers (MT)[34]	0.005 mm^2 (83 μm x 64 μm)	Yes	-	1x	1	1

When the field of view was not provided, it was calculated using the magnification, pixel dimensions, and camera sensor size. Strick *et al.* used a 100x objective with a XC77CE Sony camera with 756x581 pixels and a pixel size of 11 μm x 11 μm which generates an estimated field of view of 83 um x 64 um. Yang *et al.* used a 40x objective with a Prosilica GC 2,450 camera with 2448 x 2050 and a pixel size of 3.45 μm x 3.45 μm which generates an estimated field of view is 211 μm x 176 μm. For this study the number of mobile beads was determined using a flow reversal step. Resolutions were determined by tracking stuck beads and correcting for drift.

4.1 Construction and calibration of FMT

To realize the multiplexing potential of combined flow and magnetic force transformations, a large 7x Telecentric Lens (TL), designed for industrial inspection of LCD monitors and microprocessors, was directly coupled to a 29 MegaPixel CCD camera (Figure 4-1 A) generating a field of view greater than 15 mm^2 (Figure 4-1 B). Under typical experimental conditions this field contains around 50,000 beads and offers the theoretical possibility of imaging more than 100,000 randomly arranged beads (Equation (3.23)) simultaneously[52] (Figure 4-1 C). A combination of axial and lateral forces is applied to individual molecules tethered between a coverslip surface and a polystyrene bead at the base of a flow chamber. Vertical force (F_{magnet}) is applied by magnetic tweezers containing two large 1 cm block magnets in a horizontal configuration.[63] With optimal spacing, this arrangement creates a magnetic field parallel to the coverslip surface orienting the superparamagnetic beads so that rotation of the magnets can be used to apply positive and negative torque on the molecules. A lateral drag force (F_{drag}) is applied to the beads using negative pressure at the outlet of the flow cell. A flow sensor provides continuous feedback and allows for programmable changes in flow with millisecond response time.

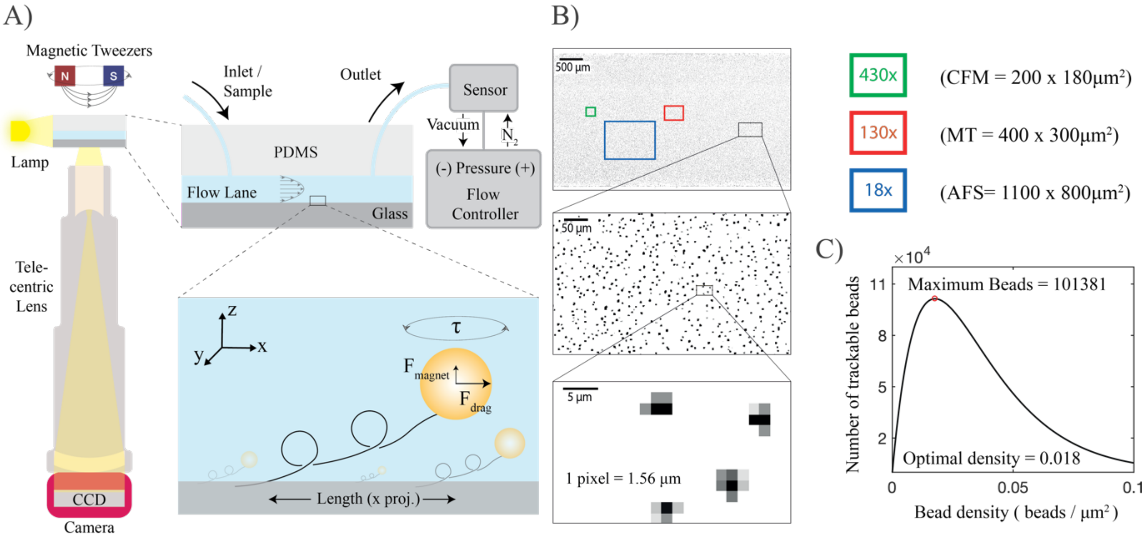

Figure 4-1 Principle of Flow Magnetic Tweezers. A) The flow cell is mounted on a x-y translation stage with a fiber illuminator (Lamp). Beads are imaged with a 7x Telecentric Lens mounted on a 29 Megapixel CCD camera. Antiparallel magnets (MT) are mounted above the flowcell. The flowcell consists of a PEG-functionalized glass coverslip and a PDMS lid with an embedded flow lane. DNA molecules are tethered to the surface using biotin-streptavidin attachment. The total force on each molecule is the sum of the magnetic

force (F_{magnet}) due to MT and drag force (F_{drag}) due to flow. Magnetic beads tethered to the DNA molecules are locked in the magnetic field and linking number of the molecules can be manipulated by rotating the magnets. Manipulation of DNA length and topology can be monitored by tracking beads in the x-y plane. B) A representative field of view (5.2 mm by 3 mm) from a single experiment containing 53,831 microspheres (diameter, 1um) enlarged by 10x and 100x to show individual microspheres. The field size comparison to MT, CFM and AFS is shown. C) . Optimal bead density for random attachment sites. Bead density for maximum number of useful DNA-tethered beads was calculated assuming a random distribution of point-like particles on a 2D plane with ellipsoid profile according to De Vlaminck *et al.*[52] ,where A_{FOV} is the area of the field of view (1.56e+07 μm^2) and ϱ is the bead density (beads/μm^2). More than 100,000 functional tethers could potentially be established for the given field.

Multidimensional force control provides numerous avenues to characterize the physical properties of biomolecules in a massively parallel manner. For example, in the case of double-helical biopolymers like DNA, magnet rotation allows for the introduction of different topologies. Positive (counter-clockwise) rotation induces DNA overwinding and negative (clockwise) rotation induces DNA underwinding. In parallel, applied force can be modulated with flow, including complete reversal of flow direction, revealing the surface attachment location and projected length of individual molecules (Supplementary movie 1). These transformations can be combined to study complex force-extension behaviors. In Figure 4-2 A, vertical force is held constant and magnet rotation is used to over- and underwind DNA. Simultaneously, lateral force is increased in steps using flow. These transformations reveal an asymmetry in force-extension behavior as a function of topology.[64] At low force (< 1 pN), both over- and underwinding of DNA leads to plectoneme formation and compaction in a symmetric fashion. Whereas, at higher forces (> 1 pN), buckling is only observed in overwound DNA (Figure 4-2 B); for underwound DNA, local melting of the helix ensures minimal changes in length.

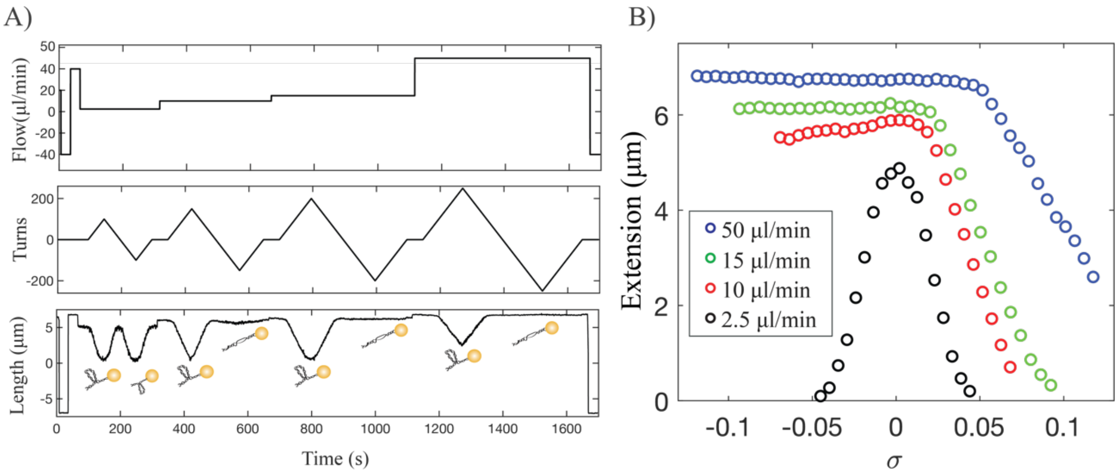

Figure 4-2 Force dependence of length for supercoiled DNA demonstrated by FMT. A) Changes in length are displayed for positive and negative supercoiling states at four flow rates. Negatively supercoiled DNA only compacts at the lowest flow rate, which corresponds to a force below 1 pN. The height of the magnets is held constant. B) The mean length as a function of turns and force for a single molecule displays an asymmetric character where positive buckling is less sensitive to increases in flowrate than negative buckling.

To characterize the force as a function of flow, the flow velocity was increased in steps and the magnet position was held constant. The force can then be calculated with the equipartition theorem given by $F = k_B T l \,/\, <\delta y^2>$ (equation (3.20)), where k_B is the Boltzmann constant, T is the absolute temperature, l is the length of the molecule, and $<\delta y^2>$ is mean-squared displacement of the beads in the direction orthogonal to flow (Figure 4-1 A). The other parameter required for force determination is DNA length. However, the improved throughput of FMT depends on tracking only lateral changes in position. As a consequence, only the projected length is observed. Therefore, both force and length were determined by assuming worm-like chain behavior and numerically solving using the mean-squared displacement $<\delta y^2>$. Importantly, this numerical approach assumes observations were made using dsDNA and assumes a persistence length of 46 nm.[8]

This force calibration approach was validated independently, where the topological control provided by the magnets and biophysical properties of DNA were leveraged. The forces at which over- and underwound DNA buckle are known.[65] Buckling of underwound DNA, shown in Figure 4-2 A & B, occurs at ~ 1 pN. Buckling of overwound DNA has a stronger dependence on the number of turns in the molecule. The buckling transitions in molecules having 150 turns introduced corresponding to a sigma of 0.075 were evaluated. Under these conditions MTT have estimated the positive buckling force to be ~ 6.5 pN.[65] To determine the flowrate for each transition, flow ramp experiments were performed in which flow was reduced or increased gradually (Figure 4-3 A). For both over- and underwound DNA, rapid buckling and extension was observed at distinct flowrates. Transition flowrates, 12.3 ± 0.2 µl/min (median ± s. e. median) for underwound DNA and 76.3 ± 0.8 µl/min (median ± s. e. median) for overwound DNA, were determined in an unbiased manner using a single kinetic change point detection algorithm (Figure 4-3 B, C).[66] In Figure 4-3 D, the flowrate versus force is shown as determined using numerical fitting together with the forces of the known buckling transitions.

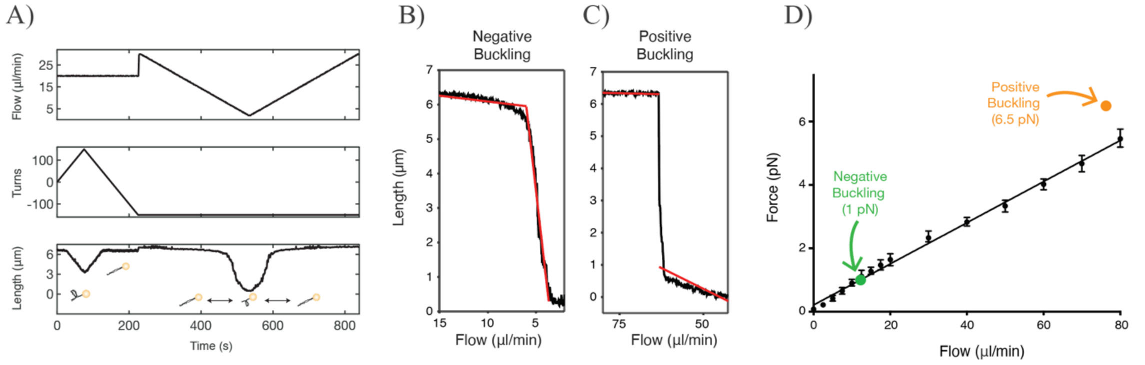

Figure 4-3 Force determination. A) A flow ramp experiment to determine the flow rate where negative buckling occurs. The molecule is singly-tethered and negatively supercoiled at high flow rate (middle panel). The flow is decreased gradually (upper panel) and a buckling transition is seen in the lower panel. B, C) Two-segment kinetic change point fits to determine buckling flow rates for negative buckling (left) and positive buckling (right) transitions. D) The force increases linearly as a function of flow (black points represent the median force). Gray area represents s. e. median. The median negative buckling transition flowrate from a single experiment is indicated in green (s. e. median is within the spot size) (n = 399 molecules). The median positive buckling transition from a single experiment is indicated in orange (s.e. median is within the spot size) (n = 260 molecules). The positive buckling transition is strongly dependent on torque. The measurement was conducted at 150 turns corresponding to a sigma of 0.075. The forces for each buckling transition were set to values from the literature for similar buffer conditions[65] (1 pN for negative buckling and 6.5 pN for positive buckling).

To achieve very high throughput using flow magnetic tweezers some trade-offs were necessary. First, the dramatic increase in imaging area is only possible using a low magnification lens that results in a spatial resolution of 21 nm as determined by calculating the standard deviation of surface-immobilized beads after drift correction. This is 10-fold lower than other force spectroscopy methods (Table 4-1). Second, the large CCD camera needed to capture the very large field of view provides limited bandwidth. As a consequence, the highest frequency fluctuations of individual beads are not captured. A correction factor was applied to the bead fluctuation term to correct for over estimation of the force resulting from motion blur (Figure 4-3 D, Methods).[67] The numerically determined correction factor ranged from 2% at lowest flowrate of 2.5 ul/min (used for all gyrase reactions) to 40% at the highest flowrate of 80 ul/min. Notably, the numerically determined force is in good agreement with the negative buckling transition (Figure 4-3 D, green point) in the low force region but at the highest flowrates the force is lower than that predicted for the positive buckling transition (Figure 4-3 D, orange point). The force estimation at higher flowrates could be improved by using a higher bandwidth camera and increasing the magnetic force. These trade-offs also present challenges for studies involving short DNAs (less than 10 kb). The flow velocity approaches zero near the surface, so applying force on short DNAs would require very high flowrates. Moreover, projected length changes may not be observable due to the spatial resolution limit. DNAs that are 10s of kbs in length are optimal for FMT experiments.

4.2 Microsphere tracking and analysis software

To efficiently process the large datasets generated in FMT experiments, Molecule Archive Suite (Mars) – a high-performance collection of single-molecule analysis plugins for Fiji written in Java was developed. The Mars source code is available under the BSD-2 license and deposited in several repositories on Github (*see* Code availability). Videos were analyzed using Mars as follows. First, a discoidal averaging filter was applied to the images to amplify single beads over background. Second, all beads were detected using an intensity threshold followed by local maximum determination. Third, bead positions were determined with subpixel accuracy by 2D Gaussian fitting. Finally, bead positions were linked from frame to frame to reveal tracks using a local radius search on a KDTree for optimal performance (ImgLib2).[68] These individual steps are combined in a single Peak Tracker command located in the Image package of mars-core.

Tracking results were stored in the Molecule Archive format of Mars together with image metadata, which were saved in either plain text JSON format or with Smile encoding to reduce the file sizes. The coordinates for each bead were stored in molecule records together with parameters (i.e. mean squared displacement, reversal size, etc.), tags, and segments generated using kinetic change point analysis. All molecule records were given Universally Unique IDs (UUID) for reproducible merging of datasets retaining full processing history (further facilitated by logging of all operations within the Molecule Archives). The results of one FMT experiment yielded Molecule Archives that were 10-20 GB in size. Subsequent merging of multiple archives increased the storage requirements further beyond the memory of normal desktop computers. Therefore, Mars was developed to place molecule records in virtual storage and retrieve them as needed. Multithreaded processing of these very large datasets was further facilitated by the molecule object core data model, which allows for processing of molecule records in parallel, leveraging the concurrent data structures provided in Java.

A powerful, scriptable API and graphical user interface, allowed for the development of secondary classification algorithms to identify beads with desired qualities (i.e. coilable, showing gyrase activity, etc.) (http://github.com/duderstadt-lab/fmt-scripts). Plots for figures were similarly made leveraging the Mars API but with ImageJ running in Jupyter notebooks written in Groovy or Python. Additional plotting was performed using Prism 8.

4.3 Spatial resolution

Several distinct factors influence the spatial resolution obtained in our experiments. The magnification, pixel dimensions, and intensity of the bead together result in a fundamental limit in spatial resolution independent of the experimental condition. This can be calculated with the following expression:

$$\sigma = \sqrt{\frac{s^2}{N} + \frac{a^2}{12N} + \frac{8\pi s^4 b^2}{a^2 N^2}} \tag{4.1}$$

where N is the number of photons, a is the pixel size, b is the standard deviation of the background, and s_x is the standard deviation of the fit of the bead.[69] For MyOne beads with a diameter of 1 µm that are nonspecifically stuck on the surface, we measured N = 50,200 photons, a = 1.57 µm, b = 107, s_x = 0.78 µm. These measurements were performed using the telecentric lens having 7x magnification and NA 0.23. The camera was set to 2x binning and collection was performed at 4 Hz. The theoretical limit of spatial resolution for these conditions is ~6 nm. However, several other factors prevent realization of this limit. The most significant of these is mechanical drift. The lens used to achieve the improvement in throughput is very large and tall requiring a custom microscope which suffers from mechanical drift over time. The standard deviation of the position of beads nonspecifically stuck on the surface after correcting for drift averaging over a 5 minute window is 21 nm. The resolution obtained when tracking length changes using mobile beads depends on the DNA length and applied force used in individual experiments (The s.d. of position for mobile beads in gyrase reactions was 81 nm for n = 29,892, at 33 Hz, for a 1 minute time window).

4.4 Force determination

The dramatic improvement in throughput achieved using FMT relies on the addition of a lateral flow force so that length changes can be observed as lateral changes in position. This removes the requirement for high numerical aperture optics needed for tracking axial position changes. In magnetic tweezers, the force can be calculated using the equipartition theorem (Equation (3.20) given by $F = k_B T l \,/\, <\delta y^2>$, where k_B is the Boltzmann constant, T is the absolute temperature, l is the length of the molecule, and $<\delta y^2>$ is mean-squared displacement of the beads along an axis orthogonal to the force axis, for FMT experiments this is perpendicular to flow (Figure 4-1 A). However, in FMT experiments only the projected length is observed and not the absolute length, l, from the equipartition theorem. Both the length and the force therefore, were solved numerically by assuming Worm-Like-Chain (WLC: Equation (3.7)) behavior[7,70] using the set of equations:

$$\langle \delta y^2 \rangle = \frac{k_B T l}{F} \tag{4.2}$$

$$\frac{FP}{k_B T} = \frac{1}{4}\left(1 - \frac{l}{l_0}\right)^{-2} - \frac{1}{4} + \frac{l}{l_0} \tag{4.3}$$

where F is the force, P is the persistence length (46 nm)[8], l_0 is the contour length of the DNA (21 kb, 6.8 μm), l is the extension length of DNA, and the remaining constants are specified above ($T = 296$ K, $k_B = 1.38 * 10^{-23}$ m^2 kg s^{-1} K^{-1}). A utility function was written in the Mars plugins to perform the numerical solving (calculateForceAndLength in the util package in the MarsMath class of mars-core). The BracketingNthOrderBrentSolver of the apache commons math3 package was used for the numerical solving. The settings used can be found in the ForceCalculator class in the util package of mars-core. Formula (4.3) is an approximation for the WLC that exhibits 5 to 7% error at mid extension. If extensive experiments will be conducted within this range an alternative formula, with additional corrections, should be used[71].

To determine the applied force for both single beads and clusters of beads (both were observed in individual experiments), force was calculated individually for each molecule. During the initial stage of each experiment the frame rate was increased from 4 Hz to 33 Hz. Force was calculated at the higher frame rate using the variance of bead motion in the direction perpendicular to flow. 33 Hz was the highest rate achievable for the full sensor of our camera with 2x binning. These measurements had to be conducted with the full sensor to capture all molecules. While considerably higher than the experimental frame rate, 33 Hz is too slow to capture the full extent of bead fluctuations that occur on shorter timescales. Fortunately, this is a well-known phenomenon and a correction factor can be calculated for motion blur due to under sampling.[70]

The force versus flowrate results presented in Figure 4-3 D were corrected for the influence of motion blur (Equation (3.22)) using the approach outlined by Wong and Halvorsen[67] using the correction factor S.

$$S = \frac{2}{\gamma} - \frac{2}{\gamma^2}(1 - e^{-\gamma}) \tag{4.4}$$

Where γ is the product of the camera integration time W and inverse trap relaxation time, α is the spring constant of the trap (equivalent to force F over length l)[38], and β is the friction factor of the particle given by the Stokes' law.

$$\gamma = \frac{W\alpha}{\beta} = \frac{FW}{l 6\pi\eta r} \tag{4.5}$$

Where r is the radius of the bead and η is the viscosity. The corrected variance is the measured variance divided by the correction factor S.

$$\langle \delta y^2 \rangle_c = \frac{\langle \delta y^2 \rangle}{S(\gamma)} \tag{4.6}$$

The correction factor S depends on force and length, which are numerically determined using equations (4.2) & (4.3). Therefore, the correction factor was incorporated into equation (4.1) in a second numerical solver class called MotionBlurForceCalculator in the util package of mars-core. This solver was used to calculate the points in Figure 4-3 D. The numerically determined correction factor ranged from 2% at lowest flowrate of 2.5 ul/min (used for all gyrase reactions) to 40% at the highest flowrate of 80 ul/min. The blur correction was only applied in Figure 4-3. The other figures present experiments conducted at the lowest flowrate of 2.5 ul/min where motion blur does not significantly influence force estimation.

The magnets were kept at a constant height above the flow cell throughout all experiments. To determine the magnetic force the fluctuations in bead position at zero flow were measured. Under these conditions the numerically determined force is 0.08 ± 0.04 pN (n = 917 molecules from one experiment). Given an estimate for the bead height above the surface, the force due to drag can be calculated using Stokes' law. However, the low magnification lens used to obtain very high throughput does not allow for direct observations of bead height above the surface. Nevertheless, the height can be estimated using a combination of experimentally determined and calculated values. The attachment site of all DNA molecules is determined using the reversal step at the beginning of all experiments. The projected length can be calculated throughout each experiment. The fluctuations in bead position perpendicular to flow were used to numerically solve for the force and extension of each DNA molecule. Using these two values the angle and height above the surface can be calculated for the bead position using the following formulas.

$$\theta = \cos^{-1}\frac{l_{xy}}{l} \quad and \quad z = l\,\sin\theta \tag{4.7}$$

Where l_{xy} is the projected length in the xy-plane, l is the end-to-end extension of the DNA and θ is the angle with the surface. All gyrase experiments were performed at a flowrate of 2.5 μl/min. Under these conditions the numerically determined force and extension length are 0.2 ± 0.1 pN and 4.4 ± 0.1 μm, respectively. The projected length is 3.8 ± 0.1 μm and we calculate a mean angle of 25° ± 2° and height above the surface (in the z direction) of 2.1 ± 0.1 μm (calculated from n = 917 molecules from one experiment). The drag force can be calculated using Stokes' law.

$$F_d = 6\,\pi\eta r v \quad where \quad v = 2\,v_{max}\frac{z}{h}\left(1-\frac{z}{h}\right) \quad and \quad v_{max} = \frac{3Q}{2wh} \tag{4.8}$$

Where F_d is the drag force for viscosity η, bead radius r and flow velocity v. For a laminar flow the flow velocity is a function of the distance above the surface as given by the central expression where h is the height of the flow cell and z is the distance of the bead above the surface. And finally, v_{max} is the highest flow velocity observed at the center of the flow lane, which can be calculated from the height h, width w, and the volumetric flow Q. The drag force can be calculated using the height above the surface from our experimental data (z = 2.1 μm). All the other parameters are known for our system to have the following values: w = 3 mm. h = 100 μm, η = 8.9*10^-4 Pa*s (for water), Q = 4.2*10^-11 m^3/s. Using these values the drag force is 0.07 pN.

The above calculation is an approximation for the primary experimental condition used for all gyrase reactions reported. The force as a function of flowrate plot reported in Figure 4-3 D was generated using a range of flowrates. Given that the magnet height was held constant throughout these experiments, the approximation above will not be accurate for the higher flowrates. The bead height above the surface was expected to decrease to as little as 100 nm at the highest flowrate of 80 μl/min. Surface effects may be observed under these conditions. By lowering the magnet closer to the flow cell at higher flowrates a constant bead height above the surface could be maintained. In the current study this was not necessary because all gyrase experiments were conducted at very low flowrate and low force where the approximation above holds.

5 Investigating DNA gyrase dynamics using FMT

To demonstrate the multiplexing capability of flow magnetic tweezers, the supercoiling dynamics and drug-induced DNA double-strand (dsDNA) break intermediates of gyrase were characterized. Gyrase is a type-II topoisomerase that plays an essential role in the maintenance of bacterial chromosomes by using the energy from ATP to conduct positive supercoil relaxation and negative supercoil introduction[16]. Using these activities, gyrase supports a wide range of essential cellular processes including transcription and DNA replication[72]. These vital functions of gyrase make it an ideal antibiotic target[16]. Several major classes of potent inhibitors target gyrase including quinolones like ciprofloxacin[73], which is commonly used to treat a wide range of bacterial infections. Structural and biochemical studies have demonstrated that ciprofloxacin kills gyrase function by stabilizing a DNA break intermediate, which prevents completion of the reaction cycle[16,74]. However, when and how this stalled intermediate is converted into an exposed DNA break that triggers a cellular response is not well understood. Using the improved throughput of FMT, links between break formation and topology-dependent enzymatic activity were established. These experiments reveal a remarkable stability in gyrase-drug complexes and resistance to extreme torques.

5.1 Massive parallel imaging of topological transformations by gyrase

Having established accurate force and topology control, FMT was used to investigate the kinetics of topological rearrangements by the topoisomerase gyrase. Prior to introduction of gyrase, individual tethers were classified using a series of changes in flow velocity and magnet rotations (Figure 5-1 A, Supplementary movie 2). First, flow was reversed to identify mobile beads and the attachment site of each tether. Second, negative and positive coiling steps were conducted at high force to identify coilable molecules and distinguish them from multiply tethered beads. Third, after force determination at constant flow and magnet position, negative and positive coiling was performed a second time to determine the rate of compaction versus turns at the reaction flow rate. Finally, the tethers were left positively coiled ($\sigma > 0$) and gyrase was introduced. Upon arrival of gyrase, tethers rapidly extended and, following a pause, compacted at a slower rate. To further investigate the force and topology dependence of gyrase activity, the classification steps performed with FMT prior to gyrase arrival were considered. Molecule-by-molecule force determination revealed differences in the applied force on individual molecules within single experiments. This heterogeneity in the distribution of forces is attributed to the differences in the size and magnetic content of individual microspheres. Additionally, depending on buffer conditions and sample preparation, bead clusters were observed, resulting in increases in force proportional to cluster size. Using current force spectroscopy techniques these subpopulations may not be statistically significant, but the massive multiplexing of FMT allows for their quantification in studies of complex activity versus force relationships within single experiments.

Using this approach, the force dependence of gyrase activity in just two experiments performed with different flow velocities was determined (Figure 5-1 B). The peak velocity for positive relaxation was 1.26 ± 0.07 cycles/s (median ± s. e. median) at 0.2 pN after which the velocity decreases to a plateau of ~ 0.85 cycles/s was observed. Introduction of negative supercoils is more sensitive to force having a peak velocity at 0.65 ± 0.05 cycles/s (median ± s. e. median) at ~ 0.2 pN and loss of activity above ~ 0.5 pN. The force-velocity relationship observed here qualitatively agrees with observations made using magnetic tweezers.[58] The peak velocity also quantitatively agrees with past reports.[58,59] The force and topology dependence of gyrase observed here can be interpreted as a combination of distinct operational modes previously reported. Below ~ 0.5 pN is α mode, where gyrase resolves positive supercoils by strand passage of a proximal segment and introduces negative supercoils. Above ~ 0.5 pN gyrase is in χ mode for which only positive supercoils are resolved by strand-passage of a distal segment.[58,59]

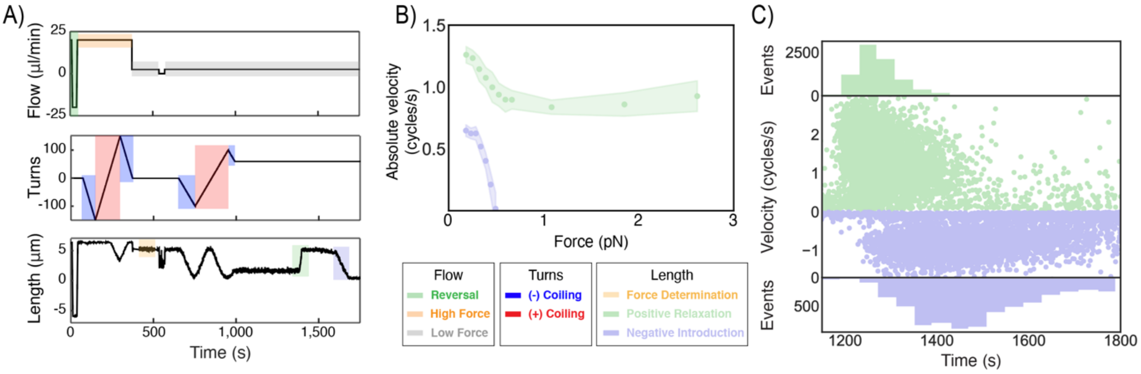

Figure 5-1 Massive parallel imaging of DNA supercoiling by gyrase. A) Changes in flow and magnet rotations used for molecule classification. Mobility is checked using flow reversal (green). Negative and positive coiling are conducted to select singly-tethered beads (blue and red). Force is determined at higher frame rate (33Hz, orange). Finally, rapid lengthening, pausing, and shortening are observed as gyrase relaxes positive supercoils (green) and introduces negative supercoils (blue). B) Velocity (cycles/s) versus force (pN) dependence of gyrase. Median rates of positive supercoil relaxation (green) and negative supercoil introduction (blue) (n = 680 molecules from two independent experiments). Shaded regions represent the s. e. median. C) Gyrase activity burst velocities (cycles/s) versus start times (s) for individual molecules observed in a single experiment. Bursts of positive relaxation (green, n = 8,426 bursts from one experiment) and negative introduction (blue, n = 3,302 bursts from one experiment). Molecules at higher forces did not have negative supercoil introduction bursts, but were nonetheless plotted and show up as a broad scatter near zero. Of the 53,831 microspheres tracked, 12,172 passed the pipeline outlined and were evaluated for activity bursts.

The multiplexing capability of FMT was benchmarked by analyzing a gyrase experiment in which 53,831 molecules were tracked. Among those, the feature classification pipeline of Mars (Figure 5-3) identified 12,832 coilable molecules and a final set of 8,874 accepted molecules, which were also reversible, singly tethered and remained so throughout the experiment. Mars reported 7,969 bursts of positive relaxation and 6,183 bursts of negative introduction. The massive throughput achieved is visible in the velocity versus burst time scatter plot in Figure 5-1 C. FMT provides more than an order of magnitude higher throughput than existing force spectroscopy approaches (Table 4-1).

5.2 Molecule classification

A rigorous set of criteria were used to evaluate and further classify individual molecules generated using the Mars Peak Tracker. First, the mobility of each bead was checked using the mean squared displacement as well as flow reversal steps at the beginning and end of each experiment. The center point between the two extreme positions during flow reversal was taken as the attachment site to determine the projected length. Next, molecules were checked for coilability (to ensure they were not nicked) by performing a series of clockwise and counterclockwise rotations of the magnets. The standard coiling series was 150 clockwise turns and 150 counterclockwise turns, followed by 150 counterclockwise turns and 150 clockwise turns (Figure 5-2 A). To determine if beads were single or multiply tethered, the coiling steps were conducted at high force. For this condition single tethers only showed compaction for positive supercoiling, whereas multiply-tethered beads showed compaction for both coiling steps (Figure 5-2 B). Multiply-tethered molecules were then removed based on the slope in the negative coiling region. For gyrase experiments the final uncoiling step was stopped after 40 turns leaving the DNA positively supercoiled in preparation for gyrase arrival. An additional high frame rate (33 Hz) region was added for molecule-by-molecule force determination (using the approach outlined in Force determination). For gyrase experiments the rate of length change observed during magnet rotations conducted at the experimental flowrate was used to calculate the number of cycles/s.

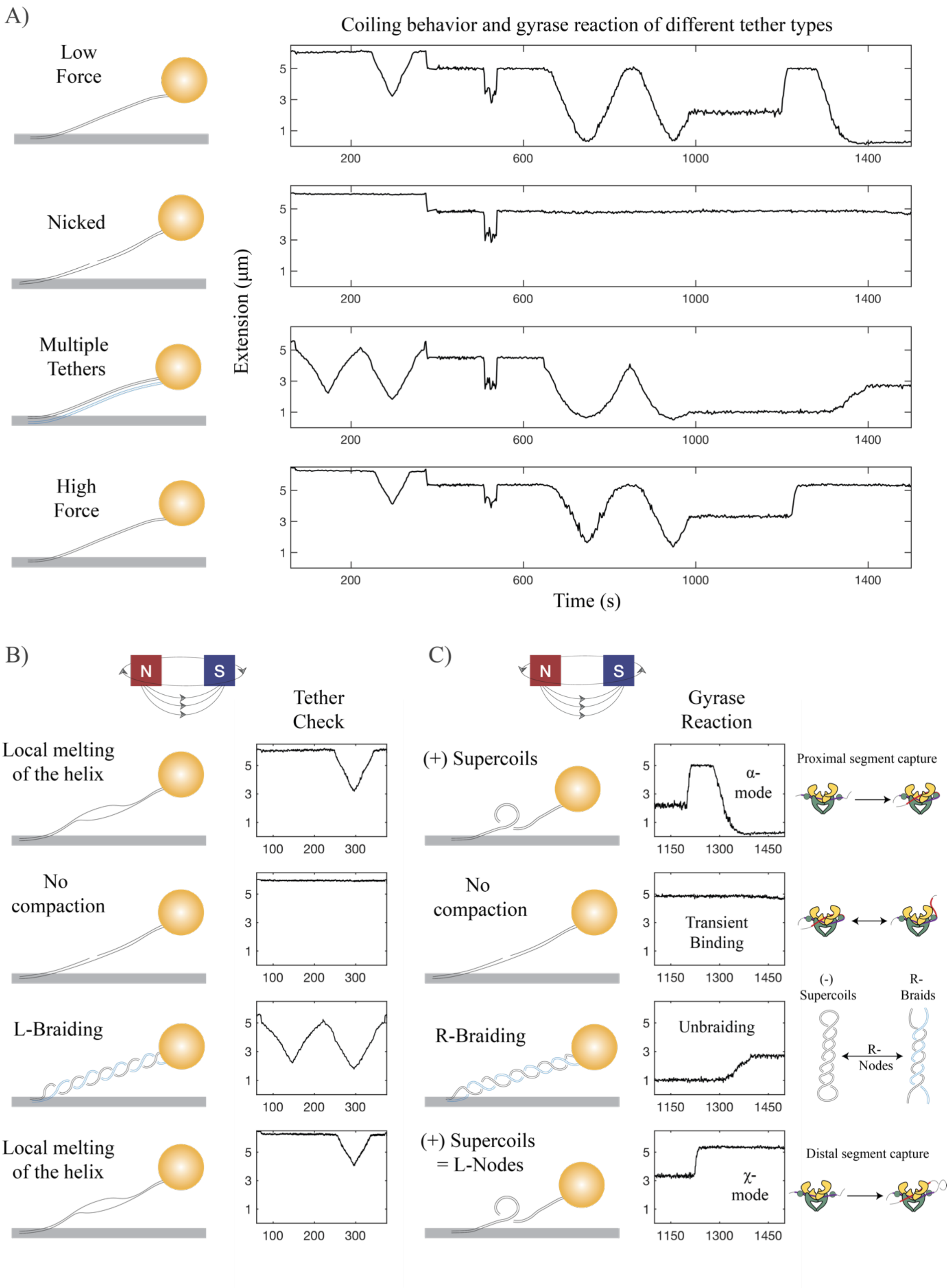

Figure 5-2 Molecule classification. A) Example traces of different tether types where distinct coiling and enzymatic behavior can be seen. B) Tether check for coilable, nicked and multiply-tethered molecule where compaction for only positive coiling, no compaction and braiding compaction is seen respectively. C) Gyrase behaves distinctly for (+) supercoiled molecule at low (α-mode) and high (χ-mode) forces. Nicked

molecules exhibit minimal compaction where gyrase molecule trasiently bind to the topologically relaxed molecule. Lastly R-braiding is resolved by gyrase where it displays poor decatenase activity.

Bursts of gyrase activity within the subset of coilable molecules were classified using the overall length change from before gyrase arrival and after all supercoiling activity. For α reactions, where the DNA is negatively supercoiled after relaxation, this length difference is negative. For χ reactions, where the DNA is only relaxed and high force prevents introduction of negative supercoiling, this length difference is positive (Figure 5-2 C). The locations of gyrase activity within these selected molecules were identified using a sliding window approach. A window of 12.5 s was used in the region prior to max length to identify the region of positive supercoil relaxation (searching for the highest slope). A window of 25 s was used to identify the region of negative supercoiling (searching for the lowest slope). The difference in window size was due to differences in the duration of the distinct activities. The maximum slopes detected are represented as circles in the scatter plot displayed in Figure 5-1 C.

In all cases, the Mars API was used to develop scripts for automated secondary classification either using the scripting editor of Fiji or Jupyter notebooks. Plots were created in Jupyter notebooks using matplotlib, Matlab and Prism 8.

5.2.1 Feature classification using Molecule Archive Suite (Mars)

To efficiently process the large datasets generated in FMT experiments, Molecule Archive Suite (Mars) – a high-performance collection of single-molecule analysis plugins for Fiji[68,75,76] written in Java was developed (source code and installation instructions available at https://github.com/duderstadt-lab). By combining this classification pipeline with a standard series of force and torque manipulations, we quantify a broad spectrum of gyrase behaviors. These include positive supercoil relaxation, negative supercoil introduction, unbraiding, and very rare DNA breaks. Studies of gyrase dynamics show the potential of FMT as a platform to rapidly characterize small subpopulations that exhibit rare enzymatic activities with single molecule precision. Multiplex FMT can be readily adapted to studies of a broad range of complex, multistep enzymatic pathways in which throughput presents a significant challenge that prevents the discovery and characterization of novel intermediates.

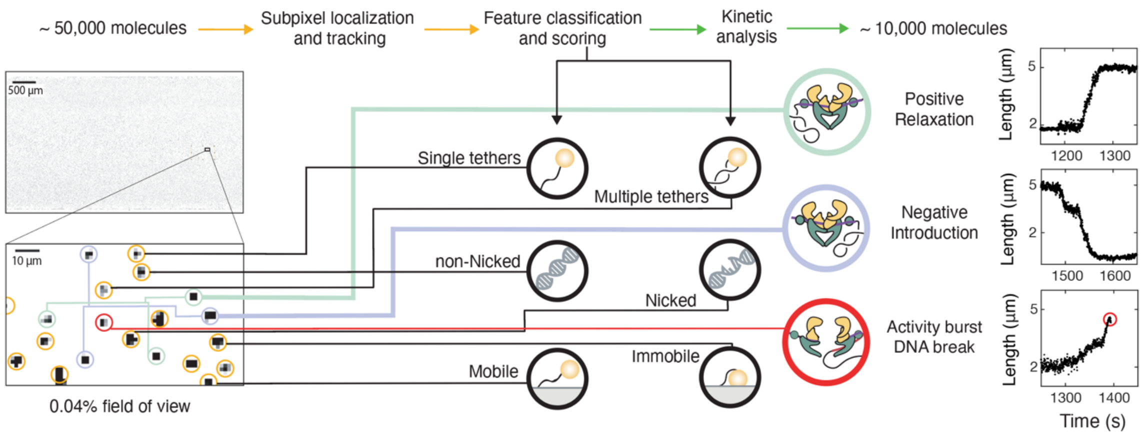

Figure 5-3 Automated feature classification pipeline to convert raw videos to annotated Molecule Archives containing scores for standard features and tags for gyrase behaviors. Images and example traces were selected from three independent experiments.

Using Mars, all beads were located and tracked with subpixel accuracy. Secondary classification algorithms based in part on kinetic change point analysis[66] (Figure 5-3) helped allocated different tags to single molecules. The tracking results from FMT experiments typically do not fit in physical memory. Therefore, Mars relies on a new core data model based on collections of molecule objects each with a universally unique identifier (UUID) that are retrieved from the hard drive on demand. The architecture allows for seamless virtual storage, merging, and multithreaded processing of very large datasets.

5.2.2 Gyrase behavior under different buffer conditions

As expected for topoisomerase II activity, the given behavior was not observed in the absence of ATP or on nicked, non-coilable molecules (Figure 5-4). These observations are consistent with previous reports showing that gyrase resolves positive supercoils and has the unique ability to introduce negative supercoils on relaxed DNA molecules.[58] Therefore, the extension was interpreted as a resolution of positive supercoils and the compaction as an introduction of negative supercoils. Since each enzymatic cycle of gyrase is known to change the net Linking Number (Lk) of DNA by -2 turns[77], we conclude that each burst of activity represents multiple enzymatic cycles.

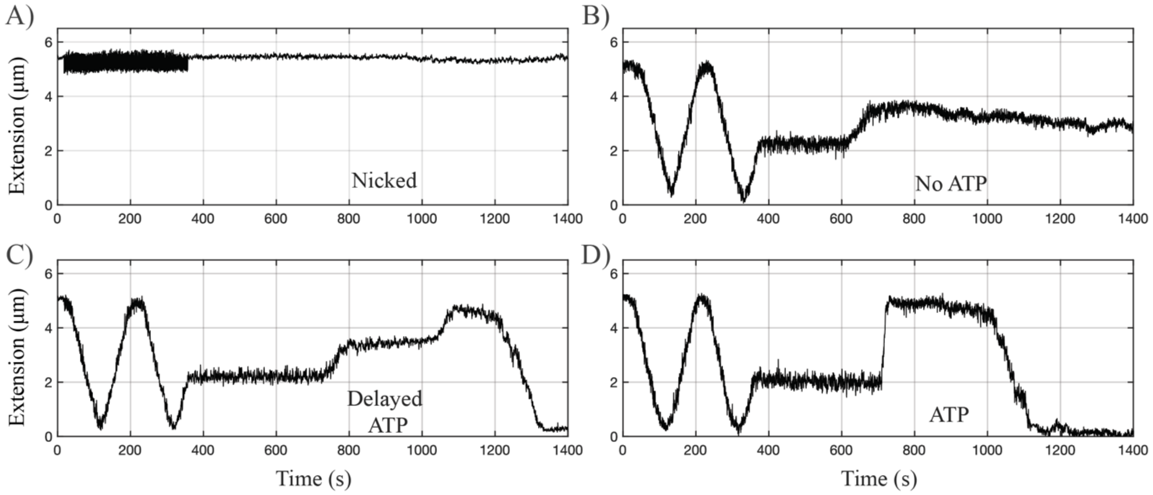

Figure 5-4 Gyrase activity for different buffer conditions. A test for coilability was conducted at the beginning as follows: DNA was negatively supercoiled with 100 clockwise turns, uncoiled with 100 counterclockwise turns, positively supercoiled by 100 counterclockwise turns. After the coilability test, 40 clockwise turns were conducted leaving the DNA positively supercoiled prior to gyrase arrival. A) Nicked molecules display no length changes due to magnetic rotation or introduction of gyrase. Distinct behaviors are observed for non-nicked molecules depending on the buffer conditions: B) In the absence ATP, DNA length increases upon gyrase binding. C) If ATP is supplied in the buffer with gyrase, DNA length increases in two steps. First, due to binding as displayed in B). Second, due to ATP-dependent relaxation of positive supercoils. The second step is followed by a pause and a decrease in length as gyrase negatively supercoils the DNA. D) If the flow cell is prewashed with ATP, the initial length increase is absent and only ATP-dependent relaxation of positive supercoils is observed. This is followed by a pause and then the length decreases as gyrase negatively supercoils the DNA. The rate of positive supercoil relaxation is approximately half in the absence of an ATP prewash. All experiments reported were conducted with an ATP prewash prior to introduction of gyrase into the flow cell.

5.3 Gyrase inhibition and DNA break formation induced by ciprofloxacin

The improvement in throughput offered by FMT allows for rapid characterization of numerous subpopulations from individual experiments and direct observations of rare, yet critically important, events in the life cycle of the cell. To demonstrate the detection power of FMT, a series of experiments were performed to directly visualize gyrase dynamics in the presence of the potent inhibitor ciprofloxacin. During each cycle of activity, gyrase makes a transient double-strand break in one DNA strand, passes a second strand through, and then reseals the break[78]. The transient double-strand break formed by gyrase during strand passage is exploited by ciprofloxacin, which prevents resealing of the break upon binding (Figure 5-5 A). The drug is believed to kill cells by at least two pathways. In one pathway, inhibition of relaxation of positive supercoils and introduction of negative supercoils is believed to shutdown DNA replication and transcription[16]. In the other pathway, the transient DNA breaks stabilized by ciprofloxacin are thought to be converted into permanent DNA breaks that cause severe genome damage[79]. The mechanism of the former pathway is clear, but how and when gyrase-drug complexes disassemble to become *bona fide* DNA breaks and reveal themselves to the cell is not well understood. As a consequence, the sequence of events during the cellular response to many important antibiotics remains unclear.

Gyrase reactions were conducted in the presence of increasing concentrations of ciprofloxacin to characterize inhibition and detect DNA breaks. Importantly, the sequence of transformations outlined in Figure 5-1 A was conducted for all experiments so molecules could be filtered using the feature classification pipeline outlined in Figure 5-3. This filtering step ensures the gyrase dynamics reported are only from properly formed, non-nicked DNA tethers. As previously outlined, gyrase was introduced to positively supercoiled DNA molecules and the rates from bursts of positive supercoil relaxation and negative supercoil introduction were determined using sliding windows. The burst analysis revealed a dose-dependent reduction in gyrase activity (Figure 5-5 B, C, D) with an IC50 of 0.94 μM (0.2 to 4.1; 95% CI) for positive supercoil relaxation and 5.3 μM (2.6 to 12.1; 95% CI) for negative supercoil introduction. These values are consistent with past estimates placing the IC50 around 0.5 μM using gel-based cleavage assays[80]. The number of positive relaxation (np) and negative introduction (nn) bursts used to generate Figure 5-5 B, C were as follows: no drug (np = 1662, nn = 1067), 78 nM (np = 1492, nn = 1014), 156 nM (np = 1503, nn = 923), 312 nM (np = 1761, nn = 942), 1,250 nM (np = 3202, nn = 2050), 2,500 nM (np = 1072, nn = 501), 5 μM (np = 2647, nn = 1340), 20 μM (np = 3204, nn = 2609), 50 μM (n = 506). Each represents molecules observed in single experiments. Figure 5-5 D shows representative traces of gyrase activity, treadmilling and recovery at similar conditions with incrementing ciprofloxacin concentration. Enzymatic activity of gyrase is hampered while resolve (+) supercoils and while introducing (-) supercoils. This is also apparent during treadmilling as gyrase can barely resolve the excess torsion at higher drug concentrations as well the poor recovery of any gyrase activity once the treadmilling is paused.

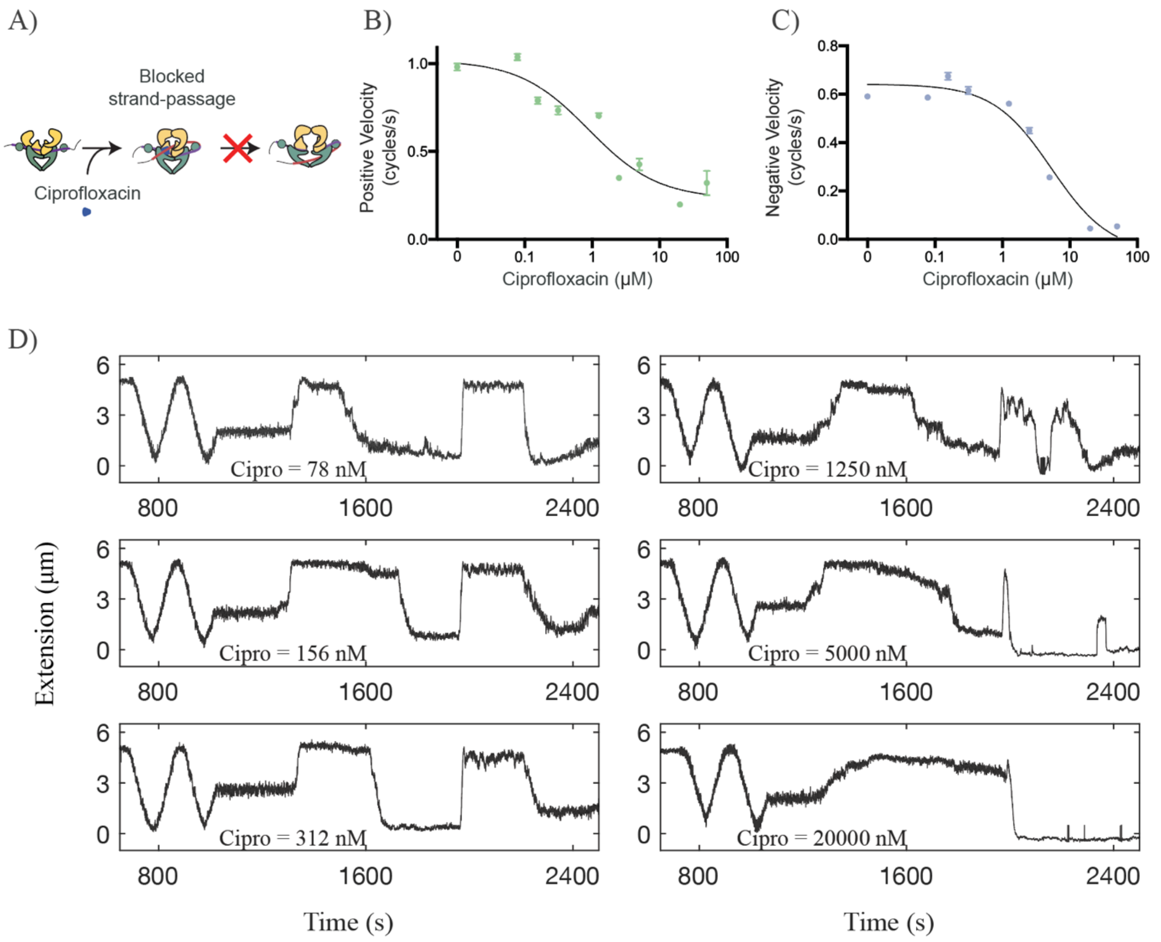

Figure 5-5 Gyrase activity inhibition due to ciprofloxacin. A) Enzymatic cycle of gyrase. Gyrase binds a gate segment, makes a transient DNA break, and passes a transfer segment through. Ciprofloxacin prevents resealing of the break. B) The velocity of positive supercoil relaxation as a function of ciprofloxacin concentration. The IC50 from the inhibitor versus response equation (Y=Bottom + (Top-Bottom)/(1+(X/IC50))) was 0.94 μM (0.2 to 4.1; 95% CI). C) The velocity of negative supercoil relaxation as a function of ciprofloxacin concentration. The IC50 from the inhibitor versus response equation (Y=Bottom + (Top-Bottom)/(1+(X/IC50))) was 5.3 μM (2.6 to 12.1; 95% CI). Error bars represent the s. e. median. D) Representative molecules for different ciprofloxacin concentrations. All experiments were performed under similar conditions with the exception of drug concentrations. Following the reversal to check for mobility, beads were checked for single tethering to the surface. Once the DNA was positively supercoiled, gyrase uncoils the excess positive coils and introduces negative coiling. Following the enzymatic activity, positive torque was applied using the external magnet @480 rpm for 4 minutes. Recovery of gyrase activity was then observed. It was observed that the velocity of gyrase activity was diminished with increasing drug concentration. At lower drug concentration, gyrase can still resolve the rapid positive coils introduced by the external magnet. As the drug concentration increases, gyrase barely introduces negative coils or resolves the positive coils respectively.

Given that ciprofloxacin stabilizes a transient DNA break within gyrase, we expected to see an increase in DNA breaks as a function of drug concentration. However, surprisingly, the frequency of DNA breaks did not increase even at drug concentrations of 20 μM and above with severely reduced activity. Nonetheless, rigorous classification of filtered molecules did reveal very rare DNA break events (Figure 5-3 & Figure 5-6). In total 26,063 molecules passed all filters in 10 experiments conducted at a range of ciprofloxacin concentrations and 26 DNA breaks were observed in the presence of gyrase. The breaks were evenly distributed among the cipro concentrations. The possibility that these breaks arise due to nuclease contamination in the gyrase protein stock cannot be entirely excluded. However, DNA breaks were three times more frequent during activity bursts than at random locations during the period of gyrase incubation (Figure 5-6). Frequencies were compared by considering the number of burst windows during the observation period. DNA breaks occurred in only 1 in 1,000 molecules and were only detectable due to the massive throughput improvement of FMT. Example traces of breaks during bursts are also shown for both (+) relaxation and (-) introduction.

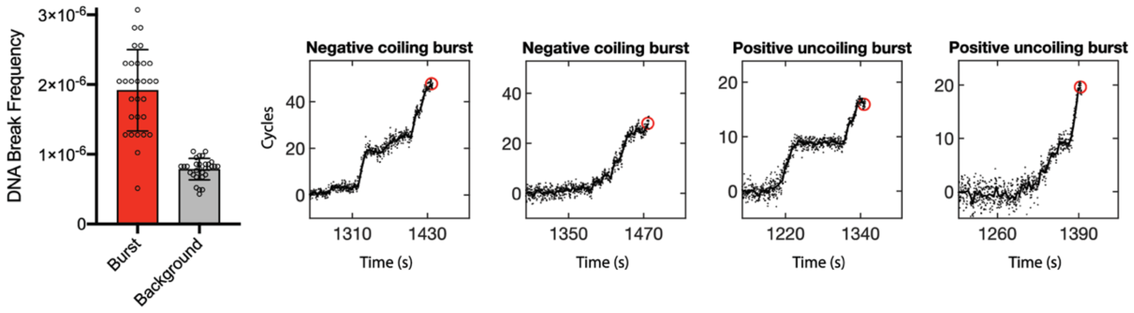

Figure 5-6 Frequency of DNA breaks that occur during bursts of gyrase activity (red) compared to background (gray) normalized by the mean burst length (n = 26,063 molecules from 10 independent experiments). In total 26 breaks were observed with 8 occurring during bursts (example traces shown). Error bars represent s.d. determined by 30 cycles of bootstrapping. Example traces of DNA double strand breaks during positive uncoiling and negative coiling bursts.

5.3.1 Visualization of 100 million reaction cycles in parallel

To further probe the enzymatic activity of gyrase and surprising stability of gyrase-drug complexes, a treadmilling assay was developed to visualize large numbers of reaction cycles in individual experiments. In the treadmilling assay (Figure 5-7 A), the magnet is rotated continuously after completion of the standard transformation series shown in Figure 5-1 A.

Three consecutive 30 minute periods, with increasing magnet rotation rates, revealed a robust ability of gyrase to continuously resolve positive supercoils as they were introduced (Figure 5-7 B, C). At the lowest rate of 2 rotation per second or 1 cycle per second, gyrase not only resolved the positive supercoils but introduced negative supercoils in bursts (blue trace, Figure 5-7 C). At higher rotation rates gyrase was only able to remove positive supercoils as they were introduced. Formation of positive supercoils at the highest rate of 8 rotations per second or 4 cycles per second, triggered the recruitment of additional gyrase molecules similar to the accumulation of gyrase visualized ahead of DNA replication[10]. On average 7,801 molecules passed filtering in each of three treadmilling experiments performed and 98 ± 11 million gyrase reaction cycles were visualized at the single-molecule level during each three-hour experiment. Using FMT, single-molecule imaging of billions of reaction cycles is easily within reach if experiments are conducted for longer than three hours with high rotation rates.

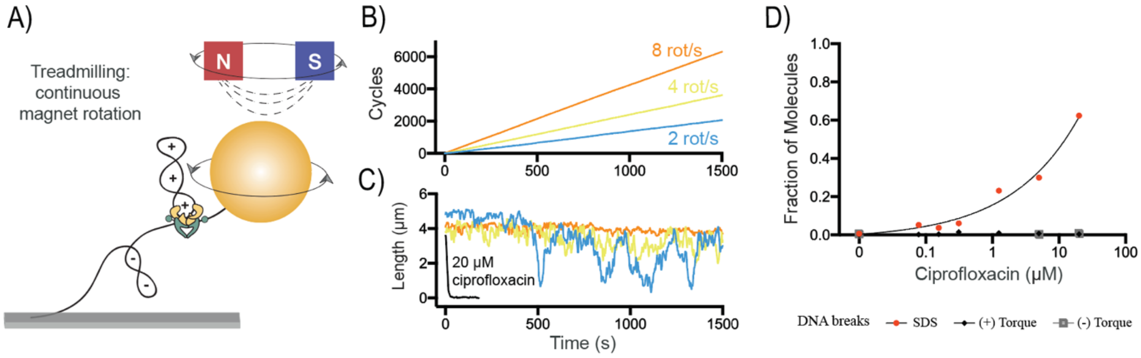

Figure 5-7 A) Treadmilling assay developed to observe continuous gyrase activity for long periods. The magnet is continuously rotated to introduce positive supercoils. Gyrase continuously resolves the positive supercoils as they form. B) Number of gyrase reaction cycles performed as a function of time from a single molecule for different rotation speeds. C) DNA length changes during the treadmilling assay. Loss of activity and rapid compaction in the presence of ciprofloxacin is shown in black for 8 rotations per second. D) Fraction of molecules with DNA breaks as a function of ciprofloxacin concentration, positive and negative torque, and SDS treatment.

The treadmilling assay provided the opportunity to probe the stability of gyrase-drug complexes in response to torque. Treadmilling experiments were conducted in the presence of increasing concentrations of ciprofloxacin to characterize inhibition of treadmilling activity and detect whether DNA breaks form as a result of positive or negative torque. At high drug concentration gyrase was inhibited and DNA rapidly compacted in response to magnet rotations (Figure 5-7 C). Remarkably, no increase in DNA break frequency was observed as a function of drug for high levels of positive or negative torque (up to $\sigma = 0.35$). To confirm that gyrase-drug complexes housing transient DNA breaks were in fact formed under our experimental conditions, an extreme 0.1% sodium dodecyl sulfate (SDS) wash step was introduced after completion of the torque step. The detergent wash revealed massive, dose-dependent DNA breaks as gyrase-drug complexes unfolded confirming their formation in the torque experiments (Figure 5-7 D). Importantly, a control in the absence of gyrase and drug revealed no tether loss during SDS washing. These observations demonstrate the extreme stability of gyrase-drug complexes over a wide range of experimental conditions.

6 Characterizing type IIA topoisomerases

The pipeline established for gyrase could be used to investigate other type II topoisomerases as well. Eukaryotic topoisomerases are homodimers as compared to DNA gyrase and topo IV which are heterotetramers. Similar to topo IV in bacteria, they are known to modulate topology by resolving both positive and negative supercoiling as well as catenates in eukaryotes[16,81,82]. Here the topoisomerase II from *Saccharomyces cerevisiae* (scTop2), the two isoforms of human topoisomerase IIα and IIβ (hTop2α and hTop2β respectively) and point-mutant of hTop2β where Valine (111) is replaced with Isoleucine were investigated.

scTop2 is the only known topo II in yeast. It untangles knots in DNA, decatenates linked chromosomes and help segregate them during mitosis. It is an essential enzyme and can even replace topoisomerase 1 function in yeast cells[83,84]. The crystal structure of scTop2-DNA-nucleotide complex shown by Schmidt *et al.*[85] is the only known structure of a full-length eukaryotic Top2 (the cryo-EM structure of a complete gyrase-DNA-antibiotic was also shown by Vanden Broeck *et al.*[86]). As the sequences among eukaryotic topo II are well-conserved, the structural similarity is used to create homology models of other topo II from higher eukaryotes. hTop2α is essential for chromosome segregation and expressed in proliferating cells while hTop2β is explicitly present in non-dividing and terminally differentiated cells[87]. These isoforms share almost 77% sequence homology and same mechanism of action[15,16,87]. The Carboxy-terminal domain (CTD) however differs, imparting a preference for hTop2α to resolve positive supercoils while hTop2β does not display any chirality dependence[16,88]. The point-mutation V111I (βVtoI) resides in the ATP-binding pocket and is close to the ATP hydrolysis site. This mutation is aimed at disrupting ATP hydrolysis *via* steric hinderance and indirectly influences DNA double-strand cleavage and religation by inhibition of energy transduction. Another mutation where Arginine (757) is replaced with Tryptophan (βRtoW) finds itself near the dimeric interface of DNA and cleavage domains. Replacement with tryptophan can disrupt the dimer interface while directly influencing dimer formation hence causing breaks.

Positive supercoil relaxation of these eukaryotic topoisomerases was characterized at the same conditions as gyrase while using following buffer:

10 mM Tris-HCl pH 8.0, 50 mM NaCl, 50 mM KCl, 3 mM MgCl2, 0.1 mM EDTA, 1 mM DTT, 1 mM ATP, 0.1 % Tween and 0.1 mg/mL BSA with 0.2 nM of topo II unless specified.

This buffer was adapted from a study by Le *et al.*[89] where the (+) plectoneme uncoiling rates of scTop2 were observed under similar conditions with the exception of enzyme concentration (1 pM). The rate observed in their study 1.8 ± 0.6 turns/s (or 3.6 ± 1.2 cycles/s at 0.5 pN) was comparable to rates of other eukaryotic topo II studies such as *Drosophila melanogaster* topo II by Strick *et al.*[90] (3.2 ± 0.2 cycles/s at 0.3 pN) and hTop2α by Seol *et al.*[88] (3.2 ± 0.6 cycles/s at twist density +0.6%, force not specified). Here, diverse topoisomerases II were introduced at a wide distribution of forces as shown in the velocity box plots in Figure 6-1. Gyrase and scTop2 display similar velocities with 1.4 ± 0.5 cycles/s and 1.4 ± 0.5 cycles/s respectively. This result contradicts the findings from Le *et al.*[89] as the rate of scTop2 positive uncoiling is vastly different as compared to other eukaryotic topoisomerases. Possible explanations could be a difference in forces or temperatures at which the experiments were performed. The rate of hTop2α however (2.7 ± 0.8 cycles/s), is comparable to the rates by Seol *et al.*[88]. As suggested in this study, the velocity distribution for hTop2α were broader than expected due to heterogeneous enzymatic activity; thus, twist density as a metric was used. This heterogeneity is apparent in the boxplot for hTop2α here as well. The rate of hTop2β (2 ± 0.6 cycles/s) and its comparison to the rate of hTop2α could indicate the chirality discrimination and preference for positive supercoils by the α isoform. The rate of positive uncoiling for the V111I mutant of the β isoform, where the ATPase activity of the enzyme is hampered, the rate as compared to WT hTop2β is almost halved (1.2 ± 0.5 cycles/s). This and the R757W mutant (not shown here) are aimed at studying breaks induced by topoisomerases where additional experiments are needed to investigate break frequencies by topo II. The general trend for all the topoisomerases displays a decreasing rate of positive coil relaxation as the force increases (Further experiments at higher flow rates can convey the trend better as seen from the force ranges in the studies by Strick *et al.* and or twist density by Seol *et al.*).

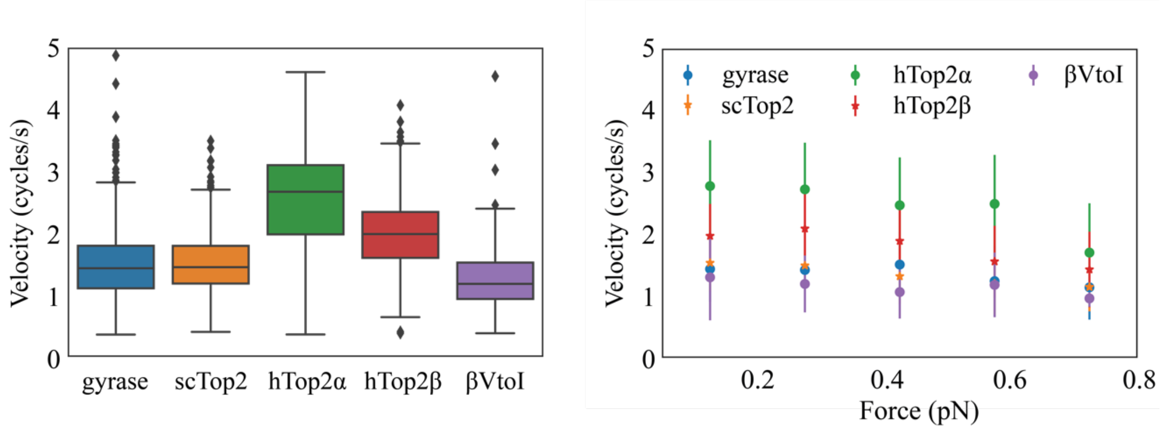

Figure 6-1 Positive supercoil relaxation velocities of diverse topoisomerases as well as the force-dependence of these rates from single-experiments. Gyrase and scTop2 rates are similar which contradicts previous study from Le *et al.* where scTop2 has comparable rates to other eukaryotic topo IIs. Greater heterogeneity in the rate of hTop2α in comparison to other topos is seen through a wider distribution along the velocity axis. Seol *et al.* previously reported this along with a comparable (+) uncoiling rate for the α isoform. Rate of hTop2β as the other isoform in higher eukaryotes is slightly lesser than the α isoform. This could point towards its chirality-independence; or rather the higher-affinity of hTop2α for (+) supercoiled DNA. For the βVtoI mutant, the rate is almost halved as compared to the WT- hTop2β. It could point towards the poor ATPase activity of this mutant where ATP-dependent DNA cleavage and religation is affected. Regarding the force-dependence of (+) uncoiling, the trend points towards a decrease in the uncoiling rate with increasing tension. A wider range of forces however, is needed to fully discern the trend.

The diversity of topoisomerases among organisms is staggering[78,81]. The physiological roles of some enzymes among distinct species also diverges. FMT provides an ideal platform to quickly characterize and screen various topoisomerases. Using the methodology and analysis pipeline, one can devise a juxtaposition plot similar to Figure 6-2. This qualitative and quantitative comparison can convey temporal and metabolic information at a glance. Normalized graphs for velocity and time reveal heterogeneity in and among diverse topo IIs. This can provide some clues as to why various type IIA topos differentially specialize for topology simplification. Expanded, this method can be use characterize innumerable enzymes and complexes involved in nucleic acid transactions.

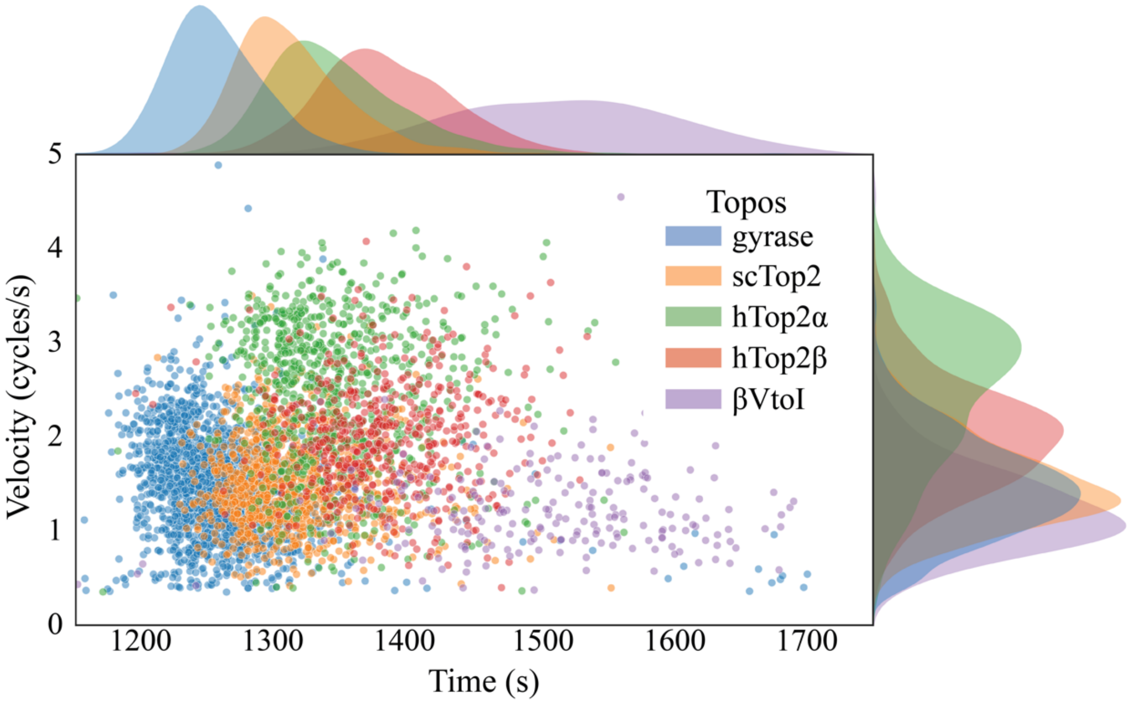

Figure 6-2 Juxtaposition plot for diverse topoisomerases. Normalized histograms for velocity and time reveal a degree of heterogeneity in and among different types of topo IIs. Overlap of graphs convey similar rates. A wider histogram such as one for hTop2α points towards heterogeneous rates of uncoiling. A comparison of WT- hTop2β and βVtoI along the time axis where the flattening of βVtoI plot reveal consequences of a point-mutation on ATPase activity of the enzyme.

7 Investigating topological stress during replication

In order to study effects of DNA topology on an active *E. coli* replication complex (Figure 3-4, Figure 3-5), DNA construct shown in Figure 3-13 B can be modified to topologically constrain the substrate.

7.1 Alternative DNA constructs

DNA substates in previous replication studies were designed such that the leading strand was primed[44,46,91]. Contraction of ssDNA of the lagging strand conveyed the rate of replication (Figure 7-1 A, DNA flow stretching) where the primed leading strand of this substrate can be tethered to the surface to constrain torsional stress in the parental strand (Figure 7-1 B). This strand was designed and tested with phi29 DNA polymerase where a 3-6-fold increase in rate of bead contraction was measured in a topologically constrained substrate, pointing towards plectoneme formation due to replication. The substrate however didn't yield a lot of constrained molecule, potentially due to the lack of attachment sites as shown in Figure 7-1 B. Possible substrates to overcome this problem involve introducing multiple biotin attachment moieties in the primed substrate (Figure 7-1 C). A better solution however, is to introduce *E. coli* replication initiation locus *OriC* in the plasmid backbone instead of priming the leading strand (Figure 7-1 D). In this substrate, henceforth referred to as the OriC substrate, the origin site contains DnaA boxes and AT-rich DNA unwinding element (DUE).

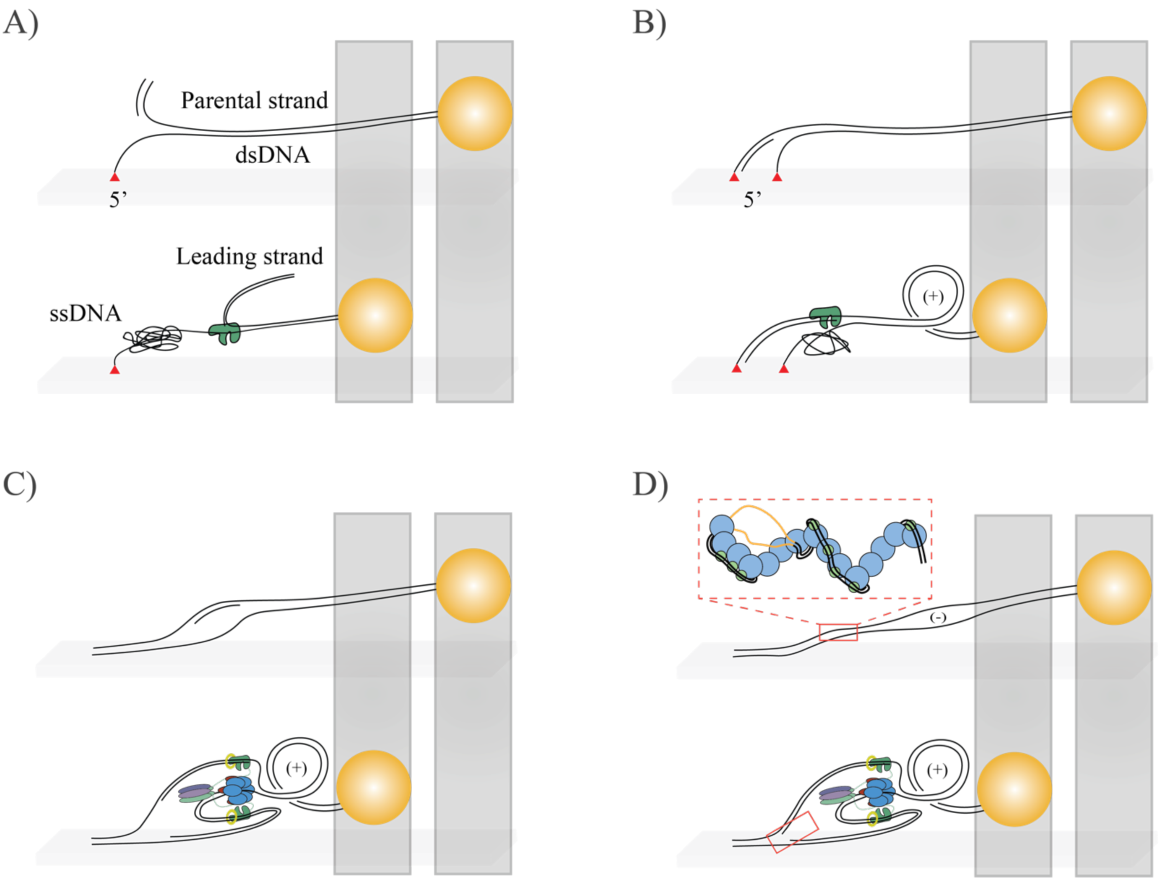

Figure 7-1 Different DNA constructs to study replication. A) Leading strand is primed and lagging strand is tethered to the surface. As a polymerase synthesizes the parental strand, bead displaces due to compaction of ssDNA. B) Leading strand is primed and tethered to the surface along with the lagging strand, this construct can convey information about the effect torsional stress has, on replisome. However, it lacks sufficient attachment moieties. C) This construct is an extension of the construct shown in B) and has multiple attachment moieties. D) This construct is a normal dsDNA with no priming on the leading strand. It contains the replication initiation locus of *E. coli* called *OriC*. The introduction of this construct in FMT and DnaA protein will help unwind the DUE and facilitate loading of the Replisome.

7.2 Initiating replication on the OriC substrate

Once a field of these DNAs is established, the enzymes DnaA, DnaBC, DnaG, DNA pol III $(\alpha\varepsilon\theta)$, β-clamp, clamp loader complex $(\tau_3\delta\delta'\psi\chi)$ and single-strand binding proteins (SSB) are introduced in the flow cell. The DNA boxes in the *OriC* contain 9 bps consensus sequence 5' – TTATNCACA with high affinity for DnaA which melts the helix and facilitates the loading of DnaB$_6$-DnaC$_6$ helicase-loader complex (Figure 7-2 A) and subsequently rest of the replisome[14] (Figure 7-2 B).

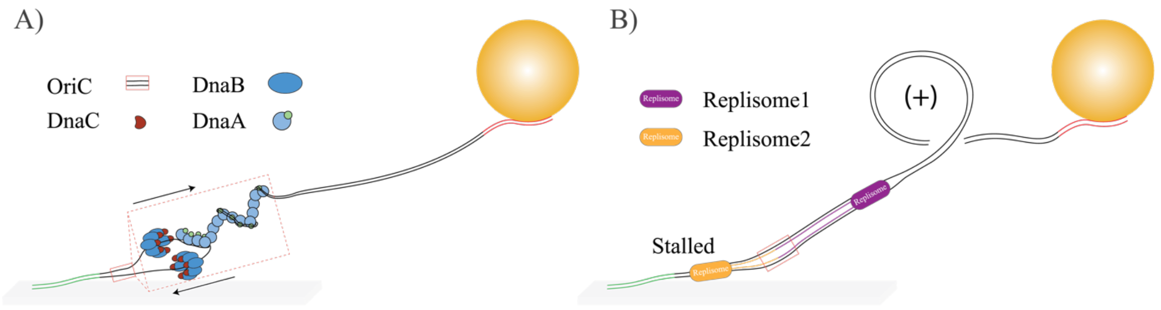

Figure 7-2 Initiation of Replication on the OriC substrate. A) DnaA binds to the DNA boxes and unwinds the DUE hence facilitating loading of the helicase loader complex DnaBC in a bidirectional fashion. B) Once rest of the replisome components are loaded, Replisome 1 continues synthesis and accumulation of torsional stress ahead of the fork causes bead to recede, shedding light on the mode of replication as discussed in Figure 3-4 B.

While Replisome 2 does not replicate for the lack of parental substrate, Replisome 1 continues replicating and hence introducing torsional stress in the topologically constrained substrate. This conveys information on how the Replisome copes with the topological problems it encounters during rapid synthesis (Figure 3-4 B). Furthermore, addition of topoisomerases topo IV and DNA gyrase at different concentrations can relieve the topological constructs such as precatenates and positive supercoils. In case these two replisomes are coupled, the mechanism will extrude the daughter strand and compaction of the bead would be due to this strand extrusion and not topological barriers in the DNA. To test this scenario, additional plasmid with a nicking site is designed to dissipate any torsional strain. Whereby, the compaction reports said strand extrusion and corresponding replication rate.

8 Discussion

A hallmark of several molecular processes in cells is the effect of forces and torques on DNA and corresponding enzymes undergoing conformational changes. Here, DNA replication in bacteria is discussed where translocation of the replication fork along the parental strand leads to a build-up of positive supercoils ahead of the fork. These in turn are relaxed by a class of enzymes called topoisomerases while the newly replicated daughter strands are compacted and segregated by enzymes like structural maintenance of chromosome (SMC) proteins among others. The contents of this study pertained mostly to the investigation of bacterial enzymes, DNA replication and chromosome organization but also delved into further studies of eukaryotic topoisomerases.

8.1 FMT is an ultra-high throughput single-molecule technique

Single-molecule force spectroscopy techniques in the last three decades have yielded a wealth of information about the function of these molecular machines as well as the processes involving complex DNA topology manipulation, phase transitions and force dependent behavior. Optical tweezers as a technique to study biomolecules has made leaps in terms of spatiotemporal resolution. Angular orbital trapping enabled researchers to measure as well as apply torque on molecules simultaneously. While applicable to many biological questions, optical tweezers lack the necessary throughput that scales and often applies to the study of a single-molecule at a time. An optical tweezers setup is also more complex as compared to other contemporary methods such as Magnetic Tweezers and DNA flow stretching. As the latter methods rely on video-based detection of bead displacement, the bandwidth and sensitivity are limited as compared to optical tweezers. Technically, however, both these methods display the capacity to achieve high throughputs and there is a potential to apply forces and control torques on larger fields. This was leveraged to develop flow magnetic tweezers; a Hybrid methods of magnetic tweezers and DNA flow stretching.

Single-molecule methods in past decades were quite cumbersome to apply to a diverse population of enzymes and their complexes, mainly due to limitations in throughput in a single experiment. Several approaches were discussed in earlier sections that provided greater multiplexing including Highly parallel magnetic tweezers, Centrifuge force microscopy and

Acoustic force spectroscopy. There were still some fundamental limitations like dependence of these techniques on high NA optics leading to smaller fields of view and a general lack of usage in large scale studies of enzyme dynamics and function. Development of flow magnetic tweezers addresses this bottleneck that persisted in single molecule biophysics and facilitated large-scale investigations of biological processes involved in nucleic acid transactions.

Flow magnetic tweezers provided a two order of magnitude improvement in general as well as enzymatic throughput as compared to contemporary single-molecule methods (Table 4-1). It can be used to study complex force versus topology relationships in biomolecules and biomolecular systems in a massively parallel manner. This is achieved by reconfiguring the magnetic tweezer tether geometry and applying lateral drag force via flow in a microfluidic chamber. A 7x telecentric lens and a 29 MP camera enables fields as large as 15 mm^2 and upwards of 50,000 molecules are observed in regular experiments. Forces on each of these molecules are determined by numerically solving the equipartition and worm-like chain equations where variance of the bead's excursions lateral to the flow direction serves as the experimental read-out. This method of force determination is then tested using known values of buckling transition for positive and negative plectoneme formation and resolution. Molecule classification during each experiment helps tag each molecule and give context to the enzymatic activity on diverse populations of molecules.

The multiplexing capability of FMT allows for statistically robust quantification of small subpopulations, rare events, and complete force characterization in single experiments. The detection power of FMT was demonstrated by investigating the supercoiling dynamics of gyrase in the presence and absence of ciprofloxacin. We developed a new software platform (Mars) with an automated feature classification pipeline to rapidly analyze the massive amounts of data generated during each FMT experiment. In the case of gyrase, this analysis revealed a broad spectrum of activities including positive supercoil relaxation, negative supercoil introduction, unbraiding, and rare DNA breaks. These applications were complimented by the usage of the same pipeline to analyze diverse type IIA topoisomerases (Characterizing type IIA topoisomerases).

Given that FMT can be implemented using low cost components on standard microscopes, we anticipate applications in a broad range of fields. Moreover, implementing FMT on a traditional magnetic tweezer setup requires only small modifications but results in a substantial improvement in throughput.

8.2 Multiplexed studies of diverse topoisomerases and drug action.

Apart from its ability to resolve positive supercoils in bacteria, DNA gyrase has the unique ability to introduce negative supercoiling using ATP. This made the enzyme an ideal candidate to study topological rearrangement of DNA. Once a DNA molecule was classified to be mobile and coilable, it was left at a positive σ. The rapid extension upon arrival of gyrase signified the resolving of (+) supercoil followed by a pause and introduction of (-) supercoils as the DNA compacted. The velocity of the enzymes were comparable with previous studies by Nöllmann *et al.*[58] and also exhibited similar force-dependent behavior, notably the different modes of gyrase. For forces below ~0.5 pN, gyrase operated in α-mode, where it captures a proximal T-segment of DNA while resolving (+) supercoils and introducing (-) supercoils. For force above ~0.5 pN, the enzyme switched to the χ-mode, identified by the capture of a distal T-segement by gyrase while only resolving (+) supercoils and not introducing any (-) supercoils. The field of heterogeneous DNA molecules served as a perfect playground for enzymes as the DNA molecules existed over a diverse force spectrum and configurations. Even nicked- or catenated DNA molecules conveyed gyrase dynamics of transient binding and unbraiding respectively.

A crucial step in gyrase cycle is the strand-passage during which the enzyme introduces a double-strand break in the chromosome. Antibiotic and anticancer drugs take advantage of this intermediate step by forming a stable enzyme-drug complex and arresting the cycle. If these breaks are not resealed, the resulting double-strand breaks could be catastrophic for an organism. Increasing concentrations of ciprofloxacin result in reduce efficacy of gyrase to both relax and introduce (+) and (-) supercoils respectively. Gyrase-drug complexes are remarkably stable. No dose-dependent increase of DNA breaks was observed under normal buffer conditions or in response to extreme positive or negative torque for 10s of thousands of molecules. The improved detection power of FMT did reveal rare DNA breaks during bursts of gyrase activity, however, these occurred with equal frequency independent of drug concentration. The transient DNA breaks stabilized by ciprofloxacin were only converted into irreversible breaks that triggered bead loss in the presence of detergent. The stability of gyrase-drug complexes under extreme torques suggests that the positive supercoils generated ahead of an advancing transcription or replication complex are not sufficient to generate breaks. Instead a physical encounter is likely required to convert transient breaks into irreversible breaks[92] that are ultimately exposed to the cell during failed repair attempts[93]. The improved throughput of FMT allows for direct characterization of the dynamics of encounters of complex machineries[94], which were previously out of reach.

Diverse homologs of the same family of enzymes in different species have distinct physiological roles in the cells. The throughput provided by FMT makes it an ideal platform to rapidly characterize and compare various enzymes. Following gyrase, a screen of various eukaryotic topoisomerases was conducted. With similar experimental buffer, conditions and parameters in the analysis pipeline, final comparative plots conveyed enzymatic and temporal information among different eukaryotic topos at a glance. For relaxation of (+) supercoils, scTop2 displayed rates similar to those of prokaryotic enzyme DNA gyrase from *E. coli*. This rate was not comparable with other eukaryotic topos as suggested by Le *et al.*[89] and was almost half of what was suggested by the study. While the experiment was performed in a buffer of similar composition, the concentration of the enzyme was more in the FMT experiment. Other factors that might have influenced these differences in velocities could be the temperature at which the experiments were performed or the differences in forces on the nucleic acids among both experiments.

Two human isoforms of topoisomerases II: namely hTop2α and hTop2β were also screened in our study. Rates of hTop2α were comparable with other eukaryotic topos and a previous study by Seol *et al.*[88]. The heterogeneity in the (+) supercoil relaxation velocity for hTop2α was also observed in our study. The rate of hTop2β couldn't be related to any previous literature value but a comparison to hTop2α could be made. Activity of hTop2α is known to be writhe dependent as it chirally discriminates relaxation of (+) supercoils more than the relaxation of (-) supercoils. hTop2β shows chiral-independence and relaxes both (+) and (-) supercoils equally[88]. The higher velocity of hTop2α points towards its preference of (+) supercoil relaxation over hTop2β. Additional experiments however are needed where similar screens are done to resolve (-) supercoils and discern any possible changes in rates as compared to (+) supercoil relaxation.

Studying DNA double-strand breaks is another aspect from the gyrase experiments that will be applied to detect such breaks by eukaryotic topoisomerases. For our studies, two point-mutants of the isoform hTop2β are made that are supposed to be more prone to said breaks. The mutation βVtoI (V111I: Valine to isoleucine at position 111) resides in the ATP-binding pocket and disrupts ATP hydrolysis *via* steric hinderance of ATP binding during enzymatic activity. This could indirectly lead to a double-strand break as energy transduction is inhibited. The effects of this mutation can be seen in the rates of βVtoI as the velocity is almost halved as compared to WT hTop2β. Similar results (data not shown) were seen for the mutant βRtoW (R757W: Arginine to tryptophan at position 757) although more experiments are needed to get higher throughput results. This mutation finds itself close to the dimeric interface of cleavage domains and DNA; and can thus directly influence dimer formation and dissociation, causing breaks.

With time and additional experiments, clues could be gathered as to why various type IIA topos differentially specialize for topology simplification. Also studies of double-strand breaks will help decipher the mode of action of these enzymes in absence and presence of a drug while expanding our understanding of drug action in organisms. Characterization of other major classes of antibiotics and anticancer drugs[16] that target both bacterial and eukaryotic topoisomerases promise to clarify the biophysical properties of critical intermediates in the pathways of drug inhibition and DNA break formation. FMT and the software platform developed can be easily tailored to studies of a broad range of enzymes that conduct nucleic acid transactions.

8.3 Mechanism of topological rearrangement by *E. coli* DNA replisome

The E. coli replisome replicates at around 600-1000 bases per second. The unwinding of parental strand leads to a build-up of (+) supercoils ahead of the fork. For an efficient replication cycle, DNA gyrases accumulate in front of the fork to resolve these topological barriers[10] while avoiding any toxic collisions with the fork. As the fork approaches replication termination and the parental strand shortens, the segregated daughter strands titrate away any active topoisomerases. The machinery should thus have an intrinsic mechanism to deal with the topological stress. Fork rotation is one such mechanism where the (+) superhelical stress diffuses through the fork and forms precatenates behind it. Other mechanisms include fork pausing and decoupling of either the leading- or the lagging strand to release excess torsional strain[13]. These were discussed in the section: Topological Stress during DNA replication. A failure to resolve these coils could result in fork collapse.

Although single-molecule studies of the replisome were conducted successfully in the past and a lot of information regarding the dynamics and coordination was gathered, the DNA substrates were relaxed and not topologically constrained. This loss of topological information could have altered how the dynamics of these complexes were perceived. A simple reaction with phi29 DNA polymerase on a topologically constrained substrate shows the accumulation of positive coils in front of the fork. The design of this substrate is inspired in part from previous DNA constructs where a primed leading strand is also tethered to the surface along with the lagging strand. The molecule is shown to be coilable and compaction is reported to be 3-6 times higher than the replication compaction of phi29 polymerase on a nicked or a relaxed substrate. The throughput here however, is extremely poor owing to the lack of multiple attachment sites of the DNA substrate on the slide surface.

A better alternative in this case is a substrate akin to the 21 kb DNA used for the topoisomerases experiment. For easier synthesis and higher coilability of the molecule, a substrate containing the *E. coli* origin of replication site (*OriC*) was designed. The final plasmid containing *OriC* could easily propagate in *Dh5α* bacteria and method to synthesize the substrate remained similar to the original topoisomerase substrate. As all other replication proteins required are available in the lab except DnaA, a plasmid was designed by inserting DnaA gene in 1B vector using Gibson assembly. The presence of the gene was confirmed using restriction analysis of the vector and the final plasmid. There was no conclusive result of the incorporation when the plasmid was sequenced. A replication reaction can be attempted upon expression and purification of DnaA enzyme.

The *OriC* site contains DNA boxes with high affinity for DnaA where binding of the protein melts the AT-rich DNA unwinding region and promotes loading of the helicase-loader complex. This serves as an initiation for bidirectional replication by two replisomes. The OriC substrate is designed with the *OriC* site on one extremity of the substrate. The objective is to halt one replisome while the other replicates the parental strand. The effects of a complete replication on a topologically constrained substrate and the different scenarios such a rotation, pausing or collapse of the fork could thus be observed. The complex can then be modified further by including additional components such as DNA gyrase, topoisomerase IV and SMC proteins. One can potentially study fork collision with an attempt to convert the transient breaks made by gyrase into irreversible breaks during replication. In case the two replisomes are physically associated, compaction of the bead could result from extrusion of the daughter strands and not due to any changes to parental strand topology (or it could be a mix of both). Additional plasmids are being designed where a nicking site is introduced in the plasmid to dissipate any topological barriers and only observe the compaction due to strand extrusions.

For replication reactions, stoichiometry of individual components or mutants could be manipulated and introduced in the flow cell. Different DNA sequences and constructs are designed to tailor the experiments and confirm hypotheses. The rapid analysis pipeline can be used to interpret data and conduct several back-to-back experiments. FMT serves as a versatile technique and yet uniquely suited to study the effects of DNA topology on multi-molecular complexes and vice-versa. The high-throughput makes it an ideal tool to study DNA breaks and enzyme collisions. FMT opens new frontiers in single-molecule biophysics by enabling statistically robust studies of enzyme dynamics and will act as a tool for discoveries of rare and divergent behavior in single enzymes and enzyme complexes.

9 Materials and Methods

9.1 Experimental Setup

All single-molecule force and topology studies were conducted on a setup constructed as follows. A 29-megapixel charge coupled device (29M Prosilica GX6600 GigE Monochrome camera, Allied Vision 6576 x 4384 pixel dimensions) was mounted directly to a 7x telecentric line scan lens (TL12K-70-15, Lensation GmbH, numerical aperture of 0.23)[47] generating a field of view of ~15 mm^2. Each pixel represented 0.78 µm x 0.78 µm at 7x magnification and 1x binning. The Lens-Camera assembly was mounted on a vertical translation stage (Newport, M-MVN50) for focusing and positioned below an XY-translation stage (Physikinstrumente M-545.2ML) for sample alignment. A custom-machined holder was used for mounting on the stage and sealing a PDMS flow cell. The flow cell consisted of two inlets and one outlet tube, where the latter was attached to an appropriate flow sensor: BFS, Microfluidic Coriolis flow sensor, Bronkhorst-Elveflow or MFS3, Microfluidic Thermal flow sensor, both purchased from Elveflow and connected to an OB1 pressure control system. The two inlets allow for fast switching between buffers without disrupting flow. Negative and positive pressure was applied using vacuum and nitrogen outlets. Flow profiles were programmed and controlled using ESI microfluidic software from Elveflow. The magnetic tweezers were mounted above the flow cell and consisted of two antiparallel 1 cm neodymium (supermagnete, W-10-N) block magnets placed 6 mm apart. Vertical translation and rotation of the magnets was achieved using dc servo motors (M-126.PD1, C-150.PD, 2x C863, Physikinstrumente) mounted on a rail tower for course vertical alignment (X95, M-CSL95-80, Newport) with an additional linear stage for centering the magnets over the sample (PT1/M, Thorlabs). Additional posts, and clamps for mounting, were either custom machined in house, or purchased from Thorlabs or Newport. Magnets were kept at a constant height above the flow cell for all experiments and only changes in flow were used to alter applied force on the beads. A fiber illuminator (OSL2, OSL2FB, OSL2COL, Thorlabs) was setup laterally to the flow cell to illuminate the beads in a dark field. Videos were acquired using StreamPix 6 software suite (Norpix) typically at 4 Hz or 33 Hz with 2x binning enabled to improve readout performance.

9.2 Flow cell setup

Glass coverslips (60 mm x 24 mm) were functionalized as previously described (Figure 9-1 A).[47] They were placed inside a plasma cleaner (Zepto B, Diener electronic) and cleaned under occasional influx of oxygen for 20 minutes. The surface was silanized by incubating the plasma-cleaned slides in a 2% v/v solution of freshly opened APTES (aminopropyltriethoxysilane, ROTH) in acetone. A solution of inert and biotinylated PEG (MPEG-SC-5000-5g, Biotin-PEG-SC-5000-1g, Laysan Bio Inc.) in the ratio 12%:1% (w/v) was dissolved in 0.1M $NaHCO_3$ at pH of 8.2. The PEG solution was put between two stacked silanized slides overnight, after which the slides were washed, dried and stored in vacuum for up to a month at a time. Prior to experiments, slides were incubated with 0.2 mg/ml streptavidin (Streptavidin from *Streptomyces Avidini*, Sigma-Aldrich) in 1x working buffer.[47] A PDMS cover with an embedded lane was placed on the coverslip and sealed using a frame built into the flow cell holder. The inlet tubes had an inner diameter of 0.58 mm and an outer diameter of 0.96 mm (PE tubing PORTEX, SX05, laborversand.de) and the outlet tube was 1/32" ID PTFE tubing (Darwin microfluidics). Following the setup of the flow cell on the microscope, the cell is flushed with the given buffer (1x PBS for force calibration, buckling and supercoiling experiments and 1x Gyrase buffer for the enzymatic experiments) and incubated for at least 30 min (Figure 9-1 B). The topologically constrained DNA (5 pM), with biotins on one end and digoxigenins on the other (DNA preparation), was introduced to the flow cell at a constant flow rate for 30 minutes to allow time for attachment to streptavidin molecules on the surface. After incubation with the DNA, Anti-DIG fab fragment coated beads were flushed into the flow cell for attachment to the exposed digoxigenin end. Once sufficient bead attachment is observed, excess beads are washed out of the flow cell and the magnet is lowered into position. Mobile tethers are then identified using a flow reversal step (Supplementary movie 1) and coilable tethers were identified with a series of coiling steps using the magnets (Supplementary movie 2). The buffer used for supercoiling, force calibration and buckling experiments contained 0.01 M phosphate buffer, 2.7 mM KCl, 0.137 mM NaCl (1xPBS tablet solution from Sigma), 0.1 mg/ml BSA, and 0.1 % TWEEN20. Gyrase reaction buffer contained 35 mM Tris-HCl (pH 7.5), 24 mM potassium glutamate, 4 mM $MgCl_2$, 2 mM DTT, 0.2 mM spermidine, 1 mM ATP (ATPγS), 6.5% (v/v) glycerol, 0.1 mg/ml BSA, 0.1 % TWEEN20 and indicated amounts of DNA gyrase, typically 0.2 nM.[58] Where indicated ciprofloxacin (17850-5G-F, Sigma) was added at the concentrations specified.

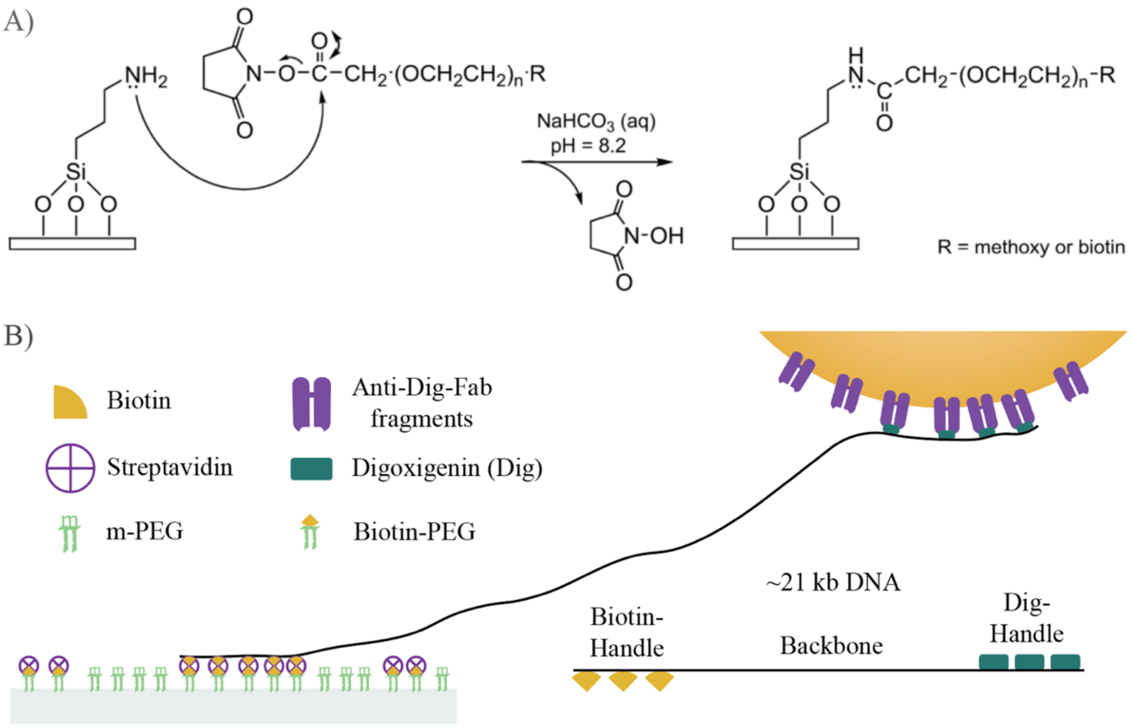

Figure 9-1 Preparing the flow cell. A) The glass coverslips were cleaned under occasional influx of oxygen in a plasma cleaner for 20 min followed by silanization in acetone. The nucleophilic amino group attacks the electrophilic carbonyl carbon in succinimidyl ester PEG causing removal of N-Hydroxysuccinimide (NHS) in a 0.1 M $NaHCO_3$ solution with pH 8.2. The functionalized surface contains inert and biotinylated PEG in the ratio 12%:1%(w/v). The slides are stored in vacuum chamber and retrieved prior to the experiment. B) A solution of 0.2 mg/ml Streptavidin is incubated on the slide and washed off before covering the surface with PDMS cover containing an embedded lane. The 21 kb DNA containing biotin and dig moieties is flown in where the biotin side attached to the surface. Micron size beads enveloped in Anti-dig fab fragments are then introduced in the flow cell.

9.3 DNA and bead preparation

The torsionally constrained DNA constructs were ~21 kb in length which corresponded to a contour length of 6.8 µm. They were generated using the plasmid Supercos1-Lambda 1,2 generated in *E. coli* cells as previously described.[39,95] To avoid damaging the final DNA substrate (20666 bps), a Chargeswitch Plasmid miniprep kit (Invitrogen) was used to extract the plasmid. The plasmid was then double-digested using NotI and XhoI sites and purified again using a Chargeswitch PCR clean-up kit (Invitrogen). Once digested, the segments were ligated (T4 DNA ligase, NEB) to DNA linker fragments (~600 bp) that had biotinylated and digoxigenated (DIG) dUTP moieties incorporated via PCR (polymerase chain reaction).[96] The beads (1µm Dynal MyOne, Invitrogen 650-01) were prepared as follows. They were washed in 0.1 M Borate buffer (H_3BO_3) at pH 9.5 and incubated under constant overnight shaking with DIG antibody Fab fragments (Roche diagnostics GmbH) in Phosphate-buffered saline (PBS) at 37° C. Excess fragments were washed away using Tris-HCl buffer and stored for months in the same at 4° C.[47] The bead stock was sonicated for 1 min and mixed prior to dilution in the experimental buffer (either PBS or gyrase buffer).

9.3.1 Handles with dUTPs containing Digoxigenin and Biotin moieties

The approximately 600 basepairs long handles were made with a PCR using bacteriophage λ DNA as template in 2 parts.

Table 9-1 Reaction volumes for a 3 x 50 µl reaction with Phusion polymerase.

Component	Volumes	Final Concentration
Nuclease-free water	109.5 µl	
5X Phusion HF Buffer	30 µl	1X
10 mM dNTPs	3 µl	200 µM
100 µM Forward Primer	0.75 µl	0.5 µM
100 µM Reverse Primer	0.75 µl	0.5 µM
48 kb bacteriophage λ DNA	1 µl of 50 ng/µl stock	
DMSO	4.5 µl	3%
Phusion DNA Polymerase	1.5 µl	

Restriction site dependent forward and reverse primers were used.

NotI forward:	5’ TAT TAG CGG CCG CGA TTG TTC TTT ATT CAT TTT 3’
NotI reverse:	5’ CCC ATC GGA AAA CTC CTG CTT TAG C 3’
XhoI forward:	5’ TTA CCG CAT ACC AAT AAC GCT TCA C 3’
XhoI reverse:	5’ GAA ACT CAA CAT CGT CAT CAA ACG C 3’

Following program was used in a thermocycler on 3 x 50 ul reactions.

Table 9-2 PCR program for Phusion polymerase reaction to make handle templates.

Steps	Temprature	Time
Initial Denaturation	98°C	180 seconds
30 Cycles	98°C	30 seconds
	55°C	30 seconds
	72°C	180 seconds
Final Extension	72°C	600 seconds
Hold	10°C	∞

The template segments are then obtained through gel purification using QIAprep Spin miniprep kit. These fragments are used further for PCR with Taq DNA polymerase.

Table 9-3 Reaction volumes for a 3 x 50 µl reaction with Taq polymerase to incorporate Biotin (Digoxigenin) with NotI (XhoI) fragment respectively.

Component	Volumes	Final Concentration
Nuclease-free water	117.5 µl (119.5 µl)	
10X Thermopol Buffer	15 µl	1X
10 mM dNTPs	3 µl	200 µM
1 mM Biotin (Dig) -dUTP	4.5 µl (2.5 µl)	30 µM
100 µM NotI (XhoI) forward	0.75 µl	0.5 µM
100 µM NotI (XhoI) reverse	0.75 µl	0.5 µM
NotI (XhoI) fragment	1 µl of 50 ng/µl stock	
DMSO	4.5 µl	3%
Taq DNA Polymerase	3 µl	

Table 9-4 PCR program for Taq polymerase reaction to make Biotin (Dig) incorporated handles.

Steps	Temprature	Time
Initial Denaturation	95°C	180 seconds
35 Cycles	95°C 60°C 68°C	30 seconds 30 seconds 180 seconds
Final Extension	68°C	600 seconds
Hold	10°C	∞

The plasmid backbone is then ligated with NotI restriction sequence to the biotin handle and XhoI to the dig handle to get the final construct as shown in Figure 9-1 B.

9.4 Designing the OriC plasmid

A plasmid containing the *E.coli* OriC was generated using T5 exonuclease DNA assembly (TEDA).[97] The backbone, p221 donor plasmid, was amplified using the following primers:

p1 Forward: 5’ GTC ATA GCT GTT TCC TGG C 3’
p1 Reverse: 5’ GAC TGG CCG TCG TTT TAC 3’

The insert, *E.coli* OriC, was amplified from *DH5α E.coli* using the following primers:

OC1 Forward: 5’ CGA CGG CCA GTC GTC GAC GTC GGC TTG AGA AAG ACC 3’
OC1 Reverse: 5’ CAG GAA ACA GCT ATG ACT GAC ACC TTT TGT GGG GC 3’

This plasmid contained an origin of replication, a Kanamycin resistance cassette and the OriC as insert, flanked by the universal sequencing primers M13F and M13R. The fragments were gel purified in every step and the inserts were checked by sequencing with M13F and M13R. In this step a SalI restriction site was inserted with the forward primer. A NotI restriction site was inserted in the generated plasmid using the Q5® Site-Directed Mutagenesis Kit (NEB, #E0554S) and the following primers:

OCN Forward: 5’ TTG CGG CCG CAA TTT AAG TCG ACG TCG GCT TGA GA 3’
OCN Reverse: 5’ GAC TGG CCG TCG TTT TAC 3’

The insertion was validated by sequencing with the M13R primer.

Supercos1-lambda1,2 plasmid[95] was used as a template to generate a 21 kb plasmid where an *E. coli* OriC site was incorporated using T5 exonuclease DNA assembly (TEDA).[97] The incorporation was confirmed by forward and reverse sequencing from M13 primer. Following primers were used to generate DNA fragments *via* PCR.

Fragment 1 is 10,583 basepairs and contains the Ori site for the plasmid as well as the Ampicillin resistance.

F1 forward: 5’ GCG TGG ATA GCA CCA TTT GCG 3’
F1 reverse: 5’ TTG AAG ACG AAA GGG CCT CG 3’

Fragment 2 is 10,095 basepairs.

F2 forward: 5’ GGT GCA TCC CTC AAA ACG AG 3’
F2 reverse: 5’ CCT GAT CGC AAA TGG TGC TAT CC 3’

Fragment 3 is 592 basepairs and contains the *E. coli* OriC site obtained from the previously generated NotI-SalI OriC containing plasmid.

F3 forward: 5’ GGC GTA TCA CGA GGC CCT TTC GTC TTC AAT TGT AAA ACG ACG GCC AGT C 3’

F3 reverse: 5’ GGG ATT TTC CCT CGT TTT GAG GGA TGC ACC TGC CAG GAA ACA GCT ATG AC 3’

The fragments were synthesized in a final volume of 25 µl using Q5 hot Start 2X master Mix following instructions from the manufacturer. The melting temperature (Tm) was calculated using NEB Tm calculator. They were then recovered through gel purification using NucleoSpin Gel and PCR Clean-up, Mini kit (MACHEREY-NAGEL, REF 740611.250). Following TEDA, the annealed fragments were directly transformed into Dh5α strain of *E. coli*. Plasmid extraction in every step was performed using NucleoSpin Plasmid, Mini kit for plasmid DNA (MACHEREY-NAGEL, REF 740588.50).

9.5 Data availability

Raw videos for reproduction of the essential results are available at Zenodo with the following titles and links:

Flow Magnetic Tweezers: Gyrase dynamics in absence of drug ciprofloxacin (https://doi.org/10.5281/zenodo.3981513),Flow Magnetic Tweezers: Gyrase dynamics in presence of 20 uM drug ciprofloxacin (https://doi.org/10.5281/zenodo.3981123),Flow Magnetic Tweezers: Gyrase dynamics under 3 different external torque conditions. Part 1/3 (https://doi.org/10.5281/zenodo.3981531),Flow Magnetic Tweezers: Gyrase dynamics under 3 different external torque conditions. Part 2/3 (https://doi.org/10.5281/zenodo.3981542), Flow Magnetic Tweezers: Gyrase dynamics under 3 different external torque conditions. Part 3/3 (https://doi.org/10.5281/zenodo.3981545).

Additional data and instructions available upon request.

9.6 Code availability

The analysis software used for this work is open source and publicly available in several repositories on Github at https://github.com/duderstadt-lab. The core data model implementation and plugins used for data processing and storage are available at http://github.com/duderstadt-lab/mars-core and the graphical user interface used for classification and plotting is available at http://github.com/duderstadt-lab/mars-fx. The plugin used for length conversion from pixels to microns is available at http://github.com/duderstadt-lab/mars-fmt. Scripts used for region definitions and automated feature classification can be found at http://github.com/duderstadt-lab/fmt-scripts. To facilitate the general use of our software, we have created an ImageJ update site at http://sites.imagej.net/Mars/ and a documentation site http://github.com/duderstadt-lab/mars-docs. The plugins can very easily be installed by adding the update site to any local copy of Fiji. The use of specific commands is described in detail on the documentation site.

10 Appendix I: Schematics of flow magnetic tweezers

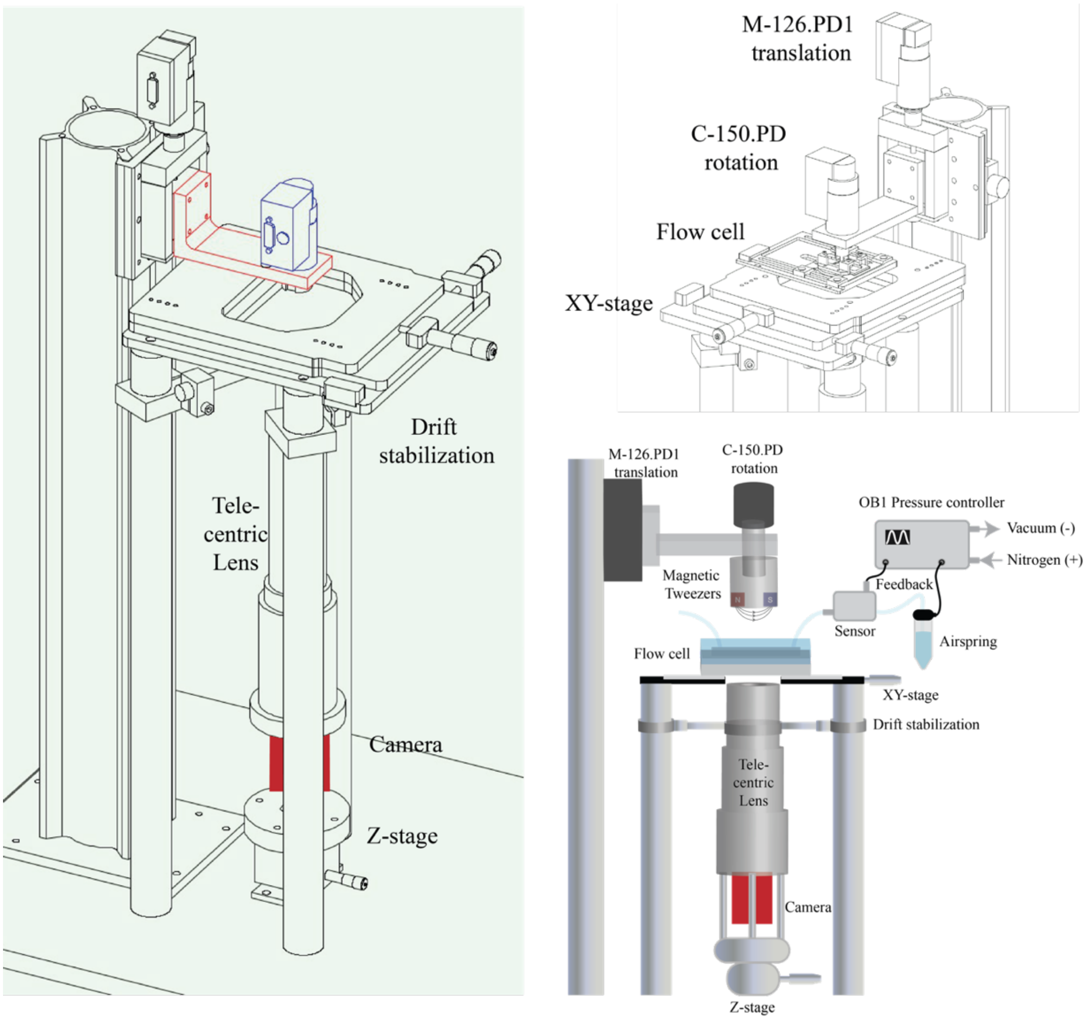

Figure 10-1 Schematic of Flow Magnetic Tweezers: A 7x telecentric lens is attached directly to a 29 MP camera and mounted on a z-stage to adjust the focus of the field. Due to the large size and vertical orientation of the camera-lens setup, the system is prone to drift. Hence, the lens is clamped to the pillars through a stiffner shaft (see Drift Stabilization). Flow cell is attached to the xy-stage to further reduce drift. A PDMS cover with inlet and outlet holes is mechanically fastened to a functionalized coverslip in the flow cell holder (see Flow cell holder). A heater plate is fastened between the flow cell holder and xy-stage to heat the lane (see Stages). The magnetic tweezers are mounted on top of the flow cell where dc servo motors M-126.PD1 and C-150.PD control the translation and rotation respectively (see Magnetic Tweezers). The flow control system consists of a OB1 pressure controller attached to a vacuum inlet (for negative) and a nitrogen inlet (for positive) to regulated flow through a feedback-controlled sensor (MK3+). Detailed information of the components, their costs and vendor are given in Table 10-1. (credits: CAD schematics by Chris Duderstadt)

10.1 Drift Stabilization

1) Lens Ring

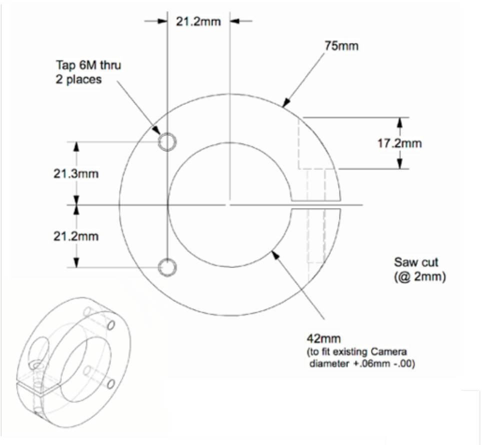

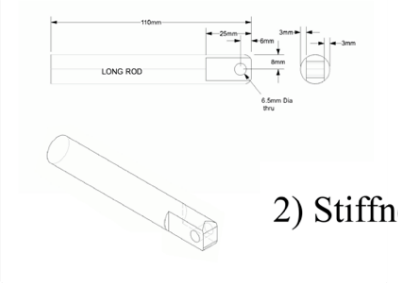

2) Stiffner Shaft

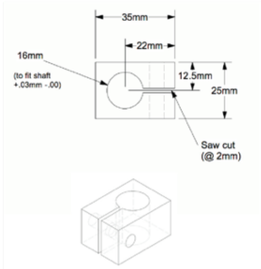

3) 16mm Clamp

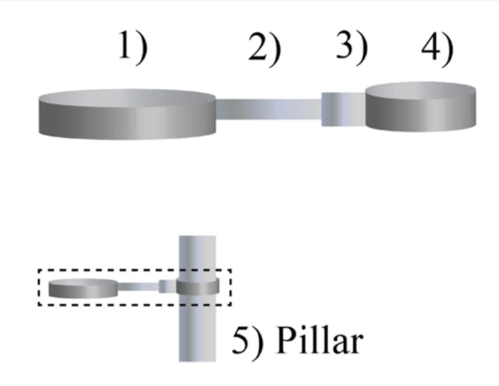

5) Pillar

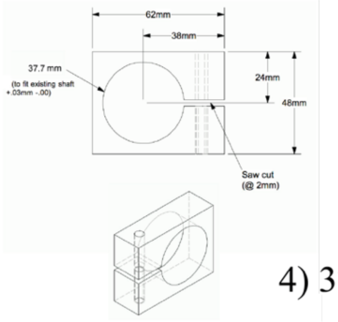

4) 37.7mm Clamp

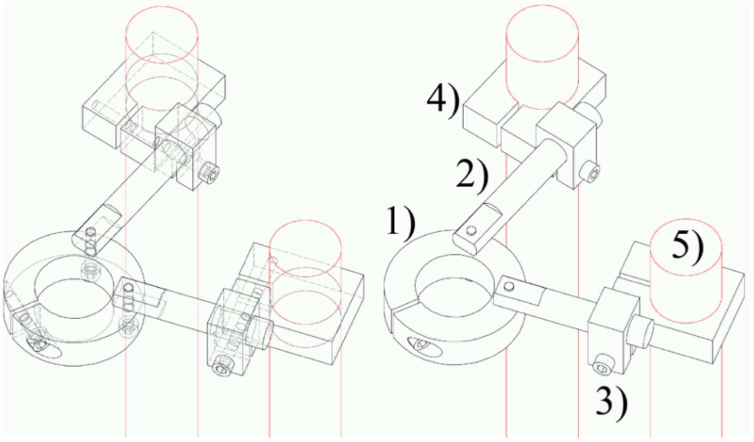

drift stabilization:
Final assembly

10.2 Flow cell holder

6) flow cell hot stage

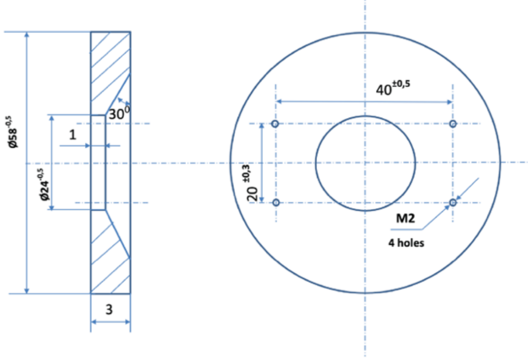

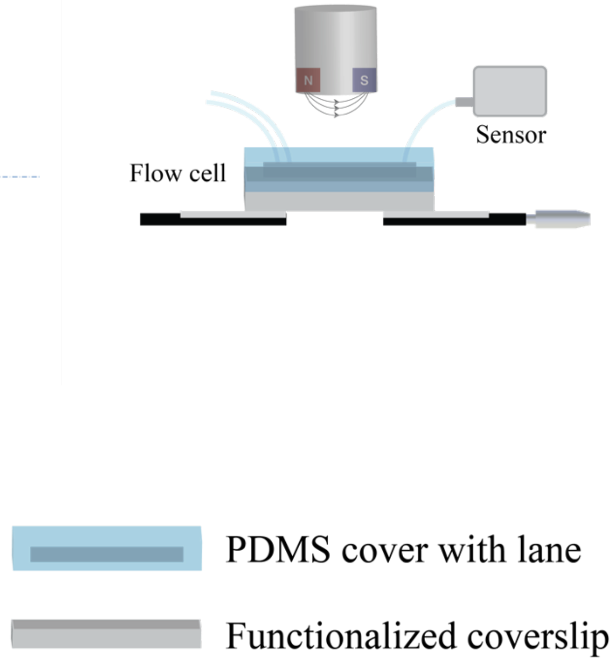

7) flow cell clamping arm

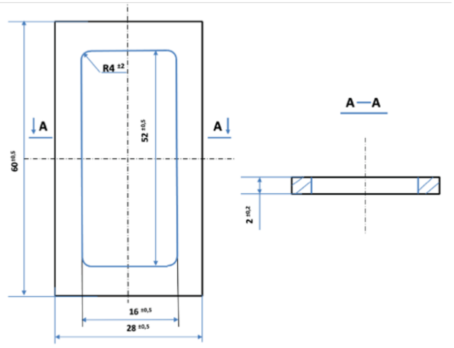

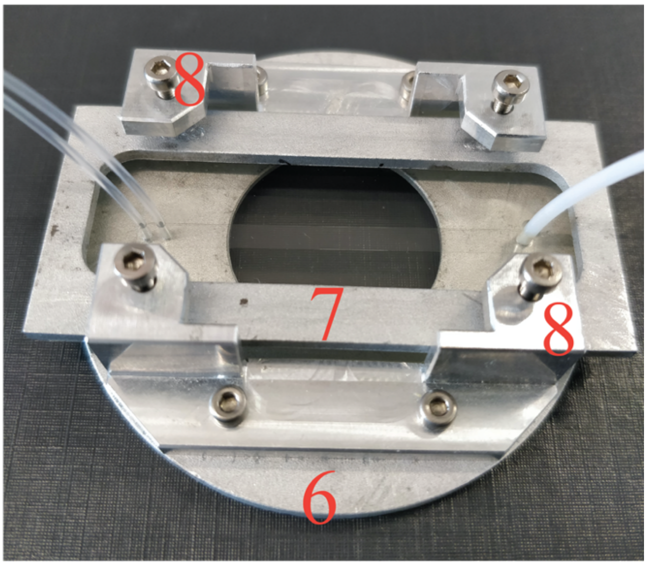

8) flow cell adapter plate

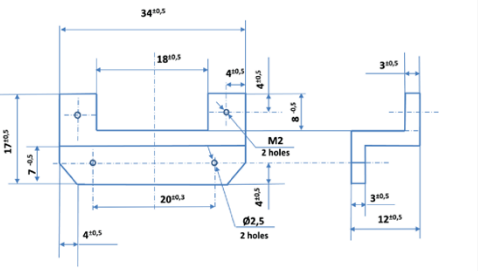

10.3 Stages

9) XY-stage (black)

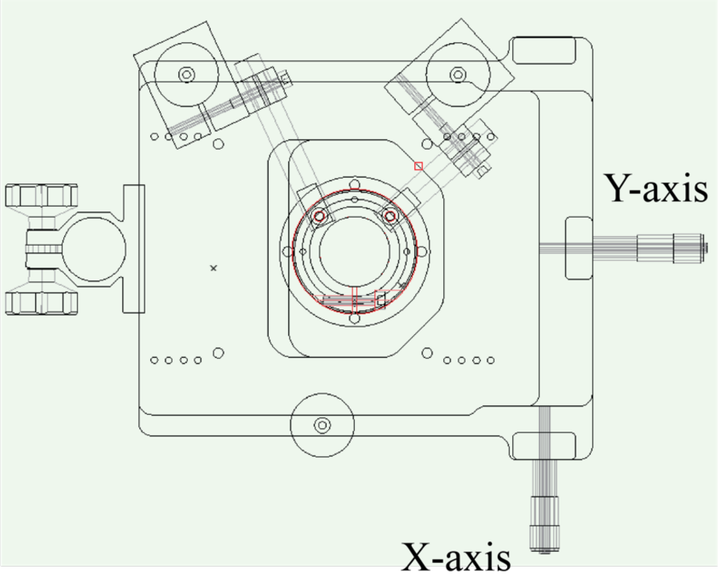

10) Heater plate (gray)

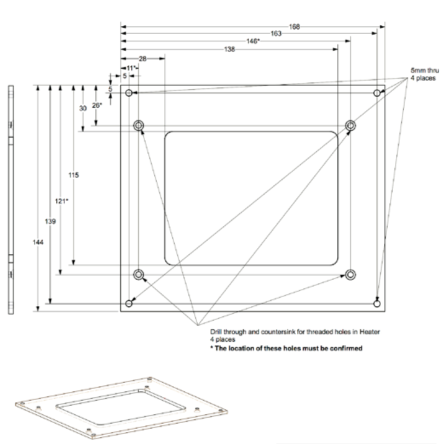

11) Camera vertical mount

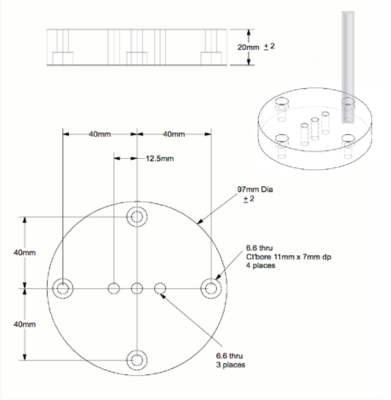

12) mvn50 vertical linear stage

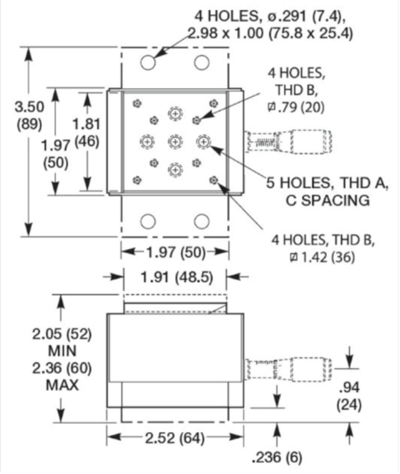

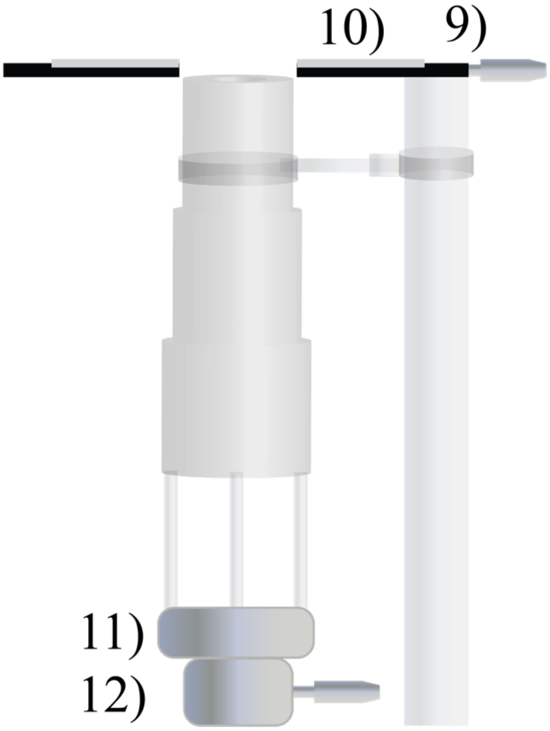

10.4 Magnetic Tweezers

13) Rotary mount vertical plate

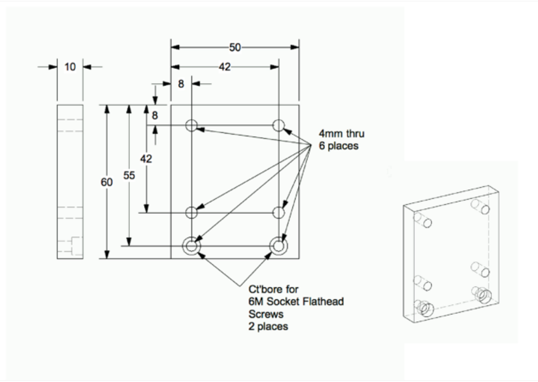

14) Rotary mount horizontal plate

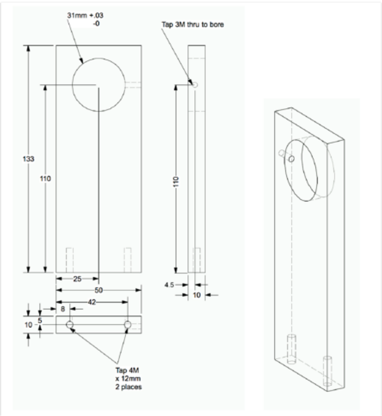

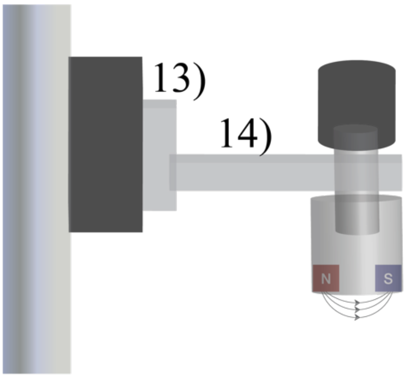

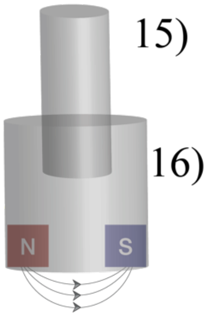

15) Rotary brushing

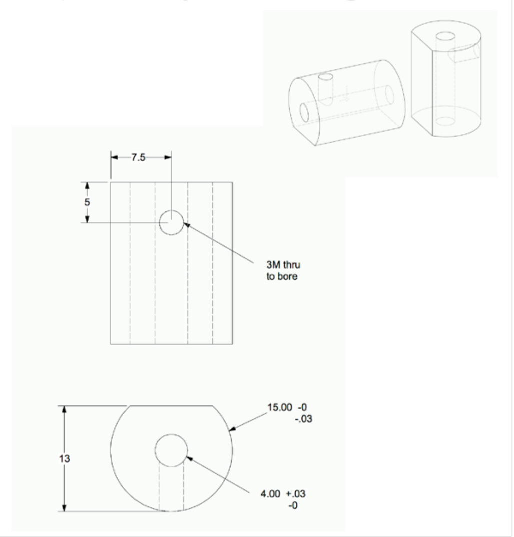

16) 10 mm magnetic holder

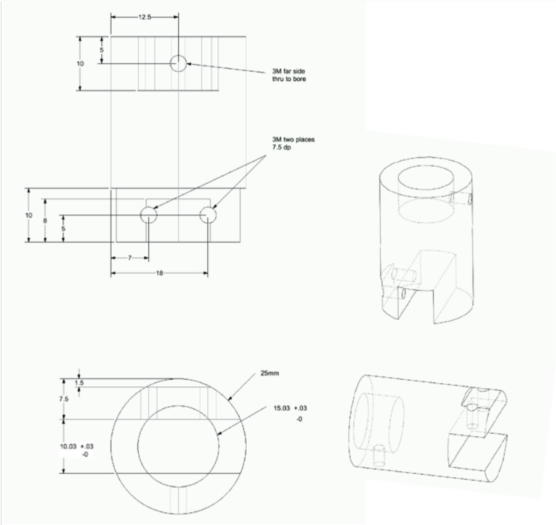

10.5 Components, vendors and costs

Table 10-1 Parts list of FMT setup including vendors and prices in euros

Item Description	Item Number	Vendor	Price €
Camera, Table and Lens			
29 MegaPixel camera from Allied Vision (GX6600 PROSILICA 35m CCD Mono)	-	Allied Vision	10,069
Ultra wide field lens with custom mount TL12K-70-135	TL12K-70-135	Lensation	12,000
XY Microscope Stage, 25 mm x 25 mm, Micrometer Drive, High Stability	M-545.2ML	PI	3481
TMC-78-241-12R (1 m x 1 m x 100 mm) Optical Table	TMC-78-241-12R	TMC	2,100
TMC-12-416-33 Support system with tiebars	TMC-12-416-33	TMC	2,920
Magnetic Tweezers components			
Translation Stage, 25 mm, ActiveDrive DC Motor (Includes 24V Power Supply)	M-126.PD1	PI	1,970
Rotary servomotor ActiveDrive DC Motor / Encoder, 30 W, Incl. 24 V Power Supply	C-150.PD	PI	993
Mercury DC-Motor Controller, 1 Channel, Wide range P/S	C-863.11	PI	651
Mercury DC-Motor Controller, 1 Channel, Wide range P/S	C-863.11	PI	651
Flow controller components			
Base module of the OB1 MkIII+ pressure controller	OB1MkIII+-MIX-	Elveflow	1,350
OB1 MkIII Channel -900/1000	VAN	Elveflow	700
Flow Sensor 3 New Version	Flow-03	Elveflow	1,050
Kit Tank M - 50mL	KRM	Elveflow	70
Kit 1/16 Spare Roll Teflon - 50	KTSR50	Elveflow	90
Kit 1/4-28"	K1/4-28	Elveflow	35
Kit Luer Lock	KLL	Elveflow	70
Flow Sensor Premium BFS1+	MFS-P+-	Elveflow	6,885
OB1 MkIII Performance Pack	OB1 MkIII	Elveflow	450
Kit Reservoir Tank M - 2 ports 50mL 2017	KRM1	Elveflow	174
Kit Fitting Starter Pack Luer	StartPackLuer	Elveflow	745.5
Syringe pump	NE1000-X		650
Other components			
Precision Ball Bearing Vertical Linear Stage, 8 mm Travel, Metric	M-MVN50	Newport	578
Base Plate, Used with UMR5 Series, MVN50 & UTR46 Series	M-PBN5	Newport	50
Differential Micrometer, 25.1 mm Coarse, 0.1 mm Fine, 6.6 lb Load	DM11-25	Newport	343

Aluminum Structural Rail, 750 mm Length, M6 Threads, X95 Series	X95-0.75	Newport	115
Rail Carriage, 120 mm Length, M5 and M6 Thread, X95 Series	M-CXL95-120	Newport	98
PBN Series Base Plates, Use with UTR160 Series Rotation Stages	M-PBN16	Newport	130
Rail Carriage, 50 mm Length, M6 Thread, X95 Series	M-CXL95-50	Newport	74
Ø1.5" Mounting Post, M6 Taps, L = 25 mm	P25/M	Thorlabs	17.55
Studded Pedestal Base Adapter, M6 x 1.0 Thread	PB4/M	Thorlabs	11.16
Clamping Fork for Ø1.5" Pedestal Post	PF175	Thorlabs	15.72
Ø1.5" Mounting Post, M6 Taps, L = 300 mm	P300/M	Thorlabs	71.1
Ø1.5" Mounting Post, M6 Taps, L = 250 mm	P250/M	Thorlabs	61.2
PB2/M - Metric Mounting Post Base, Ø61 mm x 12.7 mm Thick	PB2/M	Thorlabs	24.12
P150/M - Ø1.5" Mounting Post, M6 Taps, L = 150 mm	P150/M	Thorlabs	44.1
Ø1.5" Post Mounting Clamp, 64 mm x 64 mm, Metric	C1511/M	Thorlabs	57.6
Aluminum Breadboard, 250 mm x 300 mm x 12.7 mm, M6 Taps	MB2530/M	Thorlabs	116.1
Ø12.7 mm Optical Post, SS, M4 Setscrew, M6 Tap, L = 75 mm, 5 pack	TR75/M-P5	Thorlabs	21.95
Light source			
Ø12.7 mm Pedestal Post Holder, Spring-Loaded Hex-Locking Thumbscrew, L=154.7 mm	PH150E/M	Thorlabs	23.85
Ø12.7 mm Optical Post, SS, M4 Setscrew, M6 Tap, L = 300 mm	TR300/M	Thorlabs	9.74
Adjustable Lens Mount: Ø0.28" (Ø7.1 mm) to Ø1.80" (Ø45.7 mm), M4 Tap	LH1/M	Thorlabs	35.55
High-Intensity Fiber-Coupled Illuminator with 91 cm (36") Long Fiber Bundle	OSL2	Thorlabs	807.3
Long Clamping Fork, 1.76" Counterbored Slot, Universal	CF175	Thorlabs	8.91
Total			49,818

11 Appendix II: Setting up a FMT experiment and molecule characterization

This chapter describes how to setup a FMT experiment by preparing the flowcell, assembling DNA-bead tethers and performing characterization steps for an arbitrary experiment.

11.1 Preparing the flowcell for an experiment

- A functionalized coverslip is taken from the vacuum and placed on a tube holder.
- 100 µl of working buffer (20mM Tris-HCl pH=7.5, 2mM EDTA, 50mM NaCl) is added to 25 µl streptavidin aliquot (Stock: 1 mg/ml) giving a final concentration of 0.2 mg/ml.
- The streptavidin drop is pipetted in the middle of the coverslip with holes on the tube holder being used as references and incubated for 10 minutes.
- The PDMS flowcell cover is cleaned with Triton and milliQ water.
- the cover as well as the functionalized coverslip is blow dried with a nitrogen gun.
- The PDMS flowcell cover is placed on top of the coverslip.
- Two inlet tubes of approximately 22 cm are plugged in the inlet holes.
- Prepared flow cell is placed in the Flow cell holder.

11.2 Assembling DNA-bead tethers

- Once the flow cell holder is fastened onto the stage, the flow cell is flushed with the relevant buffer while avoiding introduction of bubbles in the flow lane.
- Outlet tube is plugged into the sensor and left to run while any residual air bubbles subside and the flow stabilizes.
- DNA at approximately 5 pM concentration is introduced in following steps:
    - 25 µl/min for 90 seconds
    - 5 µl/min for 30 minutes
    - 2.5 µl/min for 2 minutes
- Beads coated with anti-DIG fab fragments are sonicated prior to their introduction in the flow cell to avoid bead clumping and introduced in following steps:
    - 25 µl/min for 90 seconds

    - 5 µl/min for 7 minutes (can be adjusted depending on coverage of the FOV)
- Remaining unattached beads are flushed out of the cell.
- Attach the magnet holder with 1 cm magnets spaced 6 cm apart to the C-150.PD.
- Quality of the field can be tested by alternating the flow while stuck beads could be freed by alternating the magnet rotation.

11.3 Characterization steps and enzymatic experiment

Gain and exposure of the camera can be adjusted to change the readout performance. Gain = 0 and Exposure = 250000 (experimental frame rate of 4 Hz) or Gain = 18 and Exposure = 30000 (force calibration frame rate of 33 Hz).

First step is to check the molecules for their mobility by a flow reversal.

- Gain is set to 0 and exposure to 250000 initially.
- A set flow rate of 20 µl/min is used to check for reversals at the beginning of each experiment.
    - 20 µl/min for 10 seconds
    - 20 µl/min reverse flow for 30 seconds
    - 20 µl/min for 30 seconds

Next step is to check the coilability of the molecules in the field by coiling the molecule by 150 turns in negative and positive direction at a flow rate of 20 µl/min which corresponds to a force of around 2 pN for the flow setup described here. A differentiation between single-tethered or multiply tethered beads could also be seen during this step.

- Velocity in the PI software is set to 720 (2 rotations per second) and following macro can be used to run the coil check program. Actions are explained in brackets (not to be used while running the macro)

```
1 mov 1 -54000           (runs the tweezers clockwise for -150 turns)
1 del 75000              (time delay of 75 seconds)
1 mov 1 54000            (runs the tweezers counterclockwise for +300 turns)
1 del 150000             (time delay of 150 seconds)
```

1 mov 1 0	(runs the tweezers clockwise for -150 turns)
1 del 75000	(time delay of 75 seconds)

- Flowrate is changed to the reaction flowrate (as an example: 2.5 µl/min for gyrase reactions or 20 µl/min for replication reactions)

Recording is paused while the gain is changed to 18 and the exposure to 30000 for the third step of force determination.

- Excursions of the beads lateral to the flow are recorded for 90 seconds at higher frame rate (33 Hz) to capture the variance of the displacement and determine the force.

Gain is changed again to 0 and exposure to 250000 for rest of the experiment.

Another characterization step can be added here. For topoisomerases or topology assays in general, a coordinate transformation step can be performed where DNA is coiled at the reaction flowrate. Any topology changes could thus be transformed from the known extension changes at a particular flowrate. Once an enzymatic reaction takes place, the experiment can be concluded or other tests could be done (such as the response of gyrase to constant magnet rotation via the treadmilling assay or checking if the replisome duplicated a single parental strand into two daughter strands by running the coil-check macro again).

Additional reversal step towards the end of an experiment could also be used in different ways. One example is gyrase reaction; where gyrase compacts the strand due to (-) supercoiling. A reversal at 20 µl/min would resolve the plectonemes and extend the DNA due to local melting of the helix. Last reversals are also used to filter stuck beads which in turn are used to correct drift.

12 Appendix III: Determining pixel dimensions

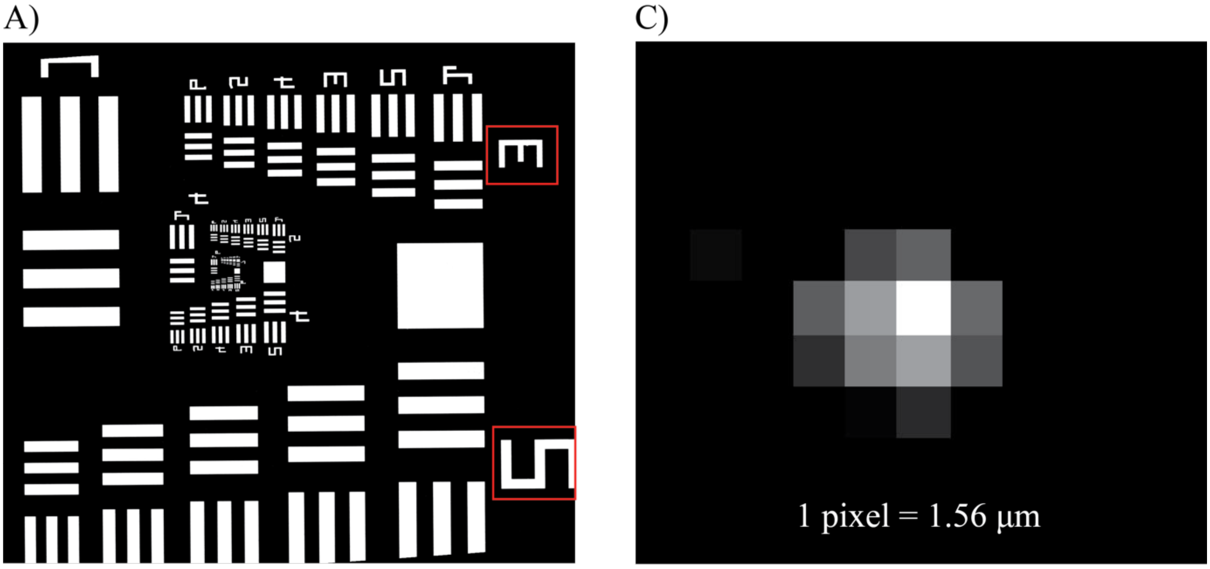

B)

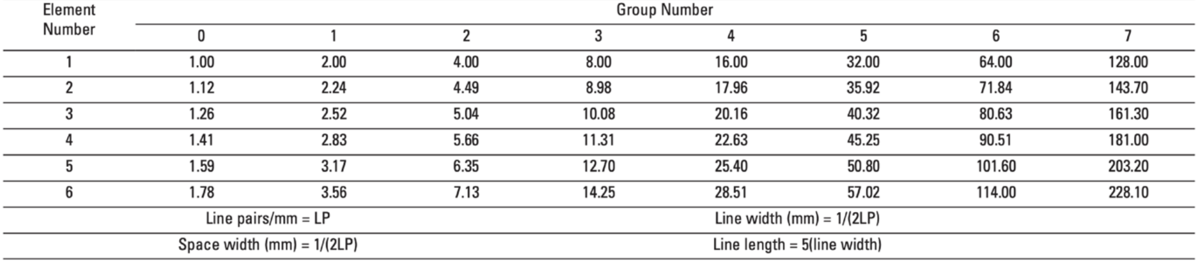

Line Pairs per millimeter

Element Number	Group Number							
	0	1	2	3	4	5	6	7
1	1.00	2.00	4.00	8.00	16.00	32.00	64.00	128.00
2	1.12	2.24	4.49	8.98	17.96	35.92	71.84	143.70
3	1.26	2.52	5.04	10.08	20.16	40.32	80.63	161.30
4	1.41	2.83	5.66	11.31	22.63	45.25	90.51	181.00
5	1.59	3.17	6.35	12.70	25.40	50.80	101.60	203.20
6	1.78	3.56	7.13	14.25	28.51	57.02	114.00	228.10

Line pairs/mm = LP
Line width (mm) = 1/(2LP)
Space width (mm) = 1/(2LP)
Line length = 5(line width)

Figure 12-1 Determining the pixel dimensions. A) A glass cover with line elements. The focus was adjusted to obtain a sharp image and group numbers 2 and 3 were analysed further using the elements numbered in table B) where the number of line pairs per millimetre are given. The image was analysed using ImageJ. C) Shown is an image of a single 2.8 µm diameter bead. Pixels with different intensities are seen here with values between 0 and 255. The software pinpoints the centre of the bead with an accuracy of ~8 nm when only considering the camera noise combined with the low magnification. A pixel corresponds to 1.56 µm which is approximately equal to the theoretical value obtained of 1.571 µm/pixel; based on the magnification combined with the pixel size.

13 Appendix IV: Flow profile in the flow cell

Relative motion of a fluid in a flow chamber can create flow pattern whose properties can be predicted using Reynolds number (R_e). It determines the relative importance of competing phenomena such as inertial or viscous forces and characterizes flow regime as either laminar or turbulent[98].

$$R_e = \frac{inertial\,forces}{viscous\,forces} = \frac{\rho v L}{\eta} \tag{13.1}$$

where ρ is the density of the fluid (kg.m^{-3}), v is the characteristic flow velocity (m.s^{-1}), L is the characteristic length (geometry of the flow system with units in m) and η is the viscosity (Pa.s). Low R_e signifies dominance of viscous forces and laminar flow profile in a chamber. Flow lane used in this study had a width of 3 mm and a height of 0.1 mm. Calculation for R_e indicate that the system remains in laminar mode and can be interpreted using Stokes' equations (see Force determination).

As the difference in the dimensions of the flow lane are considerable, the cell geometry can be approximated to have two infinite, parallel and steady-plates (parallel-plate flow chamber). If a fluid is assumed to have a constant density and viscosity and Re $\ll 1$, Navier-Stokes equation can be used to ascertain flow profile of a fluid[99].

$$\rho\left(\frac{\partial \vec{v}}{\partial t} - \vec{v}.\nabla\vec{v}\right) = -\nabla P + \eta\nabla^2\vec{v} + f \tag{13.2}$$

∇P is the pressure gradient (N.m^{-2}) and f is the external force in the system (N).

Due to unidirectionality of the flow between the parallel plates v (u,v,w), the components v- and w = 0. Additional variables such as acceleration are eliminated as the flow is steady $\left(\frac{\partial \vec{v}}{\partial t} = 0\right)$, inertial forces are negligible $(\vec{v}.\nabla\vec{v} = 0)$ and external forces are assumed to be absent $(f = 0)$. The equation is simplified further as the velocity is dependent on the flow component in the y direction and pressure in the x direction.

$$0 = -\nabla p + \eta \nabla^2 v \quad \text{or} \quad \frac{\partial P}{\partial x} = \eta \frac{\partial^2 u}{\partial y^2} \tag{13.3}$$

Assuming no slip boundaries, velocity is zero at the top- and bottom plate (u = 0 at y = ± h) and maximum at the center (y = 0). The integration of the equation using these conditions gives a parabolic profile as shown in Figure 13-1.

$$u = \frac{1}{2\eta} \frac{\partial P}{\partial x} (y^2 + h^2) \tag{13.4}$$

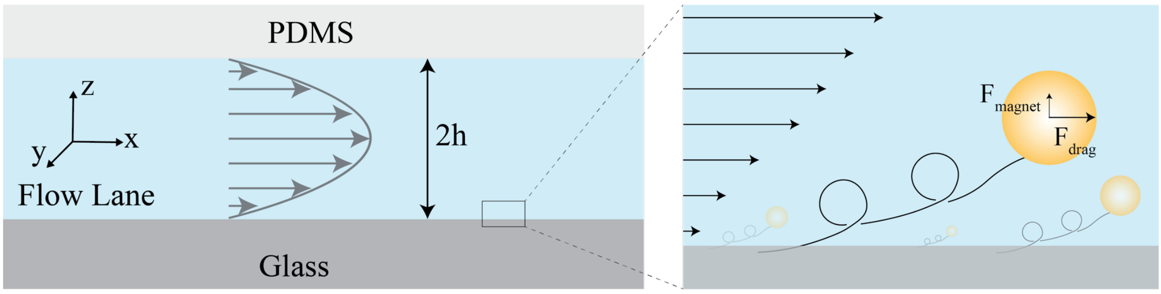

Figure 13-1 Unidirectional flow follows a parabolic velocity profile between two parallel plates of the flow cell (y = 100 µm). The flow velocity component in x direction (u) follows a parabolic path and is a function of height y. The flow u = 0 at the boundaries (y = ± h) and maximum (u = u_{max}) at the center of the flow cell (y = 0).

14 Appendix V: Supplementary movies

Following section provides description for supplementary video files.[100]

File Name: Supplementary movie 1:

Description: **Flow reversal in a typical FMT field of view**. The dimensions of the field are 5.2 mm x 3 mm where each pixel corresponds to 1.56 µm^2 after a binning of 2. The insets with yellow boundaries show 10x and 100x zoom of the vast field. The video shows a feature called flow reversal where flow is reversed at positive and negative 20 µl/min. This shows mobility of all the molecules. This field contains approximately 30,000 beads, out of which more than 16,000 beads are mobile molecules.

File Name: Supplementary Movie 2:

Description: **Representative FMT experiment imaging gyrase dynamics**. A single molecule is shown on the left together with a series of plots on the right showing flow changes, magnet rotations, and bead tracking. After the sequence of flow changes and magnet rotations described in the text and displayed in Fig 4b, gyrase is introduced into the flow cell. Positive relaxation and negative introduction are observed when gyrase engages the DNA molecule. Following these events, the magnet is continuously rotated at 480 rpm for four minutes to constantly introduce positive supercoils. These are resolved in real-time by gyrase and the tether length remains constant. Finally, magnet rotation is stopped and gyrase negatively supercoils the DNA molecule resulting in rapid compaction at the end of the video. This video is sped up and slowed down at certain points to accentuate selected features of the trace.

File Name: Supplementary Movie 3

Description: **Representative FMT experiment imaging gyrase showing a DNA break during a burst of negative supercoil introduction.**

15 Abbreviations

σ	-	Superhelical density
(-) supercoil	-	Negative supercoil
(+) supercoil	-	Positive supercoil
A	-	Adenine
AFS	-	Acoustic force spectroscopy
APTES	-	Aminopropyltriethoxysilane
ATP	-	Adenosine triphosphate
BSA	-	Bovine serum albumin
C	-	Cytosine
cccDNA	-	Covalently closed, circular DNA
CCD	-	Charged couple device
CFM	-	Centrifuge force microscope
CTD	-	Carboxy-terminal domain
DIG	-	Digoxigenin
DNA	-	Deoxyribonucleic Acid
dsDNA	-	Double-stranded DNA
DTT	-	Dithiothreitol
DUE	-	DNA unwinding element
E. coli	-	*Escherichia coli*
EDTA	-	Ethylenediaminetetraacetic acid
FJC	-	Freely-jointed chain model
FMT	-	Flow Magnetic Tweezers
FOMT	-	Freely-orbiting magnetic tweezers
FOV	-	Field of view
G	-	Guanine
hTop2α	-	Human topoisomerase IIα
hTop2β	-	Human topoisomerase IIβ
$\mathcal{L}$	-	Langevin function
Lk	-	Linking number
MT	-	Magnetic Tweezers
MTT	-	Magnetic Torque Tweezers

NA	-	Numerical Aperture
nm	-	Nanometers
OT	-	Optical Tweezers
PBS	-	Phosphate-buffered saline
PCR	-	Polymerase chain reaction
PDMS	-	Polydimethylsiloxane
PEG	-	Polyethylene glycol
pN	-	Piconewton
QPD	-	Quadrant photo diode
Re	-	Reynolds number
scTop2	-	*Saccharomyces cerevisiae* topoisomerase II
SDS	-	Sodium dodecyl sulfate
SMC	-	Structural maintenance of chromosome proteins
smFRET	-	Single-molecule Förster resonance energy transfer
ssDNA	-	Single-stranded DNA
STED	-	Stimulated emission depletion
T	-	Thymine
TEDA	-	T5 exonuclease DNA assembly
TIRF	-	Total internal reflection fluorescence
TL	-	Telecentric lens
Tw	-	Twist
UUID	-	Universally Unique ID
WLC	-	Worm-like chain model
Wr	-	Writhe

16 Acknowledgements

I cannot begin to express my thanks to Prof. Karl Duderstadt for providing me with the amazing opportunity to work on this project. The completion of my dissertation would not have been possible without his constant support (scientific and otherwise) and nurturing. He always had a positive outlook and encouraging words whenever the projects hit a roadblock. Our lengthy discussions were always very instructive for me. I would also like to thank Max Planck Society and SFB 863 for funding my position and the project.

I would like to extend my deepest appreciation to the members of my thesis advisory committee: Prof. Jan Lipfert, Prof. Ralf Jungmann and Dr. Christian Biertümpfel. As an expert on everything magnetic tweezers, Jan was a catalyst for so many ideas during my project and pointed me in the right direction during the TAC and the SFB meetings. Throughout my time at MPIB, Ralf was a mentor and made me a better scientist through his advice and our discussions. Christian's feedback on the experimental design and replication assays was really valuable.

I am grateful to all the members of the Duderstadt lab for creating such an enjoyable work environment, helping out with the innumerable biochemical assays and giving constructive feedback during our lab meetings. Many thanks to our lab manager Dr. Lional Rajappa for teaching me the basics of making DNA substrates and purifying proteins. Thomas Retzer and Dr. Anita Minnen for their ideas and feedback during the bacterial subgroup meetings. Matthias, Barbara and Nadia were cool lab mates and always fun to be around. I would also like mention the support of our neighbors, the Pfander lab. As one of the first persons to join the Duderstadt lab, the Pfander lab members: Boris, Julia, Kalle, Leo, Lorenzo, Martina and Susi were always really supportive and welcoming. Especially Lorenzo, who was my lab neighbor by default for most weekends and late evening experiments.

I would like to thank our collaborators and labs of Prof. James Berger and Prof. Nick Dixon for the gifts of topoisomerases and *E. coli* replication proteins respectively. Thanks also to the IMPRS-LS graduate school and SFB 863 for providing their support, organizing retreats and scientific training over the years.

Finally, I want to express my gratitude to my family for their unwavering support throughout my stay here in Germany. I am deeply grateful to my father for trusting me with my education and my mother for taking care of our whole family. My brother provided me with encouragement in times of much needed guidance and always made me laugh. I was lucky enough to have family here in Munich. A very special thanks to my sister-in-law for being a good friend. Lastly, I would thank my nephew Niklas for making the concluding months of my doctoral research infinitely better.

17 References

1. Watson, J.D. et al. Molecular Biology of the Gene. Pearson. (2014).
2. Watson, J.D. & Crick, F.H.C. Genetical Implications of the Structure of Deoxyribonucleic Acid. *Nature* **171**, 964-967 (1953).
3. Koster, D.A., Crut, A., Shuman, S., Bjornsti, M.-A. & Dekker, N.H. Cellular Strategies for Regulating DNA Supercoiling: A Single-Molecule Perspective. *Cell* **142**, 519-530 (2010).
4. Kuhn, W. Über die Gestalt fadenförmiger Moleküle in Lösungen. *Kolloid-Zeitschrift* **68**, 2-15 (1934).
5. Sarkar, R. & Rybenkov, V.V. A Guide to Magnetic Tweezers and Their Applications. *Frontiers in Physics* **4**(2016).
6. Smith, S., Finzi, L. & Bustamante, C. Direct mechanical measurements of the elasticity of single DNA molecules by using magnetic beads. *Science* **258**, 1122-1126 (1992).
7. Bustamante, C., Marko, J.F., Siggia, E.D. & Smith, S. Entropic elasticity of lambda-phage DNA. *Science* **265**, 1599 (1994).
8. Lipfert, J. et al. Double-stranded RNA under force and torque: Similarities to and striking differences from double-stranded DNA. *Proceedings of the National Academy of Sciences* **111**, 15408-15413 (2014).
9. Wang, X., Montero Llopis, P. & Rudner, D.Z. Organization and segregation of bacterial chromosomes. *Nature reviews. Genetics* **14**, 191-203 (2013).
10. Stracy, M. et al. Single-molecule imaging of DNA gyrase activity in living Escherichia coli. *Nucleic acids research* **47**, 210-220 (2019).
11. Postow, L., Crisona, N.J., Peter, B.J., Hardy, C.D. & Cozzarelli, N.R. Topological challenges to DNA replication: Conformations at the fork. *Proceedings of the National Academy of Sciences* **98**, 8219-8226 (2001).

12. Breier, A.M., Weier, H.-U.G. & Cozzarelli, N.R. Independence of replisomes in Escherichia coli chromosomal replication. *Proceedings of the National Academy of Sciences of the United States of America* **102**, 3942-3947 (2005).

13. Kurth, I., Georgescu, R.E. & O'Donnell, M.E. A solution to release twisted DNA during chromosome replication by coupled DNA polymerases. *Nature* **496**, 119-122 (2013).

14. Xu, Z.-Q. & Dixon, N.E. Bacterial replisomes. *Current Opinion in Structural Biology* **53**, 159-168 (2018).

15. Chen, S.H., Chan, N.-L. & Hsieh, T.-s. New Mechanistic and Functional Insights into DNA Topoisomerases. *Annual Review of Biochemistry* **82**, 139-170 (2013).

16. Vos, S.M., Tretter, E.M., Schmidt, B.H. & Berger, J.M. All tangled up: how cells direct, manage and exploit topoisomerase function. *Nature Reviews Molecular Cell Biology* **12**, 827-841 (2011).

17. Soczek, K.M., Grant, T., Rosenthal, P.B. & Mondragón, A. CryoEM structures of open dimers of gyrase A in complex with DNA illuminate mechanism of strand passage. *eLife* **7**, e41215 (2018).

18. Hooper, D.C. & Jacoby, G.A. Topoisomerase Inhibitors: Fluoroquinolone Mechanisms of Action and Resistance. *Cold Spring Harbor Perspectives in Medicine* **6**(2016).

19. Frank, J. et al. A model of protein synthesis based on cryo-electron microscopy of the E. coli ribosome. *Nature* **376**, 441-444 (1995).

20. Vitali Tugarinov, Hwang, P.M. & Kay, L.E. Nuclear Magnetic Resonance Spectroscopy of High-Molecular-Weight Proteins. *Annual Review of Biochemistry* **73**, 107-146 (2004).

21. Kendrew, J.C. et al. A Three-Dimensional Model of the Myoglobin Molecule Obtained by X-Ray Analysis. *Nature* **181**, 662-666 (1958).

22. Ashkin, A. Acceleration and Trapping of Particles by Radiation Pressure. *Physical Review Letters* **24**, 156-159 (1970).

23. Ashkin, A., Dziedzic, J.M., Bjorkholm, J.E. & Chu, S. Observation of a single-beam gradient force optical trap for dielectric particles. *Optics Letters* **11**, 288-290 (1986).

24. Neuman, K.C. & Nagy, A. Single-molecule force spectroscopy: optical tweezers, magnetic tweezers and atomic force microscopy. *Nature Methods* **5**, 491-505 (2008).

25. Miller, H., Zhou, Z., Shepherd, J., Wollman, A.J.M. & Leake, M.C. Single-molecule techniques in biophysics: a review of the progress in methods and applications. *Reports on Progress in Physics* **81**, 024601 (2017).

26. Vale, R.D., Reese, T.S. & Sheetz, M.P. Identification of a novel force-generating protein, kinesin, involved in microtubule-based motility. *Cell* **42**, 39-50 (1985).

27. Block, S.M., Goldstein, L.S.B. & Schnapp, B.J. Bead movement by single kinesin molecules studied with optical tweezers. *Nature* **348**, 348-352 (1990).

28. Svoboda, K., Schmidt, C.F., Schnapp, B.J. & Block, S.M. Direct observation of kinesin stepping by optical trapping interferometry. *Nature* **365**, 721-727 (1993).

29. Brower-Toland, B.D. et al. Mechanical disruption of individual nucleosomes reveals a reversible multistage release of DNA. *Proceedings of the National Academy of Sciences* **99**, 1960-1965 (2002).

30. Abbondanzieri, E.A., Greenleaf, W.J., Shaevitz, J.W., Landick, R. & Block, S.M. Direct observation of base-pair stepping by RNA polymerase. *Nature* **438**, 460-465 (2005).

31. Berg-Sørensen, K. & Flyvbjerg, H. Power spectrum analysis for optical tweezers. *Review of Scientific Instruments* **75**, 594-612 (2004).

32. La Porta, A. & Wang, M.D. Optical Torque Wrench: Angular Trapping, Rotation, and Torque Detection of Quartz Microparticles. *Physical Review Letters* **92**, 190801 (2004).

33. Friese, M.E.J., Nieminen, T.A., Heckenberg, N.R. & Rubinsztein-Dunlop, H. Optical alignment and spinning of laser-trapped microscopic particles. *Nature* **394**, 348-350 (1998).

34. Strick, T.R., Allemand, J.-F., Bensimon, D., Bensimon, A. & Croquette, V. The Elasticity of a Single Supercoiled DNA Molecule. *Science* **271**, 1835-1837 (1996).

35. Lipfert, J., Wiggin, M., Kerssemakers, J.W.J., Pedaci, F. & Dekker, N.H. Freely orbiting magnetic tweezers to directly monitor changes in the twist of nucleic acids. *Nature Communications* **2**, 439 (2011).

36. Lipfert, J., Kerssemakers, J.W.J., Jager, T. & Dekker, N.H. Magnetic torque tweezers: measuring torsional stiffness in DNA and RecA-DNA filaments. *Nature Methods* **7**, 977-980 (2010).

37. Kriegel, F., Ermann, N. & Lipfert, J. Probing the mechanical properties, conformational changes, and interactions of nucleic acids with magnetic tweezers. *Journal of Structural Biology* **197**, 26-36 (2017).

38. te Velthuis, A.J.W., Kerssemakers, J.W.J., Lipfert, J. & Dekker, N.H. Quantitative Guidelines for Force Calibration through Spectral Analysis of Magnetic Tweezers Data. *Biophysical Journal* **99**, 1292-1302 (2010).

39. Vilfan, I.D., Lipfert, J., Koster, D.A., Lemay, S.G. & Dekker, N.H. Magnetic Tweezers for Single-Molecule Experiments. in *Handbook of Single-Molecule Biophysics* (eds. Hinterdorfer, P. & Oijen, A.) 371-395 (Springer US, New York, NY, 2009).

40. van Oijen, A.M. et al. Single-Molecule Kinetics of λ Exonuclease Reveal Base Dependence and Dynamic Disorder. *Science* **301**, 1235 (2003).

41. Dessinges, M.N. et al. Stretching Single Stranded DNA, a Model Polyelectrolyte. *Physical Review Letters* **89**, 248102 (2002).

42. van Oijen, A.M. Honey, I shrunk the DNA: DNA length as a probe for nucleic-acid enzyme activity. *Biopolymers* **85**, 144-153 (2007).

43. Wuite, G.J.L., Smith, S.B., Young, M., Keller, D. & Bustamante, C. Single-molecule studies of the effect of template tension on T7 DNA polymerase activity. *Nature* **404**, 103-106 (2000).

44. Lee, J.B. et al. DNA primase acts as a molecular brake in DNA replication. *Nature* **439**, 621-4 (2006).

45. Hamdan, S.M., Loparo, J.J., Takahashi, M., Richardson, C.C. & van Oijen, A.M. Dynamics of DNA replication loops reveal temporal control of lagging-strand synthesis. *Nature* **457**, 336-339 (2009).

46. Tanner, N.A. et al. Single-molecule studies of fork dynamics in Escherichia coli DNA replication. *Nature Structural & Molecular Biology* **15**, 170-176 (2008).

47. Duderstadt, K.E. et al. Simultaneous Real-Time Imaging of Leading and Lagging Strand Synthesis Reveals the Coordination Dynamics of Single Replisomes. *Molecular Cell* **64**, 1035-1047 (2016).

48. Crut, A., Koster, D.A., Seidel, R., Wiggins, C.H. & Dekker, N.H. Fast dynamics of supercoiled DNA revealed by single-molecule experiments. *Proceedings of the National Academy of Sciences* **104**, 11957-11962 (2007).

49. Lang, M.J., Fordyce, P.M., Engh, A.M., Neuman, K.C. & Block, S.M. Simultaneous, coincident optical trapping and single-molecule fluorescence. *Nature Methods* **1**, 133-139 (2004).

50. Heller, I. et al. STED nanoscopy combined with optical tweezers reveals protein dynamics on densely covered DNA. *Nature Methods* **10**, 910-916 (2013).

51. Lee, M., Kim, S.H. & Hong, S.-C. Minute negative superhelicity is sufficient to induce the B-Z transition in the presence of low tension. *Proceedings of the National Academy of Sciences* **107**, 4985-4990 (2010).

52. De Vlaminck, I. et al. Highly Parallel Magnetic Tweezers by Targeted DNA Tethering. *Nano Letters* **11**, 5489-5493 (2011).

53. Yang, D., Ward, A., Halvorsen, K. & Wong, W.P. Multiplexed single-molecule force spectroscopy using a centrifuge. *Nature Communications* **7**, 11026 (2016).

54. Sitters, G. et al. Acoustic force spectroscopy. *Nature Methods* **12**, 47-50 (2015).

55. Stigler, J., Ziegler, F., Gieseke, A., Gebhardt, J.C. & Rief, M. The complex folding network of single calmodulin molecules. *Science* **334**, 512-6 (2011).

56. Neuman, K.C., Abbondanzieri, E.A., Landick, R., Gelles, J. & Block, S.M. Ubiquitous transcriptional pausing is independent of RNA polymerase backtracking. *Cell* **115**, 437-47 (2003).

57. Moffitt, J.R. et al. Intersubunit coordination in a homomeric ring ATPase. *Nature* **457**, 446-50 (2009).

58. Nöllmann, M. et al. Multiple modes of Escherichia coli DNA gyrase activity revealed by force and torque. *Nature Structural & Molecular Biology* **14**, 264-271 (2007).

59. Basu, A., Schoeffler, A.J., Berger, J.M. & Bryant, Z. ATP binding controls distinct structural transitions of Escherichia coli DNA gyrase in complex with DNA. *Nat Struct Mol Biol* **19**, 538-46, S1 (2012).

60. Berghuis, B.A., Köber, M., van Laar, T. & Dekker, N.H. High-throughput, high-force probing of DNA-protein interactions with magnetic tweezers. *Methods* **105**, 90-98 (2016).

61. Otten, M. et al. From Genes to Protein Mechanics on a Chip. *Nature methods* **11**, 1127-1130 (2014).

62. Seol, Y. & Neuman, K.C. Magnetic tweezers for single-molecule manipulation. *Methods Mol Biol* **783**, 265-93 (2011).

63. Lipfert, J., Hao, X. & Dekker, N.H. Quantitative modeling and optimization of magnetic tweezers. *Biophysical journal* **96**, 5040-5049 (2009).

64. Strick, T.R., Allemand, J.F., Bensimon, D. & Croquette, V. Behavior of supercoiled DNA. *Biophysical journal* **74**, 2016-2028 (1998).

65. Kriegel, F. et al. Probing the salt dependence of the torsional stiffness of DNA by multiplexed magnetic torque tweezers. *Nucleic Acids Research* **45**, 5920-5929 (2017).

66. Hill, F.R., van Oijen, A.M. & Duderstadt, K.E. Detection of kinetic change points in piece-wise linear single molecule motion. *J Chem Phys* **148**, 123317 (2018).

67. Wong, W.P. & Halvorsen, K. The effect of integration time on fluctuation measurements: calibrating an optical trap in the presence of motion blur. *Opt Express* **14**, 12517-31 (2006).

68. Pietzsch, T., Preibisch, S., Tomancak, P. & Saalfeld, S. ImgLib2--generic image processing in Java. *Bioinformatics* **28**, 3009-11 (2012).

69. Thompson, R.E., Larson, D.R. & Webb, W.W. Precise nanometer localization analysis for individual fluorescent probes. *Biophys J* **82**, 2775-83 (2002).

70. Urbanska, M. et al. (2020).

71. Bouchiat, C. et al. Estimating the persistence length of a worm-like chain molecule from force-extension measurements. *Biophys J* **76**, 409-13 (1999).

72. Bush, N.G., Evans-Roberts, K. & Maxwell, A. DNA Topoisomerases. *EcoSal Plus* **6**(2015).

73. Drlica, K., Malik, M., Kerns, R.J. & Zhao, X. Quinolone-mediated bacterial death. *Antimicrob Agents Chemother* **52**, 385-92 (2008).

74. Bax, B.D. et al. Type IIA topoisomerase inhibition by a new class of antibacterial agents. *Nature* **466**, 935-40 (2010).

75. Schindelin, J. et al. Fiji: an open-source platform for biological-image analysis. *Nat Methods* **9**, 676-82 (2012).

76. Rueden, C.T. et al. ImageJ2: ImageJ for the next generation of scientific image data. *BMC Bioinformatics* **18**, 529 (2017).

77. Wang, J.C. Cellular roles of DNA topoisomerases: a molecular perspective. *Nature Reviews Molecular Cell Biology* **3**, 430 (2002).

78. Schoeffler, A.J. & Berger, J.M. DNA topoisomerases: harnessing and constraining energy to govern chromosome topology. *Q Rev Biophys* **41**, 41-101 (2008).

79. Levine, C., Hiasa, H. & Marians, K.J. DNA gyrase and topoisomerase IV: biochemical activities, physiological roles during chromosome replication, and drug sensitivities. *Biochim Biophys Acta* **1400**, 29-43 (1998).

80. Mustaev, A. et al. Fluoroquinolone-gyrase-DNA complexes: two modes of drug binding. *J Biol Chem* **289**, 12300-12 (2014).

81. Forterre, P., Gribaldo, S., Gadelle, D. & Serre, M.-C. Origin and evolution of DNA topoisomerases. *Biochimie* **89**, 427-446 (2007).

82. Schoeffler, A.J. & Berger, J.M. DNA topoisomerases: harnessing and constraining energy to govern chromosome topology. *Quarterly Reviews of Biophysics* **41**, 41-101 (2008).

83. Roca, J. & Wang, J.C. DNA transport by a type II DNA topoisomerase: Evidence in favor of a two-gate mechanism. *Cell* **77**, 609-616 (1994).

84. Valdés, A., Segura, J., Dyson, S., Martínez-García, B. & Roca, J. DNA knots occur in intracellular chromatin. *Nucleic Acids Research* **46**, 650-660 (2017).

85. Schmidt, B.H., Osheroff, N. & Berger, J.M. Structure of a topoisomerase II–DNA–nucleotide complex reveals a new control mechanism for ATPase activity. *Nature Structural & Molecular Biology* **19**, 1147-1154 (2012).

86. Vanden Broeck, A., Lotz, C., Ortiz, J. & Lamour, V. Cryo-EM structure of the complete E. coli DNA gyrase nucleoprotein complex. *Nature Communications* **10**, 4935 (2019).

87. Riccio, A.A., Schellenberg, M.J. & Williams, R.S. Molecular mechanisms of topoisomerase 2 DNA–protein crosslink resolution. *Cellular and Molecular Life Sciences* **77**, 81-91 (2020).

88. Seol, Y., Gentry, A.C., Osheroff, N. & Neuman, K.C. Chiral Discrimination and Writhe-dependent Relaxation Mechanism of Human Topoisomerase IIα. *Journal of Biological Chemistry* **288**, 13695-13703 (2013).

89. Le, T.T. et al. Synergistic Coordination of Chromatin Torsional Mechanics and Topoisomerase Activity. *Cell* **179**, 619-631.e15 (2019).

90. Strick, T.R., Croquette, V. & Bensimon, D. Single-molecule analysis of DNA uncoiling by a type II topoisomerase. *Nature* **404**, 901-904 (2000).

91. Elshenawy, M.M. et al. Replisome speed determines the efficiency of the Tus−Ter replication termination barrier. *Nature* **525**, 394-398 (2015).

92. Howard, M.T., Neece, S.H., Matson, S.W. & Kreuzer, K.N. Disruption of a topoisomerase-DNA cleavage complex by a DNA helicase. *Proc Natl Acad Sci U S A* **91**, 12031-5 (1994).

93. Hiasa, H., Yousef, D.O. & Marians, K.J. DNA strand cleavage is required for replication fork arrest by a frozen topoisomerase-quinolone-DNA ternary complex. *J Biol Chem* **271**, 26424-9 (1996).

94. Scherr, M.J., Safaric, B. & Duderstadt, K.E. Noise in the Machine: Alternative Pathway Sampling is the Rule During DNA Replication. *Bioessays* **40**(2018).

95. van Loenhout, M.T.J., de Grunt, M.V. & Dekker, C. Dynamics of DNA Supercoils. *Science* **338**, 94-97 (2012).

96. Bryant, Z. et al. Structural transitions and elasticity from torque measurements on DNA. *Nature* **424**, 338-341 (2003).

97. Xia, Y. et al. T5 exonuclease-dependent assembly offers a low-cost method for efficient cloning and site-directed mutagenesis. *Nucleic Acids Research* **47**, e15-e15 (2018).

98. Acheson, D.J. Elementary fluid dynamics. (Acoustical Society of America, 1991).

99. W Fox, R. & T Mcdonald, A. Introduction to Fluid Mechanics. (John Wiley & Sons, Inc., 2004).

100. Agarwal, R. & Duderstadt, K.E. Multiplex flow magnetic tweezers reveal rare enzymatic events with single molecule precision. *Nature Communications* **11**, 4714 (2020).